UNIVERSITÉ DU QUÉBEC À MONTRÉAL

MODELLING OF THERMAL CONVECTION IN THE EARTH'S MANTLE

THESIS SUBMITTED AS PARTIAL REQUIREMENT FOR

THE DEGREE OF DOCTOR OF PHILOSOPHY

IN EARTH AND ATMOSPHERIC SCIENCES

BY

PETAR GLIŠOVIĆ

OCTOBER 2012

UNIVERSITÉ DU QUÉBEC À MONTRÉAL

MODÉLISATION DE LA CONVECTION THERMIQUE DANS LE MANTEAU TERRESTRE

THÈSE PRÉSENTÉE

COMME EXIGENCE PARTIELLE DU

DOCTORAT EN SCIENCES DE LA TERRE ET DE L'ATMOSPHÈRE

PAR

PETAR GLIŠOVIĆ

OCTOBRE 2012

ACKNOWLEDGEMENTS

This thesis would not have been possible without the guidance, encouragement and generous financial support of my mentor, Professor Alessandro Forte. His fatherly advice and friendship has been invaluable on both an academic and a personal level, for which I am extremely grateful.

I would like to thank Professors Jean-Claude Mareschal and Fiona Darbyshire for their help, and kindness, teaching me important lessons on both geophysics and humanity over the past four years. Also, I would like to thank Professor Jerry X. Mitrovica for valuable suggestions and comments that improve the final version of thesis.

I enjoyed many inspirational discussions with Professor Robert Moucha, and Xavier Robert. To Professor Moucha, I owe special thanks for his great patience, and for his kindly guidance that have lead me through this exciting and difficult journey. Also, I am very grateful to my dear friend Paul Auerbach for promoting a stimulating and welcoming social environment to me and my family.

The simulations used in this study are computed on the supercomputing facilities of the SciNet consortium at the University of Toronto. I thank the stuff of the SciNet for their support.

My special thanks to my parents, sister, and brother for their selfless love, and unconditional support.

Finally, I owe my deepest gratitude to my wife Sanja and my son Andrej for their understating, and whose unlimited love has been my deep well of strength during all these years.

TABLE OF CONTENTS

LIST OF FIGURES

FIGURE Page

LIST OF TABLES

RÉSUMÉ

Nous construisons un modèle dépendant du temps, en géométrie tridimensionnelle sphérique, de la convection dans un manteau compressible et dissipatif qui est compatible avec la dynamique de l'écoulement mantellique instantané basé sur la tomographie sismique. Nous réalisons cet objectif à l'aide d'une méthode numérique pseudo-spectrale actualisée et révisée. En résolvant le problème direct de la convection thermique dans le manteau, nous obtenons une gamme réaliste de flux de chaleur à la surface de la Terre, variant de 37 TW pour une surface rigide à 44 TW pour une surface avec plaques tectoniques couplés à l'écoulement mantellique. De plus, nos modèles de convection prédisent des flux de chaleur à la frontière noyau-manteau (CMB) qui se trouvent à la limite supérieure des valeurs estimées précédemment, à savoir 13 TW et 20 TW, pour la surface rigide et la surface avec plaques, respectivement. Les deux conditions aux limites de surface, ainsi que les profils radiaux de viscosité inférés de la géodynamique, donnent des flux convectifs en état d'équilibre qui sont dominés par de longues longueurs d'onde tout à travers la partie inférieure du manteau. À savoir la condition de surface rigide donne un spectre d'hétérogénéité mantellique dominé par le degré 4 à l intérieur des couches limites thermiques (TBL), et la condition de surface avec plaques donne comme résultat un spectre dominé par le degré 1. Nous démontrons que la structure initiale thermique est fortement imprimée sur l'évolution future du manteau, et aussi que la mesure dans laquelle l'hétérogénéité initiale du manteau détermine la distribution de la température finale dépend de la condition à la limite de la surface. Notre exploration de la dépendance temporelle de l'hétérogénéité spatiale indique que, pour ces deux types de condition aux limites à la surface, les remontées de matière chaude provenant du manteau profond qui sont résolues dans le modèle tomographique sont des caractéristiques durables et stables de la convection dans le manteau terrestre. Ces panaches chauds profondément enracinées dans le manteau profond démontrent une longévité remarquable au cours de très longues des intervalles de temps géologiques. Cette stabilité des panaches profonds est principalement due à la forte viscosité dans le manteau inférieur inférée avec les données géodynamiques. Nous proposons également que les panaches mantelliques profondes sous les points chauds («hotspots») suivants : Pitcairn, Pâques, Galápagos, Crozet, Kerguelen, Caroline, et le Cap-Vert, sont les mieux résolus par l'imagerie tomographique du manteau à grand échelle. Afin de résoudre et évaluer la robustesse du problème inverse de la convection mantellique, nous considérons et comparons deux différentes techniques numériques actuellement utilisées dans la modélisation de la convection vers le passé: les méthodes d la quasi-réversibilité (QRV) et de l'advection vers l'arrière (BAD), sur un intervalle de temps de plus de 65 millions d'années. Nous définissons une nouvelle formulation du paramètre de régularisation pour la méthode QRV en terme d'une fonction dépendant du temps et nous quantifions la gamme des

incertitudes suivantes, [7 à 29]% [11 à 37]% [8 à 33]%, et [6 à 9]% pour les champs de la divergence des plaques, les anomalies de gravité à l'air libre, la topographie dynamique de la surface, et la topographie de la CMB, respectivement. Les implications dominantes pour le problème inverse de la convection mantellique sont à la fois le choix d'un géotherme et le type de condition limite à la surface. Toutefois, l'impact critique sur la reconstruction de l'évolution thermique du manteau provient de l'intégration entre les hétérogénéités du manteau (structures décrites par degrés harmoniques $\ell \geq 1$) et un géotherme «réaliste» (structure décrite par le degré harmonique $\ell = 0$), à l'intérieur des couches limites thermiques.

Mots clés: Flux de chaleur, tomographie sismique, tectonique planétaire, courants de convection, panaches mantelliques, points chauds, rhéologie du manteau, méthodes d'inversion, Cénozoïque.

ABSTRACT

We construct a time-dependent, compressible, and dissipative convection model in three-dimensional spherical geometry that is consistent with tomography-based instantaneous flow dynamics, using an updated and revised pseudo-spectral numerical method. Solving the direct problem of thermal convection in the mantle we obtain surface heat flux in the range of Earth-like values: 37 TW for a rigid surface and 44 TW for a surface with tectonic plates coupled to the mantle flow. Also, our convection models deliver core-mantle boundary (CMB) heat flux that is on the high end of previously estimated values, namely 13 TW and 20 TW, for the rigid and plate-like surface boundary conditions, respectively. The two surface boundary conditions, along with the geodynamically inferred radial viscosity profiles, yield steady-state convective flows that are dominated by long wavelengths throughout the lower mantle. Namely, the rigid-surface condition yields a spectrum of mantle heterogeneity dominated by degree 4 inside the thermal boundary layers (TBLs), and the plate-like surface condition yields a pattern dominated by degree 1. We demonstrate that an initial thermal structure is strongly imprinted on the future mantle evolution, and also that the extent to which a starting mantle heterogeneity determines the final temperature distribution depends on the surface boundary conditions. Our exploration of the time-dependence of the spatial heterogeneity shows that, for both types of surface boundary condition, deep-mantle hot upwellings resolved in the present-day tomography model are durable and stable features. These deeply-rooted mantle plumes show remarkable longevity over very long geological time spans, mainly owing to the geodynamically-inferred high viscosity in the lower mantle. We also suggest that the deep-mantle plumes beneath the following hotspots: Pitcairn, Easter, Galapagos, Crozet, Kerguelen, Caroline, and Cape Verde are most-likely resolved by the present-day tomographic image. To solve and estimate robustness of the inverse problem of mantle convection we consider and compare two different numerical techniques currently used in backward convection modelling: the quasi-reversibility (QRV) and the backward advection (BAD) methods over a 65 Myr interval. We define a new formulation of regularization parameter for the QRV method as a time-dependent function quantifying the range of uncertainties [7,29]%, [11,37]%, [8,33]%, and [6,9]% for the surface divergence, the free-air gravity anomalies, the dynamic surface topography and CMB topography, respectively. The dominant implications for the inverse problem of mantle flow are both a choice of a geotherm and a type of surface boundary condition. However, the critical impact on the reconstruction of mantle evolution has a degree of integration between the mantle heterogeneity ($\ell \geq 1$ structure) and the 'Earth-like' geotherm ($\ell = 0$ structure) inside thermal boundary layers.

Keywords: Heat flow, seismic tomography, planetary tectonics, convection currents, mantle plumes, hotspots, mantle rheology, inverse methods, Cenozoic.

INTRODUCTION

Our research is focused on the numerical modelling of both the direct (forward-in-time) and inverse (backward-in-time) problems of thermal convection in the Earth's mantle. Thermal convection describes how mass and heat is transferred across vast distances inside the rocky mantle of the Earth (a region extending from below the crust of our planet to the liquid core, a distance of almost 3000 km). This phenomenon controls the evolution of our entire planet and affects a wide suite of processes that occur at the surface of the Earth including: continental drift, earthquakes, heat flow, mountain building, changes in sea level, and more. Therefore, one of the outstanding problems in modern geodynamics is the development of a thermal convection model that has optimal consistency with a wide suite of seismic, geodynamic, and mineral physical constraints on mantle structure and thermodynamic properties.

Time-dependent models of mantle flow are most often initialized by a theoretically perturbed mantle heterogeneity (e.g., Davies & Davies (2009)), that may, in some cases, also include surface geological constraints such as tectonic plate velocity histories (e.g., Schuberth et al. (2009b)). A more realistic internal loading state of the Earth's mantle can be provided by seismic tomography (e.g., Simmons et al. (2009)). However, seismic-tomography images of present-day mantle heterogeneity have generally been used for models of the instantaneous flow, fitting convection-related surface geodynamic data (e.g., Forte (2007)). The importance of the initial buoyancy field on the evolution of Earth's internal structure is still undetermined.

Additional complexity in determining the extent to which the 'final' (i.e. steady-state) temperature distribution depends on the initial mantle heterogeneity is introduced by surface boundary conditions. Namely, the dynamic impact of plates plays a crucial role in organizing and modulating cold downwellings and hot upwellings (e.g., Quéré & Forte (2006)). This impact is

highly constrained by: (1) constantly evolving plate geometries over the past 200 million years (e.g., Müller et al. (2008)); (2) the inability to reconstruct mantle heterogeneity before 100 Myr (Bunge et al. (2002)); (3) no currently accepted theory for accurately predicting the future evolution of plate geometries over very long geological time spans, in a manner that is dynamically self-consistent with the underlying mantle flow. In modern geodynamic modelling, the surface boundary condition is most often treated either by: (1) a free-slip surface coupled with the high-viscosity lithospheric lid and a weaker interior, either depth- or temperature-dependent, and often refereed to 'stagnant-lid' (e.g., Roberts & Zhong (2006)), or 'sluggish-lid' convection (e.g., Yoshida (2008)), therefore, no plate geometry is considered, or (2) the prescribed tectonic plate velocity histories (e.g., McNamara & Zhong (2005)) that require an external driver of energy source that can compromise the energy balance of the mantle. Therefore, it is crucial to examine another two surface boundary conditions: (1) a no-slip (i.e. rigid surface) that would be applicable in the event that all tectonic plates simultaneously resist the underlying mantle flow, or for the planets without tectonics (e.g., Schubert et al. (1990)), and (2) rigid plates where the plate velocities are predicted at each instant in time, on the basis of the evolving distribution of buoyancy forces. The rigid plates boundary condition allows a present-day subduction zone to evolve into a future spreading centre, and vice versa, in response to the evolving heterogeneity in the mantle. Also, the coupled tectonic plates involves the generation of toroidal flow via surface-plate rotations and this is not the case of the two other boundary conditions (no-slip and free-slip). The toroidal flow is expected to be the result of significant lateral heterogeneities of viscosity (e.g., Forte & Mitrovica (1997)).

The most important difficulty in the understanding of the dynamics of mantle convection is due to the complexity of the rheology. The assumed depth-dependent rheology structure of the mantle has a critical impact on the spatial (and temporal) evolution of mantle temperature variations (e.g., Solheim & Peltier (1990); Yoshida & Kageyama (2006)), especially since each viscosity profile is characterised by local, depth-dependent internal-heating Rayleigh number, Ra_H, that varies over several orders of magnitude as a results of its strong dependence on temperature and pressure (e.g., Ammann et al. (2010)). Some previous mantle convection studies in spherical geometry (e.g., Schuberth et al. (2009b)) have used simplified (2- or 3-layer) radial vis-

cosity structures, not directly derived from geodynamic constraints, resulting in a wide range of heat-flux predictions. Therefore, we have opted to work with depth-dependent viscosity profiles that have been directly verified against a wide suite of geodynamic surface observables (Mitrovica & Forte (2004); Forte (2007)) and independent mineral-physical modelling (Ammann et al. (2010)).

The central guiding principle we adopt in this thesis is a derivation of mantle convection models that incorporate a sufficient number of essential ingredients (e.g., finite compressibility, gravitational consistency, complex radial rheology variations, coupling to rigid surface plates, depth-dependent thermal conductivity, thermal expansion coefficient, and internal heating). In Chapter I, we initially focus on the theory and numerical methods employed to solve the equation of thermal energy conservation using the Green's function solutions for the equation of motion, with special attention placed on the numerical accuracy and stability of the convection solutions. The use of geodynamically-constrained spectral Green's functions facilitates the modelling of the dynamical impact on the mantle evolution of: (1) depth-dependent thermal conductivity profiles, (2) extreme variations of rheology over depth and (3) different surface boundary conditions, in this case mobile surface plates and a rigid surface. The thermal interpretation of seismic tomography models does not provide a radial profile of the horizontally-averaged temperature (i.e. the geotherm) in the mantle. One important goal of this chapter is to obtain a steady-state geotherm with boundary layers that satisfy energy considerations and provide the starting point for more realistic numerical simulations of the Earth's evolution. We furthermore employ the rigid and plate-like surface boundary conditions to explore very-long time-scale evolution of convection over billion-year time windows.

Despite the recent progress in seismic modelling of mantle heterogeneity, a question regarding the importance of the initial buoyancy field constrained by tomography on the evolution of mantle thermal structure still exists. In order to address this outstanding question, in Chapter II, we present convection models initialized by different lateral temperature variations that are compared with the results obtained by models constructed in the Chapter I.

In addition to the central focus on forward convection modelling, we have invested considerable effort in implementing advanced techniques of numerical mathematics for time-reversed

convection models (Lattes & Lions (1969), Ismail-Zadeh et al. (2007)). The importance of this inverse convection modelling steams from ability of these models to explain changes in the surface geological evolution of the planet in terms of the dynamic forces originating in the convecting mantle (e.g., Moucha et al. (2008), Forte et al. (2009), Moucha & Forte (2011)). Our goal is to obtain a numerically accurate and geologically realistic description of the evolution of the mantle's 3-D thermal structure over the entire Cenozoic era (i.e. the past 65 million years), a period characterized by major changes in the configuration and motion of Earth's surface tectonic plates. To solve the inverse problem of mantle convection, and estimate the robustness of time-reversed models, in Chapter III, we consider and compare two different numerical techniques used in backward convection modelling: the quasi-reversibility (QRV), and the backward advection (BAD) over the Cenozoic era.

Finally, we briefly summarize our main conclusions and also point out what further work needs to be done to resolve outstanding problems concerning the dynamics of mantle flow.

CHAPTER I

TIME-DEPENDENT CONVECTION MODELS OF MANTLE THERMAL STRUCTURE CONSTRAINED BY SEISMIC TOMOGRAPHY AND GEODYNAMICS: IMPLICATIONS FOR MANTLE PLUME DYNAMICS AND CMB HEAT FLUX

Published in *Geophysical Journal International* (2012), vol. 190, pages 785-815,
doi: 10.1111/j.1365-246X.2012.05549.x

1.1 Résumé

L'un des plus importants problèmes non résolus de la géodynamique moderne est le développement de modèles de convection thermique qui sont cohérents avec la dynamique actuelle de l'écoulement mantellique dans la Terre, qui sont en accord avec les images 3-D tomographiques sismiques de la structure interne de la Terre, et qui sont également capables de prédire une évolution temporelle de la structure thermique du manteau que est aussi «réaliste» que possible. Une réalisation réussie de cet objectif donnerait un modèle réaliste de la convection 3-D du manteau qui a une cohérence optimale avec une large suite de contraintes sismiques, géodynamique et minéraux physiques sur la structure du manteau et ses propriétés thermodynamiques. Pour relever ce défi, nous avons élaboré un modèle dépendant du temps de convection compressible en géométrie tridimensionnelle sphérique qui est en accord avec la dynamique instantanée du manteau basée sur la tomographie sismique, en utilisant une méthode numérique pseudo-spectrale actualisée et révisée. La nouvelle caractéristique de nos solutions numériques est

que les équations de conservation de la masse et de la quantité de mouvement sont résolues une fois seulement en termes de fonctions de Green dans le domaine spectral des harmoniques sphériques. Nous traitons initialement la théorie et la méthode numérique utilisée pour résoudre l'équation de conservation de l'énergie thermique, à l'aide de fonctions de Green qui résolvent l'équation du mouvement, avec une attention particulière placée sur la précision numérique et la stabilité des solutions de convection. Une préoccupation importante s'agit de la vérification du bilan énergétique globale dans le contexte de la formulation dissipative et compressible du manteau que nous utilisons. Telle validation est essentielle parce que nous présentons ensuite des solutions de convection contraintes par la géodynamique sur des échelles de temps de milliards d'années, initialisées avec des images thermiques du manteau déduites de la tomographie sismique. L'utilisation de fonctions de Green spectrales contraintes par la géodynamique facilite la modélisation de l'impact dynamique sur l'évolution du manteau de: (1) profils de conductivité thermique dépendant de la profondeur, (2) variations extrêmes de viscosité sur toute la profondeur du manteau, et (3) différentes conditions aux limites de surface, dans ce cas, plaques tectoniques mobiles ou, alternativement, une surface rigide. L'interprétation thermique des modèles de tomographie sismique ne fournit pas un profil radial de la température horizontale moyenne (le géotherme) dans le manteau. Un objectif important de cette étude est donc d'obtenir, en état d'équilibre thermique, un géotherme possédant des couches limites qui satisfait le bilan énergétique du système et fournit un point de départ pour des simulations numériques de l'évolution de la Terre plus réalistes. Nous obtenons des flux de chaleur à la surface qui sont cohérents avec les contraintes terrestres actuelles: 37 TW pour une surface rigide, et 44 TW pour une surface avec des plaques tectoniques couplées à l'écoulement mantellique. En plus, nos simulations de convection donnent des flux de chaleur à la CMB qui se trouvent sur les maxima des valeurs estimées précédemment, à savoir 13 TW et 20 TW, pour des conditions aux limites de surface rigide, et avec plaques tectoniques, respectivement. Nous avons finalement employé ces deux cas limites des conditions aux limites de surface pour explorer l'évolution de la convection sur de très longues échelles de temps, couvrant des milliards d'années. Ces simulations sur milliards d'années nous permettent à déterminer la mesure dans laquelle une mémoire de la structure thermique initiale basée sur la tomographie est préservée et donc à explorer la longévité des

structures 3-D dans le manteau d'aujourd'hui. Les deux conditions aux limites de surface, ainsi que les profils radiaux de viscosité inférés des contraintes géodynamiques, donnent des structures convectives en état d'équilibre qui sont dominés par de longues longueurs d'onde dans le manteau inférieur. Avec la condition de surface rigide on obtient un spectre d'hétérogénéité mantellique dominé par les degrés harmoniques 3 et 4, et avec la condition de surface de type plaques mobiles on obtient une configuration dominé par le degré 1. Notre exploration de la dépendance temporelle de l'hétérogénéité spatiale montre que, pour les deux types de condition aux limites de surface, les profondes remontées mantelliques chaudes qui sont résolues avec le modèle de tomographie sont des caractéristiques durables et stables de la convection terrestre. Ces panaches mantelliques profondément enracinées montrent une longévité remarquable sur de très longues périodes de temps géologiques, principalement en raison de la haute viscosité dans le manteau inférieur inférée avec les données géodynamiques.

1.2 Abstract

One of the outstanding problems in modern geodynamics is the development of thermal convection models that are consistent with the present-day flow dynamics in the Earth's mantle, in accord with seismic tomographic images of 3-D Earth structure, and that are also capable of providing a time-dependent evolution of the mantle thermal structure that is as 'realistic' (Earth-like) as possible. A successful realisation of this objective would provide a realistic model of 3-D mantle convection that has optimal consistency with a wide suite of seismic, geodynamic, and mineral physical constraints on mantle structure and thermodynamic properties. To address this challenge, we have constructed a time-dependent, compressible convection model in three-dimensional spherical geometry that is consistent with tomography-based instantaneous flow dynamics, using an updated and revised pseudo-spectral numerical method. The novel feature of our numerical solutions is that the equations of conservation of mass and momentum are solved only once in terms of spectral Green's functions. We initially focus on the theory and numerical methods employed to solve the equation of thermal energy conservation using the Green's function solutions for the equation of motion, with special attention placed on the numerical accuracy and stability of the convection solutions. A particular concern is the verifica-

tion of the global energy balance in the dissipative, compressible-mantle formulation we adopt. Such validation is essential because we then present geodynamically-constrained convection solutions over billion-year time scales, starting from present-day seismically constrained thermal images of the mantle. The use of geodynamically-constrained spectral Green's functions facilitates the modelling of the dynamical impact on the mantle evolution of: (1) depth-dependent thermal conductivity profiles, (2) extreme variations of viscosity over depth and (3) different surface boundary conditions, in this case mobile surface plates and a rigid surface. The thermal interpretation of seismic tomography models does not provide a radial profile of the horizontally averaged temperature (i.e. the geotherm) in the mantle. One important goal of this study is to obtain a steady-state geotherm with boundary layers which satisfies the energy balance of the system and provides the starting point for more realistic numerical simulations of the Earth's evolution. We obtain surface heat flux in the range of Earth-like values : 37 TW for a rigid surface and 44 TW for a surface with tectonic plates coupled to the mantle flow. Also, our convection simulations deliver CMB heat flux that is on the high end of previously estimated values, namely 13 TW and 20 TW, for rigid and plate-like surface boundary conditions, respectively. We finally employ these two end-member surface boundary conditions to explore the very-long-time scale evolution of convection over billion-year time windows. These billion-year-scale simulations will allow us to determine the extent to which a 'memory' of the starting tomography-based thermal structure is preserved and hence to explore the longevity of the structures in the present-day mantle. The two surface boundary conditions, along with the geodynamically inferred radial viscosity profiles, yield steady-state convective flows that are dominated by long wavelengths throughout the lower mantle. The rigid-surface condition yields a spectrum of mantle heterogeneity dominated by spherical harmonic degree 3 and 4, and the plate-like surface condition yields a pattern dominated by degree 1. Our exploration of the time-dependence of the spatial heterogeneity shows that, for both types of surface boundary condition, deep-mantle hot upwellings resolved in the present-day tomography model are durable and stable features. These deeply-rooted mantle plumes show remarkable longevity over very long geological time spans, mainly owing to the geodynamically-inferred high viscosity in the lower mantle.

1.3 Introduction

Models of the convective flow in Earth's mantle have generally been formulated as either, (1) purely theoretical, time-dependent thermal convection simulations (recent work includes, for example, Davies & Davies (2009); Davies (2005); Tan et al. (2011); Bunge (2005)) that may, in some cases, also include surface geological constraints such as tectonic plate histories (Bunge et al. (1998); McNamara & Zhong (2005); Quéré & Forte (2006); Schuberth et al. (2009b)) and lateral variations in lithospheric strength (Yoshida (2010)), or (2) models of the instantaneous, present-day flow in the mantle based on seismic tomography images of internal Earth structure. An important objective of the latter tomography-based flow modelling is fitting convection-related surface geodynamic data and this has been reviewed by Hager & Clayton (1989) and Forte (2007). Over the past few years, the gap between these approaches is being bridged and it is now feasible to consider a unified approach that fully integrates both types of modelling strategies.

The central guiding principle we adopt here is the derivation of mantle convection models that incorporate as many relevant surface geodynamic and global seismic constraints as possible. This approach involves an interpretation of 3-D seismic tomography models in terms of lateral density heterogeneities which are assumed to provide the internal buoyancy forces which drive convection (Simmons et al. (2007); Simmons et al. (2009)). A second critically important ingredient is a representation of the mantle rheology (effective viscosity) that is derived from inversions of a wide suite of surface geodynamic constraints (Mitrovica & Forte (2004); Forte (2007)).

The assumption of viscous fluid behaviour in the mantle over geological time scales allows the use of the classical hydrodynamic equations of mass and momentum conservation. These equations may be used to calculate the buoyancy driven mantle flow, but this requires an explicit description of mantle rheology. The most common approach to date involves approximating the rheology in terms of an effective depth-dependent viscosity and this permits the derivation of simple solutions of the viscous flow equations which can be represented mathematically in terms of Green's functions or internal loading kernels (e.g., Hager & O'Connell (1981); Richards &

Hager (1984); Ricard et al. (1984); Forte & Peltier (1987); Forte & Peltier (1991)). To be more precise, the Green's or impulse-response functions relate the mantle flow field to an arbitrary field of density perturbations within the mantle and they may be used to derive kernel functions which express the theoretical relationship between internal density anomalies and geodynamic surface observables such as plate motions, surface topography, and geoid or gravity anomalies. The tomography-based flow model can thus be validated by comparing the calculated geodynamic observables with the data provided by surface geophysical observations. The latter may be further used to constrain and refine the viscosity profile of the mantle. Only models which take into account tectonic plates and a significant increase of viscosity in the lower mantle are found to be successful in predicting surface observables (e.g., Forte & Peltier (1987); Forte & Peltier (1991); Forte & Peltier (1994); Hager & Clayton (1989); Ricard & Vigny (1989); Corrieu et al. (1994)).

The mantle viscosity profiles which have been inferred in tomography-based flow studies are not unique (e.g., King (1995a)), and they inherently depend on the choice of the seismic tomography model (not unique either) as well as on the inversion method employed by different authors. The viscosity profiles which are found to give the best agreement with the convection-related data are characterized by strong variations with depth (e.g., Hager & Clayton (1989); Forte et al. (1991); Forte et al. (1993); Ricard & Wuming (1991); King & Masters (1992); King (1995b); Mitrovica & Forte (1997)). In the most recent studies, the inferred viscosity variations with depth span several orders of magnitude (e.g., Forte (2000); Panasyuk & Hager (2000); Forte & Mitrovica (2001); Mitrovica & Forte (2004)).

Although tomography-based models have proven to be very useful to constrain mantle dynamics and to explain the surface observables, they are fundamentally limited to the extent that they only provide an instantaneous description of present-day mantle convection. This limitation has been relaxed in some backward-in-time reconstructions of the tomography-based mantle flow, but only over relatively short geological time intervals (e.g., Steinberger & O'Connell (1997); Forte & Mitrovica (1997); Conrad & Gurnis (2003); Moucha et al. (2008); Spasojevic et al. (2009); Moucha & Forte (2011)). Another fundamental difficulty encountered when using the 3-D tomography images is that they do not provide a corresponding radial profile of the

horizontally averaged mantle temperature (i.e. geotherm). One goal of this study is therefore to obtain an appropriate boundary-layer geotherm which may be employed to carry out more realistic numerical simulations of the Earth's thermal structure.

The mantle convection model that we will develop in this study combines previously developed treatments of time-dependent thermal convection with tomography-based instantaneous flow calculations. Following Glatzmaier (1988) and Zhang & Yuen (1996) we perform a pseudo-spectral time-integration of the temperature field in 3-D spherical geometry but, in contrast to previous studies, we solve the equations of conservation of mass and momentum in the spectral domain using a Green's function approach (Parsons & Daly (1983); Forte & Peltier (1987)). Two main advantages arise from the use of such a method. Firstly, the reformulation of the compressible flow equations in terms of a logarithmic representation of viscosity (Zhang & Christensen (1993); Forte (2000); Panasyuk & Hager (2000)) facilitates the calculation of viscous flow Green's functions for radial viscosity variations of several orders of magnitude without suffering from numerical instabilities. Secondly, the time integration of the 3-D temperature field begins with the temperature anomalies derived from recent seismic tomography models. The thermal convection simulations are therefore intrinsically constrained by global geodynamic data and by seismic tomography models.

Although the models we develop do not include all the complexity of the numerous physical effects which may have an impact on thermal convection dynamics in the real Earth, we suggest that a sufficient number of essential ingredients have been included (e.g., finite compressibility, gravitational consistency, complex radial viscosity variations, coupling to rigid surface plates, depth-dependent thermal conductivity and thermal expansion coefficient). The models we construct are effective tools for investigating the fully 3-D time-dependent dynamics of the mantle which also incorporates joint seismic-geodynamic constraints on mantle properties. In this study we pay special attention to the impact of different surface boundary conditions and depth-dependent mantle viscosity on the spectral (i.e. dominant horizontal wavelength), and global horizontal average (i.e. geotherm) character of mantle convection.

The numerical modelling we carry out in this study is briefly summarised as follows. First, we outline the basic hydrodynamic theory which is relevant to this study, followed by a pre-

sentation of the numerical implementation of the pseudo-spectral method for integrating the governing field equations. Our objective here is to lay out the numerical formulation and implementation as transparently as possible, such that any interested reader will be able to recreate and evaluate the numerical model themselves. We then discuss several basic tests which we performed to validate the model. In this regard, a number of essential benchmark calculations are carried out to confirm the accuracy and validity of the pseudo-spectral approach. We next present a few applications of this model to study thermal convection in the mantle and we consider the global characteristics of these simulations. The main objective in this portion of the study is to determine the influence of different surface boundary conditions and geodynamic inferences of large viscosity increases within the lower mantle on the spectral character and stability of lateral temperature variations in the deep mantle. We then go on to explore the longevity and stability of hot thermal upwellings (i.e. plumes) in the present-day flow field as the model evolves over billion-year time spans. We conclude with a discussion of the main results and limitations of the tomography-based convection modelling presented in this study.

1.4 Numerical Method

1.4.1 Equations for thermal convection in an anelastic, compressible, self-gravitating mantle

The thermal convection model we employ is based on the standard hydrodynamic equations which describe the principles of conservation of mass, momentum and energy for a Newtonian fluid (e.g., Landau & Lifshitz (1959)):

$$\frac{\partial \rho}{\partial t} + \nabla \cdot (\rho \mathbf{u}) = 0 \tag{1.1}$$

$$\rho \frac{d\mathbf{u}}{dt} = \nabla \cdot \boldsymbol{\sigma} + \rho \mathbf{g} \tag{1.2}$$

$$\rho c_p \frac{\partial T}{\partial t} = -\rho c_p \mathbf{u} \cdot \nabla T + \nabla \cdot k \nabla T + \alpha T \frac{dp}{dt} + \Phi + Q \tag{1.3}$$

in which $\mathbf{u}$ is the velocity field, $\boldsymbol{\sigma}$ the stress tensor, $\mathbf{g}$ the gravitational acceleration and ρ the density. The thermodynamical variables involved are the (absolute) temperature T, the pressure p, the specific heat c_p, the thermal conductivity k and the thermal expansion α. The body force

term $\rho \mathbf{g}$ in the conservation of momentum equation (1.2) describes the buoyancy forces which drive mantle flow. In convection modelling these forces are generally assumed to arise from perturbations in density due to lateral variations of temperature inside the mantle. In the equation of energy conservation (1.3), the term $\mathbf{u} \cdot \nabla T$ describes the advection of temperature, $\nabla \cdot k \nabla T$ the diffusion of temperature, Φ is the dissipation due to internal viscous friction, $\alpha T \frac{dp}{dt}$ is the work associated with adiabatic changes of volume, and the last term Q is the internal heating rate per unit volume of fluid (due to distributed radioactive energy sources in the mantle).

An explicit expression for the stress tensor is given by

$$\sigma_{ij} = -p\delta_{ij} + \tau_{ij} \tag{1.4}$$

with

$$\tau_{ij} = \eta\left(u_{i,j} + u_{j,i} - \frac{2}{3}\delta_{ij}u_{k,k}\right) \tag{1.5}$$

where p is the total pressure, δ_{ij} is the identity tensor, τ_{ij} is the deviatoric viscous stress tensor, and η is the dynamic viscosity associated with pure shear (i.e., volume preserving) fluid motion. The notation $u_{i,j}$ represents the partial derivative of the velocity component i along the coordinate axis j. The viscous dissipation rate in eq. (1.3) may be written in terms of the viscous stress tensor as

$$\Phi = \tau_{ij}\dot{\epsilon}_{ij} \tag{1.6}$$

where

$$\dot{\epsilon}_{ij} = \frac{1}{2}(u_{i,j} + u_{j,i} - \frac{2}{3}\delta_{ij}u_{k,k}) \tag{1.7}$$

is the deviatoric strain-rate tensor.

In solving for the mantle flow field that satisfies the equation of momentum conservation (1.2), we incorporate all effects arising from self-gravitation (see section 1.4.2 below) and we must therefore explicitly consider the 3-D variation of gravity throughout Earth's interior. The gravitational acceleration is written as

$$\mathbf{g} = \nabla\varphi \tag{1.8}$$

where φ is Earth's gravitational potential which satisfies Poisson's equation

$$\nabla^2\varphi = -4\pi G\rho \tag{1.9}$$

in which G is the universal gravitational constant. The gravitational potential is expressed as:

$$\varphi = \varphi_0(r) + \varphi_1(r,\theta,\phi) \tag{1.10}$$

where the subscript 0 denotes a hydrostatic reference state, in which the structure of the mantle (density, gravity, pressure, temperature) varies with radius alone, and the subscript 1 denotes all 3-D perturbations arising from the thermal convection process.

The total perturbed density and pressure fields in the mantle may similarly be expressed as:

$$\rho = \rho_0(r) + \rho_1(r,\theta,\phi) \tag{1.11}$$

$$p = p_0(r) + p_1(r,\theta,\phi). \tag{1.12}$$

The equation of state relates the density perturbations to the temperature and pressure perturbations as follows:

$$\rho_1 = \rho_0\left[1 - \alpha T_1 + K^{-1}p_1\right] \tag{1.13}$$

where $T_1 = T - T_0(r)$, $p_1 = p - p_0(r)$, and K is the bulk modulus. The term $T_0(r)$ represents the horizontally averaged temperature (i.e., the geotherm) which varies with radius only. The effects of compressibility on the density are found to be at least two orders of magnitude smaller than the effects of temperature variations. Therefore, the last term of equation (1.13) will be neglected in the study.

Important simplifications are made assuming the anelastic-liquid approximation (e.g., Jarvis & McKenzie (1980); Solheim & Peltier (1990)). This approximation is justified because the velocities associated with mantle convection are very slow compared to the local sound speed and hence acoustic waves cannot be generated by the slow changes in the mantle pressure field. We therefore neglect the time derivative of density in eq. (1.1), thereby eliminating sound waves.

For the same reason, the pressure distribution may be considered (to first-order accuracy) as the pressure of a fluid in hydrostatic equilibrium which yields

$$\frac{dp}{dt} = \frac{\partial p}{\partial t} + \mathbf{u} \cdot \nabla p \simeq -u_r \rho_o g_o. \tag{1.14}$$

The equations are then rewritten in terms of dimensionless variables according to the relations:

$$\begin{gathered} r' = r/d,\ u' = u/U,\ t' = \frac{U}{d}t,\ T' = T/\Delta T,\ \rho' = \rho/\rho_{0s}, \\ g' = g/g_{0s},\ \varphi' = \frac{1}{g_{0s}d}\varphi,\ \alpha' = \alpha/\alpha_s,\ p' = \frac{1}{\alpha_s \Delta T \rho_{0s} g_{0s} d}p, \\ \tau'_{ij} = \frac{1}{\alpha_s \Delta T \rho_{0s} g_{0s} d}\tau_{ij},\ \eta' = \eta/\eta_s,\ k' = k/k_s,\ Q' = \frac{Qd^2}{k_s \Delta T}, \\ \text{with} \quad U = \frac{\rho_{0s} g_{0s} \alpha_s \Delta T d^2}{\eta_s} \end{gathered} \tag{1.15}$$

in which the primes represent the dimensionless variables, the subscript s means that we consider the surface value of the variable to which it is applied. The length scale d and temperature scale ΔT are respectively the depth of the mantle and the difference of temperature between the bottom and the top of the mantle (see Table 2.1). In the following, we will assume that we deal with dimensionless variables and the primes will be dropped for notational convenience.

The dimensionless equation of conservation of momentum is then written as follows:

$$\rho \frac{Ra_s}{Pr_s}\frac{du}{dt} = \frac{\rho}{\alpha_s \Delta T}\nabla\varphi - \nabla P + \nabla \cdot \boldsymbol{\tau} \tag{1.16}$$

in which we introduce the surface Rayleigh Ra_s and Prandtl Pr_s numbers defined, respectively, by:

$$Ra_s = \frac{\rho_{0s}^2 c_p g_{0s} \alpha_s \Delta T d^3}{k_s \eta_s} \tag{1.17}$$

$$Pr_s = \frac{\eta_s c_p}{k_s}. \tag{1.18}$$

Because of the very high viscosity of mantle rocks, the left-hand term in equation (1.16) is smaller than the other terms by several orders of magnitude and may therefore be neglected. This important simplification is called the infinite Prandtl number approximation.

The equation of energy conservation may also be rewritten in terms of the surface Rayleigh number , as follows:

$$\frac{\partial T}{\partial t} = -\mathbf{u}\cdot\nabla T + \frac{1}{\rho Ra_s}\left(\nabla\cdot k\nabla T + Q\right) + \frac{Di}{\rho}\left(-\alpha T\frac{dp}{dt} + \Phi\right) \tag{1.19}$$

where Di is the dissipation number (Peltier (1972)) which measures the importance of compression work and frictional heating, and it is defined as

$$Di = \frac{\alpha_s g_{0s} d}{c_p}. \tag{1.20}$$

Di also measures the ratio of the depth of mantle convection (d) to the adiabatic scale height ($c_p/\alpha g_0$) and for whole-mantle convection is close to order 1 (Jarvis & McKenzie (1980)).

After all simplifications, the dimensionless system of governing equations is written as:

$$\nabla\cdot(\rho_0\mathbf{u}) = 0 \tag{1.21}$$

$$\frac{\rho}{\alpha_s\Delta T}\nabla\varphi - \nabla p + \nabla\cdot\boldsymbol{\tau} = 0 \tag{1.22}$$

$$\frac{\partial T}{\partial t} = -\mathbf{u}\cdot\nabla T + \frac{1}{\rho_0 Ra_s}\left(\nabla\cdot k\nabla T + Q\right) + \frac{Di}{\rho_0}\left(-\alpha T\rho_0 g_0 u_r + \Phi\right). \tag{1.23}$$

Other equations are

$$\nabla^2\varphi = -4\pi G\rho \tag{1.24}$$

$$\tau_{ij} = \eta\left(u_{i,j} + u_{j,i} - \frac{2}{3}\delta_{ij}u_{k,k}\right) \tag{1.25}$$

$$\rho_1 = \rho_0\left[1 - \alpha T_1\right]. \tag{1.26}$$

The perturbations ρ_1 have been neglected in the equations of conservation of mass (1.21) and energy (1.23) as their contribution is only a second-order perturbation.

1.4.2 A spectral solution of the gravitationally consistent equations of mass and momentum conservation

As discussed above, we may solve the equations governing buoyancy-induced viscous flow in a mantle with infinite Prandtl number using a Green's function method. This approach, widely employed in tomography-based mantle flow modelling (e.g., Forte & Peltier (1987); Forte & Peltier (1991); Hager & Clayton (1989); Ricard & Vigny (1989)), was first used extensively by Hager & O'Connell (1981) and is often referred to as the 'internal loading' formalism. The principal feature of this internal loading approach, which sets it apart from the traditional solution of momentum and mass conservation in numerical convection models (e.g., Glatzmaier (1988); Tackley (1997)), is that the solutions are obtained entirely in the spectral domain using orthonormal basis functions appropriate for spherical geometry (i.e., spherical harmonics).

In the present study, we employ the spectral method for solving the equations of mass and momentum conservation (eq. 1.21- 1.22) in 3-D spherical geometry, using the viscosity-renormalised flow variables employed by Zhang & Christensen (1993) and Forte (2000). This spectral method provides a gravitationally consistent solution for viscous flow in a compressible spherical mantle. A similar approach was followed by Panasyuk et al. (1996). A brief overview of the method is presented here and we refer to Forte (2000) and Forte (2007) for more details.

The method is based on the theory of generalized spherical harmonics developed by Phinney & Burridge (1973). All vector and tensor fields (e.g., velocity, stress) are expressed in the coordinate system defined by the complex basis vectors $(\mathbf{e}_-, \mathbf{e}_0, \mathbf{e}_+)$, where

$$\begin{aligned} \mathbf{e}_- &= \frac{1}{\sqrt{2}}(\mathbf{e}_\theta - i\mathbf{e}_\phi) \\ \mathbf{e}_0 &= \mathbf{e}_r \\ \mathbf{e}_+ &= \frac{1}{\sqrt{2}}(-\mathbf{e}_\theta - i\mathbf{e}_\phi) \end{aligned} \tag{1.27}$$

where $(\mathbf{e}_r, \mathbf{e}_\theta, \mathbf{e}_\phi)$ are the usual unit basis vectors in a spherical polar coordinate system.

The velocity and stress components in this new, rotated coordinate system are expanded in

terms of the generalized spherical functions $Y_\ell^{N\,m}$ such that:

$$
\begin{aligned}
u^{-}(r,\theta,\phi) &= \sum_{\ell,m} U_\ell^{-\,m}(r)\, Y_\ell^{-1\,m}(\theta,\phi) \\
u^{0}(r,\theta,\phi) &= \sum_{\ell,m} U_\ell^{0\,m}(r)\, Y_\ell^{0\,m}(\theta,\phi) \\
u^{+}(r,\theta,\phi) &= \sum_{\ell,m} U_\ell^{+\,m}(r)\, Y_\ell^{+1\,m}(\theta,\phi) \qquad (1.28) \\
\sigma^{\alpha\beta}(r,\theta,\phi) &= \sum_{\ell,m} \mathsf{T}_\ell^{\alpha\beta m}(r)\, Y_\ell^{(\alpha+\beta)\,m}(\theta,\phi) \quad (\alpha,\beta = -1,0,+1). \qquad (1.29)
\end{aligned}
$$

All simple scalar (order 0 tensor) fields involved in the governing equations (1.21-1.26) are expanded in terms of ordinary spherical harmonics. For example,

$$
\begin{aligned}
\rho_1(r,\theta,\phi) &= \sum_{\ell,m} (\rho_1)_\ell^m(r)\, Y_\ell^m(\theta,\phi) \\
\varphi_1(r,\theta,\phi) &= \sum_{\ell,m} (\varphi_1)_\ell^m(r)\, Y_\ell^m(\theta,\phi) \qquad (1.30)
\end{aligned}
$$

where $Y_\ell^m \equiv Y_\ell^{0\,m}$.

As described by Forte & Peltier (1991) and Forte (2000), a spectral decomposition of the equations of conservation of mass and momentum in a self-gravitating mantle (1.21, 1.22, 1.24) yields a system of six, coupled, first-order, ordinary differential equations:

$$
\frac{d}{dr}\begin{pmatrix} \mathsf{V}^{\mathrm{o}} \\ \mathsf{V}^{\mathrm{p}} \\ \mathsf{T}^{\mathrm{o}} \\ \mathsf{T}^{\mathrm{p}} \\ \phi_1 \\ \gamma_1 \end{pmatrix} = \begin{pmatrix}
-\frac{1}{r}(2+\Lambda_\rho-\Lambda_\eta) & \frac{\Omega_1}{r} & 0 & 0 & 0 & 0 \\
-\frac{2\Omega_1}{r} & \frac{1}{r}(1+\Lambda_\eta) & 0 & 1 & 0 & 0 \\
\frac{4}{r^2}(3+\Lambda_\rho) & -\frac{6\Omega_1}{r^2} & 0 & \frac{\Omega_1}{r} & \left(\frac{1}{\alpha_s \Delta T}\right)\frac{1}{r^2}\Lambda_\rho & 0 \\
-\frac{4\Omega_1}{r^2}(3+\Lambda_\rho) & 2\left(\frac{\Omega_2^2+3\Omega_1^2}{r^2}\right) & -\frac{2\Omega_1}{r} & -\frac{3}{r} & 0 & 0 \\
0 & 0 & 0 & 0 & \frac{1}{r}(1+\Lambda_\rho) & \frac{1}{r} \\
0 & 0 & 0 & 0 & \frac{2\Omega_1^2}{r} & \frac{1}{r}\Lambda_\rho
\end{pmatrix}\begin{pmatrix} \mathsf{V}^{\mathrm{o}} \\ \mathsf{V}^{\mathrm{p}} \\ \mathsf{T}^{\mathrm{o}} \\ \mathsf{T}^{\mathrm{p}} \\ \phi_1 \\ \gamma_1 \end{pmatrix} +
$$

$$\begin{pmatrix} 0 \\ 0 \\ \frac{g_0(r)}{\alpha_s \Delta T}\rho_1(r) \\ 0 \\ 0 \\ \frac{-3r^2 \rho_0(r)\, d}{\rho_e r_e}\rho_1(r) \end{pmatrix} \tag{1.31}$$

in which $\Omega_1 = [\ell(\ell+1)/2]^{1/2}$, $\Omega_2 = [(\ell-1)(\ell+2)/2]^{1/2}$, r_e is Earth's mean radius (6371 km), ρ_e is Earth's mean density (5.5143×10^3 kg/m^3), and

$$\Lambda_\rho = r\frac{d}{dr}\ln\left[\frac{\rho_0(r)}{\rho_{0s}}\right] \text{ and } \Lambda_\eta = r\frac{d}{dr}\ln\left[\frac{\eta(r)}{\eta_s}\right]. \tag{1.32}$$

The dimensionless flow variables $V^o(r)$, $V^p(r)$, $T^o(r)$, $T^p(r)$, $\phi_1(r)$, and $\gamma_1(r)$ represent the spherical harmonic coefficients of vertical flow, tangential flow, vertical (radial) stress, tangential stress, perturbed gravitational potential, and perturbed gravitational acceleration, respectively. These flow and stress variables characterise the purely poloidal component of the mantle flow field which is driven by the density anomalies ρ_1. The generation of toroidal flow requires that the effective viscosity in the mantle vary laterally in addition to varying with depth, as assumed in the system (1.31). As shown below, surface tectonic plates are effectively a manifestation of lateral viscosity variations (e.g., Forte & Peltier (1994)) which will generate significant toroidal flow in the (especially, upper) mantle.

The flow, stress and gravity variables in the poloidal-flow system (1.31) are all dependent on the same harmonic degree ℓ and order m (this dependence has been dropped for notational convenience). The dependence of these variables on the harmonic coefficients of flow (1.28),

stress (1.29), and gravitational potential (1.30) are:

$$
\begin{aligned}
\mathsf{V}^{\mathsf{o}} &= \eta(r)\, U^{0}(r) \\
\mathsf{V}^{\mathsf{p}} &= \eta(r)\, [U^{+}(r) + U^{-}(r)] \\
\mathsf{T}^{\mathsf{o}} &= \mathsf{T}^{00}(r) + \frac{\rho_0(r)}{\alpha_s \Delta T}\, \varphi_1(r) \\
\mathsf{T}^{\mathsf{p}} &= \mathsf{T}^{0+}(r) + \mathsf{T}^{0-}(r) \\
\phi_1 &= r\, \rho_0(r)\, \varphi_1(r) \\
\gamma_1 &= r^2\, \rho_0(r)\, \frac{d\varphi_1(r)}{dr} \, .
\end{aligned}
\tag{1.33}
$$

In the flow system (1.31) we note the dependence on viscosity is through the quantity Λ_η defined in (1.32). As shown in Forte (2000), this dependence on the logarithm of the radial viscosity profile is a consequence of the use of 'pseudo-flow' variables V^{o} and V^{p} defined in (1.33) and first used by Zhang & Christensen (1993). With this logarithmic dependence on viscosity, it is possible to numerically resolve extremely large variations in viscosity. This is particularly important when we consider the viscosity profiles obtained in recent geodynamic studies (Forte & Mitrovica (2001) and Mitrovica & Forte (2004)), which are characterized by radial variations of 3 orders of magnitude over a few hundred kilometres.

The effects of self-gravitation on buoyancy-induced mantle flow are represented by the term $\left(\frac{1}{\alpha_s \Delta T}\right) \frac{1}{r^2} \Lambda_\rho$ appearing in the (3rd row, 5th column of the) flow matrix in system (1.31). In an incompressible mantle this coupling between gravity and flow is absent, while in a compressible mantle the perturbed gravity field deflects the level surfaces in the hydrostatic reference state giving rise to effective 'loads' which are superimposed on the primary driving force due to the density anomalies ρ_1. The impact of these self-gravitational loads are not negligible when considering the longest horizontal wavelength components of the flow field, especially the flow-related surface observables such as dynamic topography and geoid anomalies (Forte & Peltier (1991)). In particular, when considering the component of the flow field corresponding to harmonic degree ℓ=1, a gravitationally consistent solution of system (1.31) will ensure that the predicted ℓ=1 component of the external gravitational potential (i.e., the dipole component of the geoid field) is zero. This result, which ensures that the centre of mass of the Earth will not

be displaced, is included in our mantle convection model.

The viscous flow solution is represented in terms of Green's functions which relate the flow velocity and the stress tensor at radius $r = r_0$ to a delta-function density load at $r = r'$. The system (1.31) is thus integrated for $\rho_1(r) = \delta(r - r')$ after appropriate boundary conditions are applied at the surface and at the CMB (see Forte (2007) for details). Zhang & Yuen (1996) have employed a system of spectral poloidal-flow equations, analogous to those in (1.31), but use a finite-difference method to solve these equations for a given field of density anomalies $\rho_1(r, \theta, \phi)$ distributed throughout the mantle.

Tectonic plates are a fundamental part of mantle convection in the Earth and, though their treatment lies beyond classical fluid mechanics theory, their dynamical impact should be modelled. A key issue in developing a procedure for coupling plates to the mantle flow field is to ensure that the plate motions, at each instant, are produced by the underlying buoyancy-driven flow and not vice-versa (i.e. the 'Hand of God' approach in which plate motions are prescribed). This concern is especially important when modelling convection over very long time spans, for example over many hundreds of millions of years as presented below, because externally-forced plate motions imply the addition of a non-physical energy source that is extraneous to the convecting system and this will compromise the energy balance of the mantle. We therefore employ a technique for coupling the motions of rigid surface plates to buoyancy induced mantle flow which was developed by Forte & Peltier (1991) and Forte & Peltier (1994). An alternative, conceptually distinct approach has been developed by Ricard & Vigny (1989), based on the earlier plate modelling work of Hager & O'Connell (1981). A complete mathematical description of the plate modelling theory we employ here is provided by Forte & Peltier (1994) and we will summarise only the main aspects of this method.

It may be shown that for a given geometry of surface plates, the internal density anomalies $\rho_1(r, \theta, \phi)$ are partitioned into two families:

$$\rho_1(r, \theta, \phi) = \hat{\rho}_1(r, \theta, \phi) + \bar{\rho}_1(r, \theta, \phi) \tag{1.34}$$

where the density perturbations $\hat{\rho}_1(r, \theta, \phi)$ are obtained through a projection operator $\hat{P}$ as fol-

lows:

$$\hat{\rho}_1{}^t_s(r) = \hat{P}_{st,lm}(r)\, \rho_1{}^m_l(r)\,. \tag{1.35}$$

The calculation of the projection operator $\hat{P}_{st,lm}(r)$ is given in Forte & Peltier (1994) and it depends on the geometry of the surface plates. The other component of the density anomalies $\bar{\rho}_1(r,\theta,\phi)$ is simply given by the expression:

$$\bar{\rho}_1{}^t_s(r) = \rho_1{}^t_s(r) - \hat{\rho}_1{}^t_s(r)\,. \tag{1.36}$$

As Forte & Peltier (1994) show, the poloidal mantle flow field produced by the component $\hat{\rho}_1$ is consistent with the geometry of possible rigid plate motions at the surface whereas the one produced by $\bar{\rho}_1$ is orthogonal to any possible plate motion. In other words, the plates participate in the underlying flow driven by $\hat{\rho}_1$, while they resist the flow produced by $\bar{\rho}_1$. Hence, free-slip ($\mathrm{T}^{\mathrm{P}}(r_s) = 0$) and no-slip ($\mathrm{V}^{\mathrm{P}}(r_s) = 0$) surface boundary conditions are applied to model the internal flows driven by $\hat{\rho}_1$ and $\bar{\rho}_1$, respectively.

The plate motions which result from poloidal mantle flow driven by the density anomalies $\hat{\rho}_1(r,\theta,\phi)$ will necessarily possess a toroidal component. This toroidal component is directly coupled to the poloidal component of the plate motions as follows:

$$(\hat{\boldsymbol{r}} \cdot \nabla \times \mathbf{v})^t_s = C_{st,lm}\ (\nabla_H \cdot \mathbf{v})^m_l \tag{1.37}$$

in which the spherical harmonic coefficients of the radial vorticity of the plate velocity field $\mathbf{v}$ are linearly dependent on the harmonic coefficients of the horizontal divergence of the plate motions. The vorticity and divergence fields are themselves directly dependent on the toroidal and poloidal scalar representations, respectively, of the plate velocity field (Forte & Peltier (1987)). The coupling matrix $C_{st,lm}$ in (1.37) is dependent only on the geometry of the plates (Forte & Peltier (1994)).

Viscous coupling between the plates and underlying mantle will result in the downward (viscously 'diffuse') propagation of the surface toroidal flow into the mantle. In analogy to the poloidal flow system (1.31), the equations governing toroidal flow are determined through

a spectral decomposition of the conservation of momentum equations, resulting in a coupled system of equations which are virtually identical to those describing elastic toroidal normal modes in seismology (e.g., Phinney & Burridge (1973)):

$$\frac{d}{dr}\begin{pmatrix} \mathsf{V}^{\mathsf{t}} \\ \mathsf{T}^{\mathsf{t}} \end{pmatrix} = \begin{pmatrix} \frac{1}{r}\left(1+\Lambda_\eta\right) & 1 \\ \frac{2\Omega_2^2}{r^2} & -\frac{3}{r} \end{pmatrix}\begin{pmatrix} \mathsf{V}^{\mathsf{t}} \\ \mathsf{T}^{\mathsf{t}} \end{pmatrix} . \tag{1.38}$$

The dimensionless flow and stress variables in this toroidal-flow system are related to the harmonic coefficients of the flow (1.28) and stress (1.29) fields as follows:

$$\begin{aligned} \mathsf{V}^{\mathsf{t}} &= \eta(r)\,[U^{+}(r) - U^{-}(r)] \\ \mathsf{T}^{\mathsf{t}} &= \mathsf{T}^{0+}(r) - \mathsf{T}^{0-}(r)\,. \end{aligned} \tag{1.39}$$

The system (1.38) is integrated downwards from the surface after appropriate boundary conditions are applied at the surface and at the CMB. The surface boundary condition requires that the toroidal mantle flow match the toroidal component of plate motions, which is equivalent to their radial vorticity (1.37):

$$\mathsf{V}^{\mathsf{t}}(r_s) = \eta_s \frac{\imath r_s}{\Omega_1}\left(\hat{\boldsymbol{r}}\cdot\nabla\times\mathbf{v}\right)_l^m \tag{1.40}$$

where $\imath = \sqrt{-1}$. A free-slip condition ($\mathsf{T}^{\mathsf{t}} = 0$) is applied at the CMB.

The Green's function solutions of the poloidal and toroidal flow equations (1.31, 1.38), obtained for a delta-function load $\rho_1(r) = \delta(r - r')$, may be used to describe the viscous response of the mantle to an arbitrary distribution of internal density anomalies ρ_1 as follows:

$$\begin{pmatrix} \mathsf{U}_\ell^{\alpha\, m}(r,t) \\ \mathsf{T}_\ell^{\alpha\beta\, m}(r,t) \end{pmatrix} = \int_{r_{\mathrm{cmb}}}^{r_s} \begin{pmatrix} \mathsf{U}_\ell^{\alpha}(r,r') \\ \mathsf{T}_\ell^{\alpha\beta}(r,r') \end{pmatrix} \rho_{1\ell}^{\,m}(r',t)\,dr' \tag{1.41}$$

where $\mathsf{U}_\ell^{\alpha\, m}(r,t)$ and $\mathsf{T}_\ell^{\alpha\beta\, m}(r,t)$ are the generalized spherical harmonic coefficients of the velocity and stress fields (1.28, 1.29), respectively, and $\mathsf{U}_\ell^{\alpha}(r,r')$ and $\mathsf{T}_\ell^{\alpha\beta}(r,r')$ are the corresponding Green's functions.

The Green's functions do not depend on time, nor on the azimuthal harmonic order m (owing to the assumed radial symmetry of viscosity in the mantle). In contrast, the thermally generated density heterogeneities will vary with time according to equations (1.23) and (1.26). Hence, the Green's functions are calculated only once and then stored. At every time step, the velocity and the stress fields will be determined simply by numerically integrating the Green's functions in (1.41) with the time-dependent density anomalies. This approach, namely to solve the conservation of momentum equation once in terms of Green's functions, rather than solving them at every time step (e.g., Glatzmaier (1988); Zhang & Yuen (1996)), is an efficient means of solving the thermal convection problem. In effect, the entire thermal convection problem has been reduced to solving one equation only: the conservation of energy equation.

1.4.3 Solving the equation of conservation of energy

1.4.3.1 Pseudo-spectral method

Several methods have been used by different authors to perform the time-integration of the energy equation, the most common of which are finite differences (e.g., McKenzie et al. (1974); Jarvis & McKenzie (1980); Solheim (1986); Machetel & Yuen (1986); Larsen et al. (1997)) and finite elements (Baumgardner (1985); King et al. (1990); van Keken et al. (1994); Bunge & Richards (1996); Kellogg & King (1997); van Keken & Ballentine (1999); Zhong et al. (2000)). Glatzmaier (1984); Glatzmaier (1988) employed a pseudo-spectral method and showed that, in the case of a three-dimensional spherical model, this method presented numerical advantages and may be less time and memory consuming. In particular, the 'pole problem' (Orszag (1974); Glatzmaier (1988)) which arises in finite differences is absent. If the mesh used for finite differences is such that the number of longitudinal points is the same at each latitude then the distance between successive points near the poles tends toward zero. In consequence, the time step for the evolution of temperature must be extremely short in order to maintain numerical stability (see the Courant stability criterion below in eq. 1.74), which results in a very large number of iterations. This problem does not arise if the equations are solved in the spectral domain of the spherical harmonics. Furthermore, comparison tests between spectral and finite difference methods have been completed by several authors (Orszag (1971); Herring et al. (1974); Glatzmaier (1984))

who all showed that spectral methods require fewer grid points, hence less memory, for achieving the same accuracy. Although the finite element method is very flexible and does not present the pole problem, we opt for the pseudo-spectral method which is straightforward to implement (Glatzmaier (1988); Zhang & Yuen (1996)).

The method employed here is similar to the one described by Glatzmaier (1984), but with some notable differences. For the sake of clarity, we will outline the procedure below and we relegate most of the mathematical details to Appendix 1.A. The main idea consists of solving the equation in the spectral domain spanned by the spherical harmonic basis functions. The orthogonal property of the spherical harmonic functions Y_ℓ^m allows us to solve the energy conservation equation (1.23) for each degree ℓ, m independently:

$$\frac{\partial T_\ell^m}{\partial t} = -(\mathbf{u}\cdot\nabla T)_\ell^m + \frac{1}{\rho_0 Ra_s}\left[(\nabla\cdot k\nabla T)_\ell^m + Q_\ell^m\right] + \frac{Di}{\rho_0}\left[-\alpha\rho_0 g_0 (Tu_r)_\ell^m + \Phi_\ell^m\right]. \quad (1.42)$$

Therefore, instead of solving one equation in four dimensions (r, θ, ϕ, t), we solve $L(L+1)/2$ independent equations in two dimensions (r, t), where L is the maximum degree of our expansion in spherical harmonics.

At every time step, the solution of the energy equation consists of the set of all coefficients T_ℓ^m of the temperature field for all depths in the mantle. The relation between the coefficients and the spatial temperature field is:

$$T(r,\theta,\phi,t) = \sum_{\ell=0}^{L}\sum_{m=-\ell}^{+\ell} T_\ell^m(r,t)Y_\ell^m(\theta,\phi)\,. \quad (1.43)$$

All expansions in spherical harmonics are numerically computed by performing Fast Fourier Transforms (FFT's) in longitude and Gauss-Legendre integration in latitude. Therefore, the temperature field is expressed on a grid formed of Gaussian nodes in latitude and equally-spaced points in longitude. In the radial direction the temperature is interpolated on Chebyshev depth nodes. These nodes are not uniformly spaced and are more densely concentrated near the upper and lower boundaries. This results in a higher resolution of the temperature variations across the thermal boundary layers (TBL), which is desirable because the TBL are the main sources of convective instabilities. The use of Chebyshev depth nodes also permits use of FFT's to readily

decompose the temperature coefficients T_ℓ^m into series of Chebyshev polynomials (Glatzmaier (1984)). This provides an accurate and efficient means of calculating the radial derivatives of temperature in (1.42).

The solution of equation (1.42) requires us to first obtain the spherical harmonic coefficients of the terms on the right-hand side. Only the diffusion term can be calculated directly in the spectral domain of the spherical harmonics, while the advection and dissipation terms are first calculated in the spatial domain (r, θ, ϕ) and then transformed to the spectral domain (hence the use of the term 'pseudo-spectral' to describe this method). The procedure we employ to compute the different terms in physical space is simplified by using generalized spherical harmonics (Phinney & Burridge (1973)) rather than ordinary spherical harmonics (e.g., Glatzmaier (1984)). More details may be found in Appendix 1.A.

1.4.3.2 Time-integration of temperature

The numerical scheme used by Glatzmaier (1984) and Glatzmaier (1988) to perform the time-integration of the energy equation is composed of two parts. The Adams-Bashforth scheme used by Glatzmaier is just the predictor part of the two-part predictor-corrector method. We instead use the complete predictor-corrector scheme in order to increase the accuracy of our results. Every iteration performing the Adams-Bashforth scheme will be followed and 'corrected' by an iteration performing the Adams-Moulton scheme for the non-linear terms (advection and dissipation terms) while a semi-implicit Crank-Nicolson scheme is used for the diffusion terms. Both schemes are second-order accurate in time and they are discussed in detail by Glatzmaier (1984). However, numerical experiments (e.g., Glatzmaier (1984); Ascher et al. (1995)) demonstrate that weak decay of high frequency modes can lead to appearance of aliasing in such constructed implicit-explicit (IMEX) schemes. Glatzmaier (1984) has proposed using a simple method of 'cutting' one half of the radial Chebyshev polynomials in the spectral domain, but with this method we lose the ability to perfectly satisfy isothermal boundary conditions.

Ascher et al. (1995) have shown that strongly damped schemes, such as SBDF (semi-implicit backward differentiation formula), MCNAB (modified Crank-Nicolson, Adam-Bashforth), or third-order SBDF can be used to inexpensively reduce aliasing. Here, we use the modified

Crank-Nicolson for the diffusion terms which allows us to use the full Chebyshev spectrum. The numerical schemes employed to solve the energy conservation equation are described in detail in Appendix 1.A.4.

1.4.4 Determination of a geotherm - the energy balance criterion

One of our goals is to determine a geotherm which satisfies the bulk energy balance in the mantle, i.e. the difference between the heat exiting and entering the mantle must be due to a combination of the mass-integrated internal radioactive heating and secular cooling within the mantle,

$$F_{surf} - F_{cmb} = 4\pi \int_{r_{cmb}}^{r_{surf}} \rho_0(r) H_0 r^2 dr - c_p \frac{d}{dt} 4\pi \int_{r_{cmb}}^{r_{surf}} \rho_0(r) T_0 r^2 dr \,. \qquad (1.44)$$

To determine a representative horizontal average of the temperature field (i.e., the geotherm), we chose to iterate the energy equation until we achieve a steady-state and this is only valid when the estimated secular cooling within the mantle tends to 0 TW and the calculated rate of total internal heating, using expression (1.44), is equal to the total imposed internal heating. To be sure that the system is not in a transient period, these criteria or one of them, have to be satisfied over a significant period of time (so-called statistical steady-state).

Secular cooling provides a measure of geotherm deviation from a steady-state and its value may be used to tell us: (1) how far we are from the system equilibrium at any one moment, and (2) the amount of numerical error of a determined geotherm at the end of calculation. We employ the steady-state geotherm as an estimate of the present-day geotherm in Earth's mantle, in which we underline that the total imposed internal mantle-heating rate includes both radiogenic and geologic estimates of secular cooling contributions.

1.5 Initial conditions and reference properties of the mantle

We use a seismic-tomography image of present-day mantle heterogeneity which satisfies both seismic and geodynamic constraints (Simmons et al. (2009)) as the initial laterally-varying temperature field for all simulations. This model fits 93%, 92%, 99% and 82% of seismic, gravity,

tectonic plate-divergence and topography data, respectively. Also, the resolution of the original 3-D image is defined by 22 layers in the radial direction, and 128 spherical harmonics in the horizontal direction.

For the purpose of this study, we use two different viscosity profiles: (1) V2-profile employed by Forte et al. (2010) and determined by jointly inverting convection-related surface observables (surface gravity anomalies, residual topography, divergence of tectonic plate motions, excess ellipticity of the core-mantle boundary) and data associated with the response of the Earth to ice-age surface mass loading (decay times inferred from post-glacial sea-level histories in Hudson Bay and Fennoscandia, and the Fennoscandian relaxation spectrum), and (2) ISOV-profile, i.e. constant viscosity profile, $\eta = 5.36 \times 10^{21}$Pa.s (the depth-average value of the V2 viscosity), used to establish benchmark simulations that characterise the numerical stability of our solution scheme. The viscosity profiles are presented in Fig. 1.1.

The radial density profile $\rho_0(r)$ which describes the reference hydrostatic state in our compressible convection model is taken directly from the seismic reference Earth model PREM (Dziewonski & Anderson (1981)). The corresponding radial gravity field $g_0(r)$ is obtained by integrating $\rho_0(r)$.

We employ a constant heat capacity $c_p = 1.25 \times 10^3 \mathrm{Jkg^{-1}K^{-1}}$.

The coefficient of thermal expansion $\alpha(r)$ is assumed to vary linearly from a value of $3.5 \times 10^{-5}\ \mathrm{K^{-1}}$ at the top of the mantle to a value of $2.5 \times 10^{-5}\ \mathrm{K^{-1}}$ at 670 km depth. This variation across the upper mantle approximates that found in equation of state modelling for a pyrolite mantle composition (Stacey (1998); Jackson (1998)). In the lower mantle we assume that the depth variation of $\alpha(r)$ follows the dependence on density (or molar volume) found by Chopelas & Boehler (1992), decreasing from a value of $2.5 \times 10^{-5}\ \mathrm{K^{-1}}$ at 670 km depth to $1.0 \times 10^{-5}\ \mathrm{K^{-1}}$ at the core-mantle boundary (CMB).

The values of these thermodynamic input parameters are deemed to be acceptable for the upper part of the mantle by laboratory experiments and inferences from geophysical data analysis. The thermal conductivity of upper mantle is in the range 3.0 – 3.3 $\mathrm{Wm^{-1}K^{-1}}$. But with increasing depth our knowledge of these parameters becomes increasingly uncertain, especially for the thermal conductivity because at high temperatures and pressures the total conductivity

is the sum of contributions from several independent mechanisms. In this study we employ a thermal conductivity k, henceforth called the 'H-profile' that considers the effect of thermal boundary layers inside the mantle and the possibility that thermal conductivity decreases with depth across both layers (Hofmeister (1999)). The H-profile has k decreasing inside the upper thermal boundary layer from 3.3 $\mathrm{Wm^{-1}K^{-1}}$ to 2.5 $\mathrm{Wm^{-1}K^{-1}}$, and at the top of the D"-layer k takes the maximum value of 6.25 $\mathrm{Wm^{-1}K}$, while at the CMB its value is 4.8 $\mathrm{Wm^{-1}K^{-1}}$.

As noted above in the discussion of the geotherm, we employ a total value of internal heating that is the sum of two components: radioactive sources (12 TW) and estimated secular cooling (12 TW).

The temperature increase across the mantle is 3000 K: from 300 K at the top of the mantle to 3300 K at the bottom of the mantle.

The physical parameters and values employed in the simulations of mantle convection are summarised in Table 1.1.

There are three types of boundary conditions that we may use for modelling thermal convection in the mantle: rigid surface (R), free-slip (F) and coupling with rigid surface tectonic plates (P). In this study we used two of them: the R- and P-boundary conditions. P-boundary condition involves the present-day geometry of the major tectonic plates and modelling the plate-coupling to mantle flow is carried out in the no-net rotation reference frame. One important difference between them is that the P-boundary condition involves the generation of toroidal flow via the surface-plate rotations and this is not the case in either of the two other boundary conditions (R or F). Moreover, the coupling of surface plates employing the P-boundary condition requires a consideration of both rigid and free-slip flow kernels and hence this condition is, in a sense, intermediate between the R- and F-boundary conditions.

For the purpose of exploring the importance and implications of surface boundary conditions on the evolution of thermal convection in the mantle, we consider the following models: (1) the M2-HP model using V2-viscosity and P-boundary condition at the mantle top, (2) the M2-HR model defined by V2-viscosity and R-boundary condition. We will, however, begin by considering an iso-viscous mantle convection simulation, the MI model, in order to validate the numerical procedures discussed above and to clarify the appropriate spatial resolution needed

for so-called 'Earth-like' conditions.

1.6 Results

1.6.1 Numerical issues in the upper part of the mantle

We constructed our initial model, MI, using the iso-viscous profile (ISOV), the present-day seismic-tomographic image of the mantle and coupled surface plates (P-boundary) condition. Because the 3-D tomographic images provide only lateral variations of temperature, and hence the global horizontal average value of mantle temperature is not constrained by seismic tomography, we are forced to design an initial estimated geotherm with 3 piecewise-linear segments (one for each boundary layer and one for the interior of the mantle).

Our objective in constructing such a geotherm is to integrate the 'Earth-like' adiabat between two TBLs. Constrained by the radial Chebyshev (non-uniform) representation we are not able to impose the exact reference adiabatic values of geotherm (1700-2584 K estimated on the basis of mineral physics constraints (Boehler & Chopelas (1991))) ending up with 1770 K at the bottom of the upper TBL and 2630 K at the top of the lower TBL.

The initial estimate of the geotherm overheats the system, because the imposed internal heating of 24 TW is less than the internal heating implied by the thermal boundary layers that instantaneously produce 48 TW (at the surface) and 14 TW (at the CMB), i.e. $Q_0 = F_{surf} - F_{cmb} = 48 - 14 = 34$ TW. Taking the average value of the thermodynamic parameters (ρ, k, α and g) and using the following formula to calculate the internal-heating Rayleigh number

$$Ra_H = \frac{g\rho^2 c_p \alpha Q d^5}{\eta k^2} \tag{1.45}$$

we obtained $Ra_H > 10^9$ for the initial MI-model. To illustrate numerical issues in the upper part of the mantle we carry out four different MI-simulations with the P-boundary (plates) condition.

The vertical resolution is defined with an order 129 Chebyshev polynomial expansion which translates into a radial-resolution length scale of 0.43 km near the isothermal boundaries to 35.44 km in the middle of mantle. This vertical resolution will be kept for all simulations presented in this study.

The first pair of simulations (MI-F128 and MI-N128) is based on the original MI-model and horizontally discretised by 128 spherical harmonic degrees, L=128, giving us the horizontal spatial resolution from 85.1 km at the CMB to 155.7 km at the top of the mantle. The only difference between these simulations is that MI-F128 uses the isotropic linear filter (see Appendix eq. (1.75)) applied to the spectral expansion of the non-linear convection term over spherical harmonic degree, while MI-N128 is not filtered.

Multiplying by 10 the iso-viscous profile we obtain a new model, MIx10, characterized by $Ra_H < 10^9$, which is used as the basis for the second pair of simulations (MIx10-N128 and MIx10-N256). Both numerical experiments, MIx10-N128 and MIx10-N256, are calculated without the filtering in the spectral domain, but with different horizontal resolution: L=128 for MIx10-N128 and L=256 for MIx10-N256.

We integrated MI-F128 over a model-time interval of 3.845 Gyr (corresponding to 36,000 time steps), and then we chose the 3-D temperature structure at that point in time to be an initial field for three remaining models (MI-N128, MIx10-N128 and MIx10-N256). Integrating all previously defined iso-viscous simulations over a time window of 290 Myr, we obtained the results discussed below.

First, we note that a numerical thermal instability in the horizontal part of the spectrum developed inside the upper boundary layer from the very beginning of both L=128 numerical experiments with no filter (Figs 1.2a and 1.2b). This type of instability is caused by the lack of horizontal resolution, because the MIx10-N256 model (with increased horizontal spectrum) does not generate an accumulation of energy on the shortest wavelengths (compare Fig. 1.2c with Fig. 1.2b). It seems that L=256 provides the minimal horizontal resolution needed to solve for mantle convection defined by $Ra_H \leq 10^9$ without aliasing over spherical harmonic degrees. If more 'Earth-like' conditions correspond to $Ra_H > 10^9$ (most likely in the upper-mantle, where sub-lithospheric viscosity is lowest), this suggests that we probably have to use $L \geq 512$, as pointed out by Schuberth et al. (2009b).

Second, analysing the lower mantle, we note the absence of any numerical issues for all models (including those with no spectral filtering, Fig. 1.2). Therefore a valid solution for thermal convection in the lower mantle is possible even with 128 spherical harmonics degrees.

We find that filtering over a spectral domain is one of the possible solutions for controlling numerical instabilities in this study and it yields a spectrum which is free of aliasing (Fig. 1.2d). To justify our use of a filter, we calculated heat flux for the MI-F128 and MI-N128 simulations over a model-time interval of 3 Gyr until both simulations reached statistical steady-state. The MI-F128 simulation provides a surface heat flux of 37 TW while the corresponding value of heat flux for the no-filter simulation is 40 TW. The difference of ~ 3 TW is also found in the CMB flux, allowing us to conclude that filtering in the spectral domain does not affect the internal heating rate and thus the energy balance in the mantle.

It is worthwhile to explore the numerical stability of the convection model for a pair of the V2-simulations without a spectral filter and with the horizontal resolution defined by L=256. Both systems of this pair are constructed as in the case of the initial model (MI), but with a new geotherm that is taken from the MI-F simulation at 6.85 Ga. The first V2-simulation (MV2-N256) uses the original V2-profile, while the second one (MV2x10-N256) is calculated with a viscosity 10x stiffer than the MV2-N256 model. Integrating this pair of models over 250 Myr, we notice a few interesting features. For both simulations, the location of an numerical instability, initialized by the lack of horizontal resolution, is at the depth of 220 km (Fig. 1.3b) where the minimum viscosity in the V2-profile is located (see Fig. 1.1). The stiff viscosity above 220 km depth, in the MV2x10-N256 simulation, prevents 'noise' transport through the lower lithosphere (Fig. 1.3a). The MV2-N256 does not possess this ability and the aliasing will spread through the lithosphere. Again it is confirmed that we may be obliged to use an upper-mantle resolution corresponding to L=512 for modelling Earth like convective flows.

For now, our numerical scheme does not have the ability to discretise layers of the mantle separately, as suggested by these results, and we employ a single whole-mantle parametrisation. Although, in future studies, we may be obliged to use $L \geq 512$ for modelling Earth-like convective flows (at least in the upper mantle), in this study we first wish to validate the numerical model and then to determine a first estimate of the steady-state geotherm. Such simulations demand integration of more than 100,000 time steps and we therefore judge that the filtered horizontal spectrum defined by 256 spherical harmonic modes could deliver a geotherm that satisfies the energy balance.

It is worth pointing out that if aliasing in the (horizontal) spectral domain is not properly controlled, energy will be projected from the shortest to the longest wavelengths and thereby corrupt the solutions over the vertical (radial) domain (Fig. 1.4a). The presence of noise in the vertical spectrum can be indicated by measuring the total local root-mean square (rms) error of the predictor-corrector (p-c) solutions by the formula

$$err = \sqrt{\sum_{i=1}^{N}\sum_{\ell=0}^{L} \frac{D_{i\ell}^{0}\overline{D}_{i\ell}^{\,0} + 2\sum_{m=1}^{\ell} D_{i\ell}^{m}\overline{D}_{i\ell}^{\,m}}{C_{i\ell}^{0}\overline{C}_{i\ell}^{\,0} + 2\sum_{m=1}^{\ell} C_{i\ell}^{m}\overline{C}_{i\ell}^{\,m}}} \tag{1.46}$$

where N is the number of Chebyshev polynomials, L is the maximum spherical harmonic degree, and D is the difference between predictor P and corrector C solutions, while $\overline{D}$ and $\overline{C}$ represent their complex conjugates. From Fig. 1.4b we observe that numerical 'noise-transport' has a transient character due to the appearance of strong advection term in thermal convection. As we already illustrated (Fig. 1.2), the application of a spectral filter acting over the range of harmonic degrees of the non-linear term may be one method for controlling numerical instabilities (Fig. 1.4b).

1.6.2 Steady-state geotherm and energy balance

To determine a first estimate of the present-day geotherm satisfying bulk-energy balance we will employ L=256 for the horizontal resolution, using a Lanczos filter (see Appendix eq. (1.76)) in the spectral domain, and an initial geotherm for a new set of simulations (M2-HP and M2-HR) that will be taken from the MI-F simulation at 6.85 Ga.

One of the criteria we employ to validate our numerical convection scheme is to examine the model's ability to reach and then preserve the bulk-energy balance in the mantle. We will use a 5% deviation from perfect energy balance as an 'error' threshold to evaluate the numerical robustness of the calculated internal heating (as determined from the difference between surface and bottom heat flux).

In the first 750 Myr of the M2-HR simulation (see Fig. 1.5), fluctuations of internal heating are large, entering a couple of times inside the 5%-level, and each time over a wider time interval while in the remaining 1.25 Gyr the results may be called numerically robust (as defined

above). However, a standard-deviation analysis of two equal halves of the $[750, 2000]$ Ma interval reveals that geotherm variations from 750 Ma to 1375 Ma are still evident, especially in the bottom boundary layer (see Table 1.2). Thus, we defined new 5%-level interval, from 1375 Ma to 2 Ga (Fig. 1.6), where the mean heat flux at the top of the mantle is 37.24 ± 0.04 TW, and the amount at the CMB is 13.38 ± 0.05 TW. We note that the standard deviations continue to decrease during the time integration for heat flux at both top and bottom boundaries, indicating that there is no need to continue the M2-HR simulation beyond the point of 2 Ga (Table 1.2). The absolute mean value of numerically-calculated secular cooling during the final 625 Myr interval (Fig. 1.7) is 0.88 ± 0.07 TW, representing the range of uncertainty in the steady-state M2-HR geotherm.

The M2-HP simulation produces larger fluctuations in the heat flow compared to M2-HR (Fig. 1.5), but this model still satisfies bulk-energy balance in the mantle over a 1.25 Gyr interval. Using the same numerical-robustness analysis presented above, we obtained the following results for the M2-HP (with surface plates): (1) the mean values of heat flux are 43.58 ± 0.41 TW and 19.67 ± 0.38 TW for the surface and CMB flux, respectively (see Fig. 1.6) , and (2) the estimated 'error' in the steady-state M2-HP geotherm is 2.60 ± 0.50 TW over the $[2775, 3400]$ Ma 5%-level interval (see Fig. 1.7). Here, we selected the second half of the 1.25 Gyr interval to present numerically acceptable results of the M2-HP simulation (in the sense that the numerical secular cooling is minimal in this time interval, see Table 1.2).

Heat flow at the top and bottom of the mantle are controlled by the thermal boundary layers (Figs 1.8a and 1.8b). The thickness of the upper boundary layer, δ_s, for the M2-HR model is $\sim$ 124 km while its lower boundary layer, δ_c, is $\sim$ 87 km in thickness. Model M2-HP (with surface plates) has thinner boundary layers: $\delta_s \approx 105$ km and $\delta_c \approx 70$ km.

The bulk of the mantle between the two boundary layers is characterized by an adiabatic temperature profile where advective heat transport by vertical motion dominates all other heat transfer mechanisms. The adiabatic part of the M2-HP geotherm ranges between $\sim$ 1732 K and $\sim$ 2484 K indicating the evolution towards cooler bulk temperatures than the model with the rigid surface whose adiabatic values increase from $\sim$ 1824 K at the top to $\sim$ 2648 K at the bottom of the mantle. Comparing the adiabatic portions of the geotherms in both simulations

with the range of values in a reference adiabatic geotherm, ranging from 1700 to 2584 K at the bottom of the mantle, estimated on the basis of mineral physics constraints that satisfy a phase-change temperature of 1800 K at 400 km depth (Boehler & Chopelas (1991)), we may say that the upper-mantle adiabat in the M2-HP geotherm is more 'Earth-like' than the same part of the M2-HR geotherm (2% versus 7% of relative deviation), while the inverse is true for the lower-mantle adiabatic parts of both geotherms (4% versus 2%).

Thus, any geotherm taken from the model time interval $[1.375, 2]$ Ga would provide a useful starting point for the M2-HR class of model simulations, and similarly for the M2-HP models, where the acceptable 5%-level interval is from 2.775 to 3.4 Ga (Fig. 1.8c).

Time-dependent oscillations in heat flux (Fig. 1.6), and the corresponding variations in mantle bulk temperature (Fig. 1.7), are most strongly expressed in the M2-HP (surface-plate-coupled) simulation, owing to the larger instabilities originating in the surface boundary layer that are transmitted to the CMB via the subducting cold material. These oscillations are not characterised by any clearly defined periodicity, although fluctuations over time intervals of about 200 to 500 Myr are evident. Such time scales are thought to characterise the Wilson or super-continent 'cycle', but the assumed periodicity for this so-called cycle is uncertain, ranging from 200 Myr (e.g., Courtillot & Olson (2007)) to 400 Myr (Labrosse et al. (2008)). Indeed, recent analyses of global zircon data do not provide compelling evidence for a clear periodicity (e.g., Bradley (2011)), while other compilations suggest that any episodicity may be characterised by longer periods approaching 600 Myr (e.g., Voice et al. (2011)). There are corresponding uncertainties in interpreting the surface geodynamic manifestations of this cycle, for example, in terms of surface heat flux, with as much as 30% variation proposed by Labrosse & Jaupart (2007) and as little as 5% proposed by Korenaga (2007). The corresponding fluctuations of heat flux at the CMB (as in Fig. 1.6b) have been linked to mantle plumes that trigger massive surface volcanism and also magnetic superchrons (Courtillot & Olson (2007)). As noted by Courtillot & Olson (2007), even small fluctuations in CMB heat flux, near a critical threshold value, can lead to changes in magnetic reversal frequency. Perhaps the most relevant result is the hemispherical style of convection that ultimately develops in the M2-HP model (discussed below), a pattern that has been identified as intrinsic to the cycle of super-continent formation

and dispersal, as modelled for example by Yoshida & Santosh (2011) and Zhong et al. (2007).

1.6.3 Lateral heterogeneity and flow patterns

In the first 65 Myr, both model simulations maintain the initial amplitude of the dominant convection modes in the range, $\ell \in [1, 16]$ (Fig. 1.9a). The strong subduction zones, reinforced in the first 30 Myr, and the plumes of the M2-HP simulation extend across the mantle to the opposite thermal boundary layer (TBL) after 65 Myr and the consequent mixing of this transported thermal heterogeneity inside the boundary layers has commenced (Fig. 1.9a). In the M2-HP simulation, a strong ℓ=1 mode is established inside the adiabatic part of the mantle between 110 and 525 Myr (Figs 1.9b and 1.9c) and the evolution of the temperature structure in the TBL is completed at about 820 Myr (Fig. 1.9d). At this time, the predominance of amplitudes associated with ℓ=1 spans the entire mantle and remains stable through the interval of steady-state conditions (Figs 1.9e and 1.9f). The dominance of degree-1 convection in terrestrial mantles has been revealed in past explorations of so-called 'stagnant-lid' convection (Roberts & Zhong (2006)) and convection with strong lateral viscosity variations (Yoshida (2008)).

The primary characteristic of the M2-HP simulation is the intense reinforcement, in the starting tomography model, of subducted material that enters the mantle under the Indonesian and Western Pacific trench systems. Starting with the tomography-derived thermal structure ensures that this initial trajectory is strongly imprinted on the future evolution, since the present-day flow field is marked by strongest subduction, globally speaking, in this region. The time-dependent evolution of this subduction ultimately leads, over the billion-year interval examined here, into a dominant hemispherical configuration of temperature anomalies in the mantle. This evolution is, of course, affected by the time-invariant surface plate geometry employed in this simulation. It is important to recall however, especially from the perspective of dynamical and energetic self-consistency, that the surface plate motions are not forced with imposed (prescribed) velocities in the plate-coupled flow calculations. This differs from previous approaches involving a prescribed history of surface plate velocities (e.g., Zhang et al. (2010)). Although the geologically inferred dominance of subduction along the margins of the paleo-Pacific (e.g., Zhang et al. (2010)) may suggest that this hemispherical pattern of subduction is not unreasonable,

we do not suggest that a fixed billion-year pattern of surface subduction is tenable. We instead choose to run these simulations to steady state to quantify the mean (ℓ=0) thermal structure (i.e. geotherm and heat flow) in the mantle. The time-dependent evolution of lateral heterogeneity over the first 100 to 200 Myr is of primary interest in exploring the interaction of subducting material with the very large radial increases of mantle viscosity as well as the amplification and propagation of the upwelling plumes from the lowermost mantle (discussed below).

In contrast to convection with moving surface plates, the M2-HR (rigid-surface) simulation does not generate 'giant' subduction zones and the downward sinking mantle originating in the cold, upper TBL is characterized by relatively weak-amplitude thermal anomalies. The changing structure of the upper TBL, due to the impact of ascending thermal plumes, continues to evolve until 525 Ma (Fig. 1.9c) and beyond this point the dominant modes of convection are characterized by harmonic degrees ℓ=3 and 4 (Figs 1.9d, 1.9e and 1.9f).

The M2-HR (rigid-surface) simulation reveals the remarkable stability and very-long-term longevity of mantle plumes that originate in the starting 3-D tomographic image of hot-mantle anomalies inside the D"-layer (Fig. 1.10a).

The steady-state plumes appear at the depth of 220 km during first 200 Myr (Fig. 1.10b). We note that four of five plumes that remain stable up to 2 Ga (Fig. 1.10f) may be linked with the locations of the present day hotspots (Courtillot et al. (2003)). The first cluster of hotspots is located around the edges of a plume that originated under East Pacific Rise (see Table 1.3). The origin of the second plume is between Fernando and Cape Verde hot spots associated with the South-American and African plates respectively, i.e. located at the mid-Atlantic ridge. The Crozet hotspot related to the Antarctica plate is relatively close to the centre of the third plume (44°S 56°E) that also could be the source of Kerguelen, Marion and Reunion hotspots. We also note the isolated Caroline hotspot that could be connected to the Darwin Rise - a large region of anomalously shallow bathymetry in the western Pacific (Cadio et al. (2011)). The location of a fifth plume under the European part of North-West Russia cannot be related with any present-day hotspot. Although the origin of this 'Siberian' plume (Smirnov & Tarduno (2010)) is beyond the scope of this paper, the ability of the convection model to 'capture' and reinforce this plume in the diffuse lower-mantle signal present in the starting tomography model is intriguing.

From Figs 1.10c, 1.10d, and 1.10e, we observe that other major hotspots have transient appearance, while some of them are not detectable by the M2-HR model (see Table 1.4). Also, it seems that during one period of time around 200 Ma (Fig. 1.10b) Iceland hotspot is part of the super plume which is subsequently re-organized into the 'Siberian' plume.

In contrast to the M2-HR model, the M2-HP (plates) convection simulations cannot yield stable and very-long-term longevity mantle plumes (Fig. 1.11). However, the M2-HP model is able to track the evolution of Marqueses, Louisville, Hawaii, Galapagos, and Martin hotspots that are undetectable by the M2-HR (see Table 1.4). The detection of the hotspot-related plumes is only possible up to 820 Ma because after that, the pattern of steady-state convection for the M2-HP model is dominated by the degree-1 (see Fig. 1.9).

The M2-HP (plates) simulation shows more fluctuations in the lateral variations of temperature (Fig. 1.12a) that precede by a couple of tens of Myr the geotherm perturbation (Fig. 1.12b). The fluctuations are also of larger amplitude (Fig. 1.13) because of the effects of changing subduction of cold material at the surface that have an ability to transport perturbations deep into the lower mantle and reaching the CMB (see Fig. 1.9). In contrast, the M2-HR simulation is dominated by the dynamics of ascending hot plumes and these are much more steady than subducting material. However, the variations in mantle thermal anomalies that provide the buoyancy changes reflected in the kinetic energy precede by a couple of hundreds of Myr the geotherm perturbations seen in the heat flux difference (Figs 1.12c and 1.12d).

Although the M2-HP or the M2-HR simulations are not expected to be representative of the actual evolution of Earth's mantle into the distant future, we conjecture that the convective trajectory of the 'real' Earth may lie between these two end-member cases. From a purely fluid-mechanical perspective of instantaneous (present-day) flow, the surface boundary on a planet with a limited number of tectonic plates is not far from a no-slip surface (e.g., Ricard & Vigny (1989); Forte & Peltier (1994)). This result follows from the very limited number of surface degrees of freedom (3 x N), for N plates, relative to the effectively infinite number of degrees of freedom (e.g., the harmonic coefficients of the mantle flow field) for the underlying convective flow. So for this reason, the evolution of the M2-HP and M2-HR simulations is similar in the first few millions of years. Obviously over billion-year time scales, the differences accumulate

and the two simulations ultimately diverge. We note however, from a comparison of Figs 1.10 and 1.11 for M2-HR and M2-HP, that the stability and evolution of the main hot upwellings in the mantle is similar over the first ~ 200 Myr. These results suggest to us that the present-day tomography models resolve plume structures that may be remarkably stable and long-lived over time scale scales of (at least) several hundred Myr. It is notable that this stability does not require the assumption of thermochemical piles in the lower-mantle (e.g., McNamara & Zhong (2005)), but rather arises from the stabilising influence of the geodynamically constrained lower-mantle viscosity structure we employ (e.g., Forte & Mitrovica (2001)).

1.7 Discussion

We have developed a pseudo-spectral numerical model of compressible, gravitationally consistent, thermal convection in a spherical-shell planetary mantle that is capable of delivering accurate and robust solutions over very long geological time scales (involving several hundred thousand numerical time steps). For Earth-like Rayleigh numbers, we find that a fully resolved solution of thermal convection dynamics in the upper mantle may require a horizontal expansion of the field variables up to spherical harmonic degree 512 (corresponding to a horizontal resolution scale of less than half a degree on the sphere). In contrast, for a fully resolved description of convection dynamics in the lower mantle, we find that a spherical harmonic truncation level at degree 128 is entirely sufficient. These differences in depth-dependent numerical resolution are consequences of the radial viscosity profile of the mantle that is constrained by surface geodynamic data, in which the average viscosity of the lower mantle is nearly two orders of magnitude greater than average upper-mantle viscosity.

To reconcile the contrasting horizontal resolution requirements in the upper and lower mantle we have adopted a globally uniform spectral description characterized by a spherical harmonic truncation at degree 256. To control any possible numerical instabilities in the upper mantle due to aliasing in the spectral domain we employed a Lanczos filtering of the spherical harmonic expansion of the non-linear temperature advection term. We found that the application of this spectral filtering throughout the mantle did not bias the essential global energy balance, a criterion we systematically applied to verify the numerical accuracy of our solutions. More

specifically, our numerical validation of the mantle convection solutions reveals that we can achieve and preserve a steady-state global energy balance (to within 5%) over very long geological time intervals (beyond 2 Gyr or 50,000 time steps) for both plate-like and rigid surface boundary conditions.

We obtained a valid approximation of steady-state geotherms for both surface boundary conditions (tectonic plates, rigid surface). In both cases we obtain surface heat flux values in the range of Earth-like values: 37 TW for a rigid surface and 44 TW for a surface with tectonic plates coupled to the mantle flow. Past estimates of CMB heat flux have been based on a number of different methods (see Jaupart et al. (2007) and Mareschal et al. (2012)) with values ranging widely between 4 and 14 TW. Currently, the highest estimates of CMB heat flux have been derived from models of the post-perovskite phase transition at the base of the mantle, with values of at least 13 ± 4 TW (e.g., Lay et al. (2006)). We find, therefore, that although our convection simulations deliver relatively high CMB heat flux, namely 13 TW and 20 TW, for rigid and plate-like surface boundary conditions, respectively, these values are compatible with the independent higher estimates cited above. We further note that the relatively high values of CMB heat flux predicted by our convection models are obtained assuming a CMB temperature of 3300 K. If we employ higher CMB temperatures, for example 4000 K (Boehler (1996)), then our predicted CMB heat flux becomes much larger than even the current highest independent estimates. The CMB temperature is therefore an important controlling parameter and this issue is discussed further below.

We have also found, for a rigid-surface boundary, that the dominant modes of steady-state convection that persist over very long time scales correspond to harmonic degrees 3 and 4. It is interesting that these same modes were also identified as dominant by Chandrasekhar (1961) on the basis of his solutions of the marginal stability problem for convection in spherical shells. The dominant convection modes for the rigid-surface simulations are able to reinforce and maintain the stability of some of the present-day hotspot-related plumes in the mantle and this stability extends over remarkably long geological time spans (of order 1 to 2 Gyr).

The plate-like surface boundary condition, in which the tectonic plate motions are coupled to those inside the mantle, is also able to produce some of the hotspots but these hotspot-

related plumes are transient in character, persisting over the first few hundred million years (see Fig. 1.11), but then continue to change in pattern after about five hundred million years as the model evolves further to long-term steady state.

The plate-like surface boundary condition yields a dominant mode of steady-state convection characterized by the long-term stability of two hemispherical structures, one hot and another cold where the latter contains giant descending limbs of cold subducted material that extends down to the CMB. We note, however, that prior to steady-state, the M2-HP simulation shows a temporal evolution through several distinct regimes. During the initial period, over the first 110 Myr, the slab and plume structures in the starting tomography model are reinforced due to the build-up of heterogeneity in the top and bottom TBLs. Between 110 and 525 Ma a strong ℓ=1 mode is established within the adiabatic interior of the mantle, outside the TBLs, and in the next 300 Myr, a clustering of subduction and upwelling occurs, thereby forming two opposing thermal hemispheres.

The dominance of such a degree-1 pattern of convection has been found in previous studies that included moderately-strong lateral viscosity variations (Yoshida (2008)). Our current implementation of the pseudo-spectral method does not explicitly model the effect of lateral variations in viscosity (LVV). The impact of such LVV has been previously explored in a number of studies of instantaneous mantle flow, for cases in which the LVV are focussed in the lithosphere or alternatively in the lower mantle (e.g., Čadek & Fleitout (2003); Čadek & Fleitout (2006); Tosi et al. (2009)) and in cases where they are distributed throughout the mantle (e.g., Forte & Peltier (1994), Moucha et al. (2007)) showed the amplitude of the dynamical effect of the LVV on surface observables is of the order of that due to differences (i.e. uncertainties) among the different seismic tomography models.

While surface observables appear to be relatively insensitive to LVV, the internal buoyancy-driven flow may be significantly affected, such that hot upwelling plumes may be more strongly focussed, with amplified flow velocities inside the main upwellings. This LVV-enhancement of mantle plumes is based on the standard assumption that thermally activated creep is the only dominant mechanism that is relevant in the mantle. If so, the LVV will also have an effect at the bottom of the mantle, such that the D"-layer will be more unstable and generate plumes with

greater frequency. The outstanding issue is then how to incorporate a representation of LVV in convection models that is at the same time compatible with mineral physics and with surface geodynamic constraints on mantle rheology. Current efforts to include LVV in time-dependent convection models (e.g., Nakagawa & Tackley (2008b); Zhang et al. (2010)) are based on simplified representations of both the depth (pressure) and temperature dependence of viscosity. None of these parametrized LVV models have been shown to generate a satisfactory fit to the range of geodynamic surface observables that have been considered in past 1-D inversions of these surface data (e.g., Mitrovica & Forte (2004)). These difficulties are further exacerbated by the recognition that temperature (and pressure) is not the only contributor to LVV, and that chemical effects (e.g., hydration state), variations in grain size (e.g., Solomatov & Reese (2006)) and variations in deformation mechanisms (e.g., Cordier et al. (2012)) can have equally important (and possibly stronger) effects. In other words, there is a great deal of uncertainty regarding the appropriate representation of LVV in mantle convection models. Confronted by these major uncertainties, we have opted to work with depth-dependent viscosity profiles that have been directly verified against a wide suite of geodynamic surface constraints (Mitrovica & Forte (2004); Forte et al. (2010)) and independent mineral-physical modelling (Ammann et al. (2010)). In the present study, we regard the incorporation of rigid, but mobile (free-rotating) surface plates overlying a very-low viscosity asthenosphere in model M2-HP as effectively equivalent to extreme LVV at the top of the mantle.

One major simplification in the convection model with surface plates (M2-HP), is the assumption that plates retain their present-day configuration over very long (billion-year) time spans. We know from geological reconstructions that plate geometries have constantly evolved over the past 200 million years (e.g., Müller et al. (2008)), although the large-scale pattern of long-term circum-Pacific subduction seems rather stable. There is, on the other hand, no currently accepted theory for accurately predicting the future evolution of surface plate geometries over very long geological time spans, in a manner that is dynamically self-consistent with the underlying mantle flow. It is this difficulty that also led us to explore long-time convection simulations with a simple rigid surface (an 'one-plate' model), to avoid the possible geometric and dynamical bias of assuming fixed surface locations for subducting cold material in the mantle.

The existence of substantial hemispheric-scale cold material descending to the CMB, and its enhanced cooling of the mantle, appears to be the main explanation for higher surface heat flux (by 6-7 TW) compared to the rigid-surface (M2-HR) convection solution where the primary mode of heat transport across the lower mantle is via the hot and stable upwelling plumes producing a heat flux in the range of acceptable values.

Although it is therefore clear that our convection modelling is an undoubtedly simplified representation of the complex nature of the dynamics in Earth's mantle, it is useful to recall the importance of some of the novel aspects of our numerical simulations.

First, we used a 'realistic' viscosity profile (V2), determined in previous inversions (Mitrovica & Forte (2004); Forte et al. (2010)) of geodynamic data sets that constrain the rheology of the mantle, which is characterized by radial changes in η over 3 orders of magnitude. Some previous mantle convection studies in spherical geometry (e.g., Schuberth et al. (2009b)) have used simplified (2- or 3-layer) radial viscosity structures, not directly derived from geodynamic constraints, and the resulting heat-flux predictions differ from those presented above, even though other input parameters are similar. There are outstanding uncertainties in the geodynamically-inferred mantle viscosity, particularly in the lowermost mantle (e.g., in the D"-layer) where the constraints are weakest (Forte (2007)). For example, Steinberger & Calderwood (2006) calculated instantaneous mantle flow, assuming the thickness of D" to be 200 km, and obtained a viscosity profile constrained by mineral physics (melting temperatures) and surface observations. This viscosity profile is characterised by strong increase with depth in the lower mantle, up to about 1×10^{23} Pa.s above the D" layer, and more than 100x viscosity reduction within the lowermost 200 km (D" layer). Comparing with the V2-profile, the viscosity obtained by Steinberger & Calderwood (2006) is less than 10x stiffer inside the D" layer thereby yielding a thicker lower thermal boundary layer, and thus lower CMB flux than we simulated here. Obviously, the assumed mantle viscosity structure has a critical impact on the spatial (and temporal) evolution of mantle temperature variations, especially since each viscosity profile is characterized by local, depth-dependent Ra_H that vary over several orders of magnitude.

Second, we employ a thermal conductivity that varies with depth according to recent mineral physical calculations (Hofmeister (1999)) and takes into account the thermal structure of the

boundary layers at the top and bottom of the mantle. The assumed depth-dependence of thermal conductivity is of major importance inside the thermal boundary layers, because heat transfer by conduction is either dominant or roughly equal to heat transfer by advection. A widely assumed choice for thermal conductivity in previous mantle convection models is the use of a constant value (typically, $k = 3\mathrm{Wm}^{-1}\mathrm{K}^{-1}$). The assumption of such a constant value of conductivity is within the range of Hofmeister (1999) k-profile for the oceanic lithosphere, but about 2× lower for the D"-layer and thereby explains previous predictions of lower CMB heat flux (e.g., Schuberth et al. (2009b)) than is estimated in our study.

An outstanding question in current mantle convection modelling is the appropriate value for the temperature at the CMB, which depends on knowledge of the adiabatic temperature profile in the outer core. Improved mineral-physical constraints on the CMB temperature, and hence the temperature jump across the D"-layer, can therefore provide independent information on the heat flux at the CMB. In previous mineral-physical modelling by Boehler (1996) it was estimated that the temperature jump across the CMB is 1400 K, constrained by a minimum temperature on the core side of the CMB of 4000±200 K and a mantle temperature at the CMB of about 2600 K. This estimate of CMB temperature is obtained using the adiabatic temperature drop across the liquid core of 850 K, pinned to an estimated temperature at the inner-core boundary (ICB) of about 5000 K, estimated from iron melting data (Boehler (1996)).

We note that the CMB temperature of 3300 K employed in our mantle convection simulations, although lower than the earlier estimates from laboratory and mineral-physical data (e.g., Boehler (1996)), was necessary to obtain acceptable value of surface heat flow and to avoid excessively large CMB heat flux and mean mantle temperatures. It is therefore of some interest that recent laboratory data on the melting of iron at core conditions, in the presence of other light elements (e.g., S and O) now suggest that the outer-core adiabat may be substantially cooler than previously estimated, and that our assumed CMB temperature may be plausible, if still on the lower end of the currently estimated range (Terasaki et al. (2011); Huang et al. (2011)). Closely related to the question of CMB temperature, and the energy budget of the mantle, is the rate of secular cooling and, in particular, the radial distribution of internal heating. These outstanding questions provide motivation for a new set of simulations that will be tested in future studies

employing the robust and efficient numerical convection methods presented in this work.

In summary, there are two basic findings which emerge from the very long-time scale, tomography-based convection simulations presented above. The first concerns the extent to which a 'memory' of the pattern of mantle heterogeneity in the starting tomography model is preserved over time. We find that with both the M2-HP and M2-HR convection simulations, there is a remarkable persistence of the hot, plume-like structures originating in the deep lower mantle. Indeed, there is no a-priori reason to anticipate that the plumes resolved in the starting tomography model should be maintained over very long times, especially in the high-Rayleigh number regime that characterises our convection models. Moreover, these simulations do not include dense chemical 'piles' at the base of the mantle that have been assumed necessary for stationary plumes (e.g., Tan et al. (2011)). The geographic stability of the deep-mantle plumes is found to extend over the first few hundred Myrs in the M2-HP (plate-coupled) model and for even longer in the M2-HR (rigid-surface) model. This plume stability and longevity is dependent on the important rheological stabilisation (e.g., Lowman et al. (2004); Lowman et al. (2008); Quéré & Forte (2006)) associated with the very-high lower-mantle viscosity peak inferred from geodynamic constraints (Forte & Mitrovica (2001); Mitrovica & Forte (2004)). As shown in Figs 1.10 and 1.11 , the most stable and long-lived deep-mantle plumes show an intriguing spatial relationship to the surface constellation of hotspots and other manifestations of intra-plate volcanism (e.g., Siberian traps). The second result to emerge from our exploration of very long-time scale convection is the high heat flux that obtains at the CMB, thereby providing the thermal energy that maintains the vigour of the deep-mantle plumes. There is indeed a direct and necessary connection between high heat flux and the strength of the lower-mantle plumes (e.g., Schuberth et al. (2009b)). Finally, although some convection studies have argued that large-amplitude chemical heterogeneity in the lower mantle (e.g., Tan et al. (2011)) is needed to generate stable plume groups, our results suggest that the geodynamically constrained viscosity maximum in the lower mantle, in conjunction with high CMB heat flux, is very effective in maintaining long-lived stable plumes. Indeed our findings ultimately lend further support to previous studies demonstrating a dominantly thermal interpretation of heterogeneity in the tomography models (e.g., Forte & Mitrovica (2001); Quéré & Forte (2006); Simmons et al.

(2007); Simmons et al. (2009); Schuberth et al. (2009a); Schuberth et al. (2009b); Davies & Davies (2009)).

1.A Pseudo-Spectral Numerical Solution of the Energy Conservation Equation

This section describes the procedure employed to obtain the spherical harmonic coefficients of all terms involved in the equation of conservation of energy (1.42).

1.A.1 Diffusion operator

The diffusion term is calculated following the procedure employed by Glatzmaier (1984). By expressing the temperature in terms of its spherical harmonic coefficients and by calculating explicitly the gradients in spherical coordinates, we obtain:

$$(\nabla.k\nabla T)(r,\theta,\phi,t) = \nabla k.\nabla T + k\nabla.\nabla T = k(r)\sum_{\ell=0}^{L}\sum_{m=-\ell}^{+\ell} \left(\frac{\partial^2 T_\ell^m(r,t)}{\partial r^2} + \frac{1}{r^2 k}\frac{\partial r^2 k(r)}{\partial r}\frac{\partial T_\ell^m(r,t)}{\partial r} - \frac{\ell(\ell+1)}{r^2}T_\ell^m(r,t)\right) Y_\ell^m(\theta,\phi) \tag{1.47}$$

for which the following relation was used :

$$\nabla_{\mathrm{H}}.\nabla_{\mathrm{H}}Y_\ell^m(\theta,\phi) = -\frac{\ell(\ell+1)}{r^2}Y_\ell^m(\theta,\phi) \tag{1.48}$$

where ∇_{H} is the horizontal gradient. We note that relation (1.47) is valid when the thermal conductivity k depends only on r , as we assumed in section 1.5. The spherical harmonic coefficients in (1.47) depend on the radial derivatives of the temperature. These derivatives are readily calculated from a Chebyshev polynomial expansion of the radial dependence of the harmonic coefficients of the temperature, $T_\ell^m(r,t)$.

The evaluation of Chebyshev coefficients requires that the temperature is specified at depths

r_i corresponding to Chebyshev nodes x_i,

$$r_i = \frac{1}{2}(r_{\text{surf}} - r_{\text{cmb}})x_i + \frac{1}{2}(r_{\text{surf}} + r_{\text{cmb}})$$
$$\text{with} \quad x_i = \cos\left(\frac{i\pi}{N}\right) \text{ and } i = 0, \ldots, N\,. \tag{1.49}$$

At these depths, the Chebyshev polynomials are

$$C_n(x_i) = \cos\left(\frac{ni\pi}{N}\right).$$

The spherical harmonic coefficients of the temperature field are expressed in series of Chebyshev polynomials as

$$T_\ell^m(r,t) = \left(\frac{2}{N}\right)^{\frac{1}{2}} \sum_{n=0}^{N}{}'' \, T_{\ell n}^m(t)\, C_n(x) \tag{1.50}$$

where the double quotes mean that the first and last terms of the sum are multiplied by 1/2. A fast cosine transform (derived from the FFT) is used to obtain the coefficients $T_{\ell n}^m(t)$.

The radial derivative of the temperature becomes

$$\begin{aligned} \frac{\partial T_\ell^m(r,t)}{\partial r} &= \left(\frac{2}{N}\right)^{\frac{1}{2}} \sum_{n=0}^{N}{}'' \, T_{\ell n}^m(t)\, \frac{\partial C_n(x)}{\partial r} \\ &= \left(\frac{2}{N}\right)^{\frac{1}{2}} \sum_{n=0}^{N}{}'' \, T_{\ell n}^m(t)\, \frac{2}{r_{\text{surf}} - r_{\text{cmb}}} \frac{\partial C_n(x)}{\partial x}. \end{aligned} \tag{1.51}$$

Substituting relations (1.50) and (1.51) into equation (1.47), we obtain the expression of the spherical harmonic coefficients of the diffusive term:

$$(\nabla . k \nabla T)_\ell^m(r,t) = \tag{1.52}$$
$$\left(\frac{2}{N}\right)^{\frac{1}{2}} k(r) \sum_{n=0}^{N}{}'' \left(\frac{\partial^2 C_n(x)}{\partial r^2} + \frac{1}{r^2 k(r)} \frac{\partial r^2 k(r)}{\partial r} \frac{\partial C_n(x)}{\partial r} - \frac{\ell(\ell+1)}{r^2} C_n(x) \right) T_{\ell n}^m(t)$$

which is valid for all depths inside the mantle. Since k and C_n are known polynomial functions of depth, their derivative is also known.

The choice of Chebyshev polynomials is not fortuitous as they present two main advantages

(Glatzmaier (1984)). Firstly, Chebyshev functions provide the best polynomial interpolation due to their favourable convergence properties. Secondly, the Chebyshev grid is formed of non-equally spaced nodes with a greater number at both extremities of the interval. This characteristic results in a higher resolution in the boundary layers which is beneficial because the boundary layers are the main sources of convective instabilities.

1.A.2 Advection

The non-linearity of the advection term makes its spectral representation challenging. This term cannot be easily expressed in the spectral domain without having recourse to cumbersome spherical harmonic coupling coefficients (e.g., Forte & Peltier (1994)). It is more readily calculated in the spatial domain (r, θ, ϕ) where the temperature gradient, the velocity field and their scalar product may be easily determined. The latter is then transformed to the spectral domain of the spherical harmonics. The procedure we employ to compute the different quantities in the spatial domain, using generalized spherical harmonics (Phinney & Burridge (1973)), differs from the one described by Glatzmaier (1984).

The temperature gradient is computed via the following expression (Phinney & Burridge (1973)):

$$\begin{aligned}
\nabla^{-}T(r,\theta,\phi,t) &= \frac{1}{r}\sum_{\ell,m}^{L}\sqrt{\frac{\ell(\ell+1)}{2}}T_{\ell}^{m}(r,t)Y_{\ell}^{-1\,m}(\theta,\phi) \\
\nabla^{0}T(r,\theta,\phi,t) &= \sum_{\ell,m}^{L}\frac{\partial T_{\ell}^{m}(r,t)}{\partial r}Y_{\ell}^{0\,m}(\theta,\phi) \\
\nabla^{+}T(r,\theta,\phi,t) &= \frac{1}{r}\sum_{\ell,m}^{L}\sqrt{\frac{\ell(\ell+1)}{2}}T_{\ell}^{m}(r,t)Y_{\ell}^{+1\,m}(\theta,\phi)
\end{aligned} \tag{1.53}$$

where $\nabla^{-}T, \nabla^{0}T, \nabla^{+}T$ are the components of the temperature gradient in the complex spherical basis $(\mathbf{e}_{-}, \mathbf{e}_{0}, \mathbf{e}_{+})$ defined by eq. (1.27).

The summations over the index m in eq. (1.53) are computed via the use of FFT's. Since we already expressed the velocity field in the complex basis $(\mathbf{e}_{-}, \mathbf{e}_{0}, \mathbf{e}_{+})$ when solving the equations of conservation of mass and momentum (Forte (2007)), the computation of the scalar product between temperature gradient and flow velocity is straightforward. It is calculated at every time

step from the relation:

$$(\mathbf{u}\cdot\nabla T)\,(r,\theta,\phi,t) = u^0\nabla^0 T - u^+\nabla^- T - u^-\nabla^+ T\,. \tag{1.54}$$

Finally, the advective term is expanded in a series of (ordinary) spherical harmonics:

$$(\mathbf{u}\cdot\nabla T)\,(r,\theta,\phi,t) = \sum_{\ell=0}^{L}\sum_{m=-\ell}^{+\ell} (\mathbf{u}\cdot\nabla T)_\ell^m(r,t)\; Y_\ell^m(\theta,\phi)\,. \tag{1.55}$$

The coefficients $(\mathbf{u}\cdot\nabla T)_\ell^m$ are determined numerically by integration on a spatial geographic grid via the use of FFT's and Gauss-Legendre integration. They will be used for the solution of equations (1.42).

1.A.3 Dissipation and internal heating

The dissipative term related to compression work, whose expression is given by eq. (1.14), is first calculated in the physical space (r,θ,ϕ) by using $u_r = u^0$. It is then expanded numerically in terms of spherical harmonic coefficients. The method used to determine the coefficients of the viscous dissipation term Φ which expresses frictional heating, is similar to the one described for the advective term. It is first calculated in the physical space described by the basis $(\mathbf{e}_-, \mathbf{e}_0, \mathbf{e}_+)$ using a procedure very similar to the calculation of the elastic potential in Phinney & Burridge (1973). The expression (1.6) for the viscous dissipation may be rewritten using the viscous constitutive relation (1.5) as follows:

$$\Phi = \frac{1}{2\eta}\tau_{ij}\tau_{ij}\,. \tag{1.56}$$

Rotating the tensor τ_{ij} from (e_r, e_θ, e_ϕ) space to that spanned by the complex basis $(\mathbf{e}_-, \mathbf{e}_0, \mathbf{e}_+)$ we obtain

$$\Phi = \frac{1}{2\eta} e_{\alpha\gamma}\, e_{\beta\delta}\, \tau^{\alpha\beta}\, \tau^{\gamma\delta} \tag{1.57}$$

where the $e_{\alpha\gamma}$ and $e_{\beta\delta}$ are covariant representations of the identity tensor δ_{ij} in the complex space (Phinney & Burridge (1973)). From this last expression we finally obtain

$$\Phi = \frac{1}{2\eta}\left[(\tau^{00})^2 + 2\,\tau^{++}\tau^{--} + 2\,(\tau^{+-})^2 - 4\,\tau^{0-}\tau^{0+}\right] . \tag{1.58}$$

The tensor components $\tau^{\alpha\beta}$ in the above expression are expanded in generalized spherical harmonics as in (1.29). The value of these tensor components, in the spatial domain is used to determine

$$\Phi(r,\theta,\phi,t) = \sum_{\ell=0}^{L}\sum_{m=-\ell}^{+\ell} \Phi_\ell^m(r,t)\, Y_\ell^m(\theta,\phi) \tag{1.59}$$

where the coefficients $\Phi_\ell^m(r,t)$ are determined via the use of FFT's and Gauss-Legendre integration.

The last term of equation (1.42) is the internal heating. It is assumed to be laterally homogeneous (although possibly depth dependent), thus Q_0^0 is the only non-zero coefficient:

$$Q_\ell^m = 0 \;\; \forall \ell, m \neq 0 . \tag{1.60}$$

1.A.4 Solution of the equation of energy conservation

1.A.4.1 Numerical scheme

This section describes the numerical scheme employed to advance the solution of the equation of energy conservation (eq. 1.42) in time. The procedure is similar to the one employed by Glatzmaier (1984), except that we use the complete predictor-corrector numerical scheme for the time stepping of the non-linear terms. To simplify the writing of the equations, new variables are defined. Using equation 1.52, the diffusivity term is written as

$$(\nabla.k\nabla T)_{\ell i}^m(t) = D_{\ell i n}^m\, T_{\ell n}^m(t) \tag{1.61}$$

where

$$D_{\ell i n}^m = \left(\frac{2}{N}\right)^{\frac{1}{2}} k_i \left(\frac{\partial^2 C_{in}}{\partial r^2} + \frac{1}{r^2 k_i}\frac{\partial r_i^2 k_i}{\partial r}\frac{\partial C_{in}}{\partial r} - \frac{\ell(\ell+1)}{r_i^2} C_{in}\right) \tag{1.62}$$

and the non-linear terms are gathered together such that

$$b_{\ell i}^{m}(t) \;=\; -\rho c_p(\mathbf{u}.\nabla T)_{\ell i}^{m} + (\alpha T\frac{dp}{dt})_{\ell i}^{m} + \Phi_{\ell i}^{m}\,. \tag{1.63}$$

In equation (1.61) the summation over the index n is implicit. The index i denotes the value at depth r_i of the variable considered; for example, $k(r_i) = k_i$. In the particular case of the Chebyshev polynomials, we use the notation $\mathcal{C}_{in} = \mathcal{C}_n(x_i)$.

If we assume that time-integration interval is discretised, $j = 0, ..., M$, and the solution is known at time t_j and t_{j-1}, then the numerical scheme employed to compute the solution at time t_{j+1} is described by the following equations:

- Predictor (non-linear terms) + modified Crank-Nicholson scheme (diffusion)

$$\begin{aligned} T_{\ell i}^{m\,*} - \frac{9\Delta t_j}{16} D_{\ell in}^{m}\, T_{\ell n}^{m\,*} \;&=\; T_{\ell i}^{m}(t_j) \\ &+\; \frac{3\Delta t_j}{8} D_{\ell in}^{m}\, T_{\ell n}^{m}(t_j) + \frac{\Delta t_j}{16} D_{\ell in}^{m}\, T_{\ell n}^{m}(t_{j-1}) \\ &+\; \Delta t_j \left((1 + \frac{\Delta t_j}{2\Delta t_{j-1}})\, b_{\ell i}^{m}(t_j) - \frac{\Delta t_j}{2\Delta t_{j-1}}\, b_{\ell i}^{m}(t_{j-1}) \right) \\ &+\; \Delta t_j\, Q\, \delta_{\ell 0}\delta_{m0}\,. \end{aligned} \tag{1.64}$$

- Corrector (non-linear terms) + modified Crank-Nicholson scheme (diffusion)

$$\begin{aligned} T_{\ell i}^{m}(t_{j+1}) - \frac{9\Delta t_j}{16} D_{\ell in}^{m}\, T_{\ell n}^{m}(t_{j+1}) \;&=\; T_{\ell i}^{m}(t_j) + \frac{3\Delta t_j}{8} D_{\ell in}^{m}\, T_{\ell n}^{m}(t_j) \\ &+\; \frac{\Delta t_j}{16} D_{\ell in}^{m}\, T_{\ell n}^{m}(t_{j-1}) \\ &+\; \Delta t_j \left(\frac{1}{2}\, b_{\ell i}^{m\,*} + \frac{1}{2}\, b_{\ell i}^{m}(t_j) \right) \\ &+\; \Delta t_j\, Q\, \delta_{\ell 0}\delta_{m0}\,. \end{aligned} \tag{1.65}$$

Δt_{j-1} and Δt_j are two successive time steps; the time step varies according to the Courant stability criterion described by equation (1.74) below. T^* represents the predicted temperature

at time t_{j+1} and before correction, b^* is the corresponding predicted non-linear term.

The above procedure cannot be employed for the first iteration because it requires the solutions at two successive time steps. Therefore, the following SBDF (semi-implicit backward differentiation formula) scheme is employed for the predictor-corrector method for the first iteration:

- Predictor scheme

$$\begin{aligned} T_{\ell i}^{m*} - \Delta t_j D_{\ell i n}^m T_{\ell n}^{m*} &= T_{\ell i}^m(t_j) + \Delta t_j b_{\ell i}^m(t_j) \\ &+ \Delta t_j\, Q\, \delta_{\ell 0}\delta_{m0}\,. \end{aligned} \tag{1.66}$$

- Corrector scheme

$$\begin{aligned} T_{\ell i}^m(t_{j+1}) - \Delta t_j D_{\ell i n}^m T_{\ell n}^m(t_{j+1}) &= T_{\ell i}^m(t_j) \\ &+ \Delta t_j \left(\frac{1}{2} b_{\ell i}^{m*} + \frac{1}{2} b_{\ell i}^m(t_j)\right) \\ &+ \Delta t_j\, Q\, \delta_{\ell 0}\delta_{m0}\,. \end{aligned} \tag{1.67}$$

1.A.4.2 Thermal boundary conditions

The previous equations (1.64) to (1.67) are used at each depth r_i, $i = 1, \ldots, N-1$, (N+1) being the number of Chebyshev points. At the surface r_0 and at the core-mantle boundary r_N, boundary conditions are required. There are two types of boundary conditions which can be used, either isothermal boundary or constant heat flux. Isothermal boundaries seem to be more realistic for both the Earth's surface and the core-mantle boundary, and yet several authors (e.g., Solheim (1986); Jarvis (1991)) have opted to apply a constant heat flux condition to model the CMB. This allows one to control the ratio of flux coming from the core to the one induced by internal (radioactive) heating. In this study we have employed isothermal conditions for both the surface and the CMB.

At the surface,

$$T_0^0(r_0) = \left(\frac{2}{N}\right)^{\frac{1}{2}} \sum_{n=0}^{N}{}'' T_{0n}^0\, C_n(x_0) = T_{\text{surf}} \tag{1.68}$$

since $C_n(x_0) = 1$, we are left with

$$\left(\frac{2}{N}\right)^{\frac{1}{2}} \sum_{n=0}^{N}{}'' T_{0n}^{0} = T_{\text{surf}} \,. \tag{1.69}$$

The other harmonics vanish as there are no lateral variations of temperature, hence

$$\sum_{n=0}^{N} T_{\ell n}^{m} = 0 \quad \forall \ell, m \neq 0 \,. \tag{1.70}$$

Similarly, at the core-mantle boundary, we have

$$\left(\frac{2}{N}\right)^{\frac{1}{2}} \sum_{n=0}^{N}{}'' (-1)^n T_{0n}^{0} = T_{\text{cmb}} \tag{1.71}$$

and

$$\sum_{n=0}^{N} (-1)^n T_{\ell n}^{m} = 0 \quad \forall \ell, m \neq 0 \,. \tag{1.72}$$

1.A.4.3 Solution of the system

The equations of the predictor-corrector scheme coupled with the appropriate boundary conditions can be written in a matrix form for each degree ℓ and order m independently (Glatzmaier (1984)) such as

$$A_{in} X_n = B_i \tag{1.73}$$

where i corresponds to the index of depth, and n the degree of Chebyshev polynomials. The size of the matrix A is $(N+1) \times (N+1)$. The first and last line of the matrix A_{in} correspond to the boundary conditions given by equations (1.69) through (1.72).

There are $L(L+1)/2$ systems of form (1.73) to be solved where L is the maximum degree of the spherical harmonic expansion. Since A_{in} does not depend on m (see eq. 1.62), there are only L matrices to be inverted. The LU decomposition method is used to invert the matrices. The decompositions may be stored because the A_{in}'s do not depend on time. However, they depend on Δt which may vary due to numerical stability requirements (see eq. 1.74) and we must therefore recompute the matrices.

The solutions X_n of the systems (1.73) are the Chebyshev and spherical harmonic coefficients of the temperature $T_{\ell n}^m(t)$. These coefficients will be used to recompute the new radial derivatives as in (1.51) needed for the evaluation of the spherical harmonic coefficients of the diffusive term in (1.52) and in the calculation of $\nabla^0 T$ in eq. (1.53). Then, the spherical harmonic coefficients $T_\ell^m(r,t)$ will be synthesised at every depth to evaluate $\nabla^- T$ and $\nabla^+ T$ in (1.53).

1.A.4.4 Numerical stability requirements

The Crank-Nicholson scheme is unconditionally stable whereas restrictions apply on the size of the time step which are necessary to maintain the stability of the advective scheme (Glatzmaier (1984)). The length of the time step is controlled by the Courant criterion which must be satisfied at any time:

$$\Delta t \leq \left|\frac{\Delta r}{u_r}\right|_{\text{MIN}} \text{ and } \Delta t \leq \left|\frac{r}{\sqrt{L(L+1)(u_\theta^2+u_\phi^2)}}\right|_{\text{MIN}} \tag{1.74}$$

where u_r, u_θ and u_ϕ are velocity components. Typically, in actual numerical simulations, we set Δt to be half of the maximum value allowed by the above expressions.

1.A.4.5 Alias-free transformations

As described above, the computation of non-linear terms requires that we jump back and forth between the spatial (r,θ,ϕ) and spectral (ℓ,m,n) domains. This method may be aliased if the number of mesh-points in the physical space is insufficient to sample adequately with respect to the maximum spherical harmonic degree L and the maximum Chebyshev polynomial degree N. The physical grid consists of Chebyshev nodes in radius, Gauss-Legendre nodes in latitude and equally-spaced FFT nodes in longitude. Alias-free transformations between physical space and spherical harmonics require (3L+1)/2 points in latitude and (3L+1) points in longitude (Glatzmaier (1984)). Also, the presence of the strong non-linear term in thermal convection may trigger the appearance of aliasing with the ability to perturb the process. The application of a spectral filter acting over the range of harmonic degrees of the non-linear (advection) term may be one method for controlling numerical instabilities arising from aliasing of short wavelength perturbations into longer wavelength terms. In this study we used two spectral filters:

one isotropic (linear) for all ℓ

$$f_{\text{lin}}(\ell) = 1 - \frac{\ell}{L} \tag{1.75}$$

and the other, a Lanczos filter only for $l \geq 1$

$$f_{\text{lan}}(\ell) = \frac{\sin(\ell\pi/L)}{(\ell\pi/L)} \,. \tag{1.76}$$

1.B Computational aspects of the numerical code

The thermal convection code utilised for all calculations presented in this paper is written in standard C++ language. The Blitz++ library is used for the management of large multidimensional arrays in order to be competitive with Fortran90 performances. The MPI-2 library is employed for the purpose of parallelisation of the code for use on a multiprocessor computer cluster. The parallelisation is mostly done over radial and latitudinal nodes and only the predictor-corrector method is distributed to processors over spherical harmonics degrees. In this way we avoided a lot of communication between processors. Although this strategy yields gain in speed, we must deal with the limitation of the fixed size of dynamic memory available on each processor, which obviously does not increase with the size of the cluster (see Table 1.5). This limitation currently prevents us from using harmonic expansions up to L=512 because we then require more than 4 Gb per processor. All simulations are done on the General Purpose Cluster (GPC) of the SciNet consortium at the University of Toronto, using Infiniband network where each node has 8 processors and the RAM per node is 16 Gb.

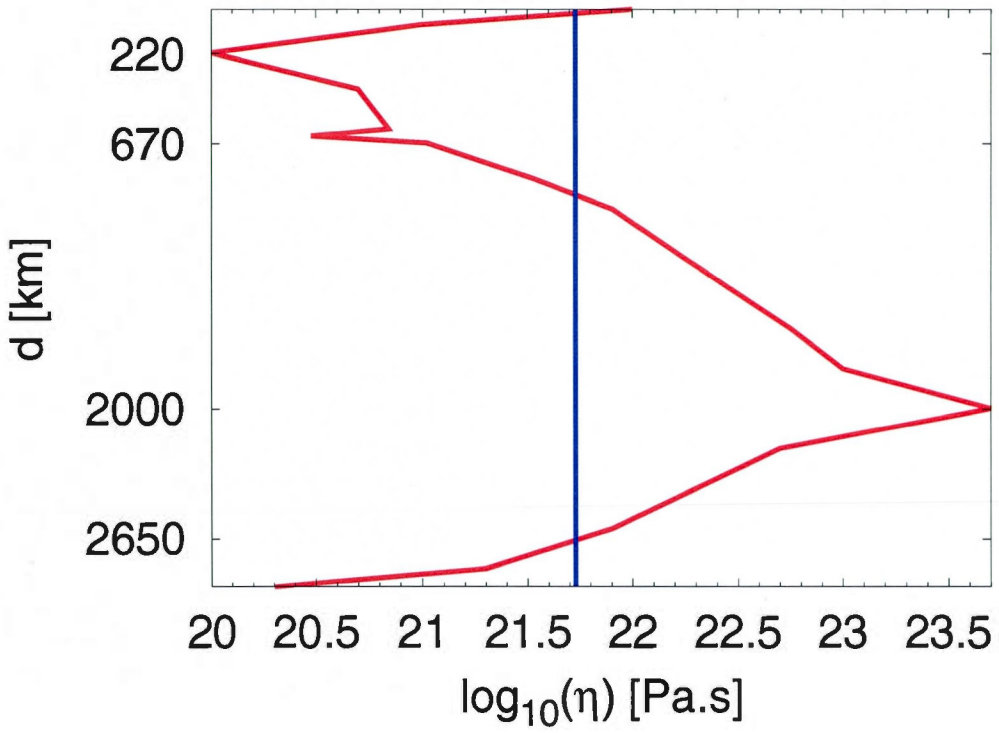

Figure 1.1: Viscosity profiles. The geodynamically inferred (Mitrovica & Forte (2004) and Forte et al. (2010)) V2-profile (red line) is characterized by a two order of magnitude reduction in viscosity across the uppermost mantle, where 220 km is the depth at which the V2-profile has minimum viscosity. Deeper in the mantle, there is a great increase in viscosity, about 1600×, from 635 km to 2000 km depth - where the latter corresponds to the depth of maximum viscosity in the mantle. In the lower 900 km of the mantle, the V2 profile exhibits a 3-order of magnitude decrease of viscosity extending down to the CMB. The ISOV-profile (blue line), is constant and characterises a logarithmic average of the whole-mantle value derived from the V2 profile.

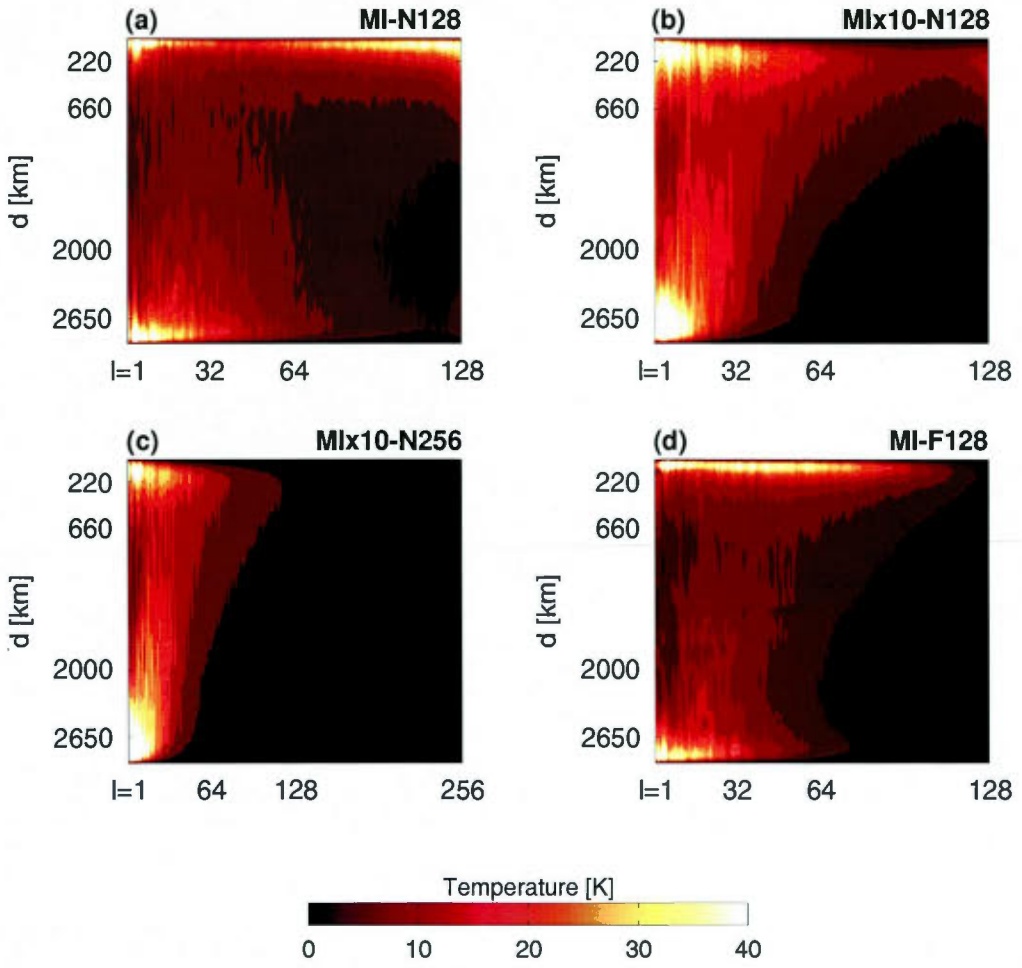

Figure 1.2: The root-mean-square (rms) spectral amplitudes of the mantle temperature heterogeneity for iso-viscous convection models after 290 Myr of time integration from the point of 3.845 Ga (see text). The rms amplitudes are represented on the Kelvin-temperature scale as a function of spherical harmonic degree (y-axis) and depth (x-axis).

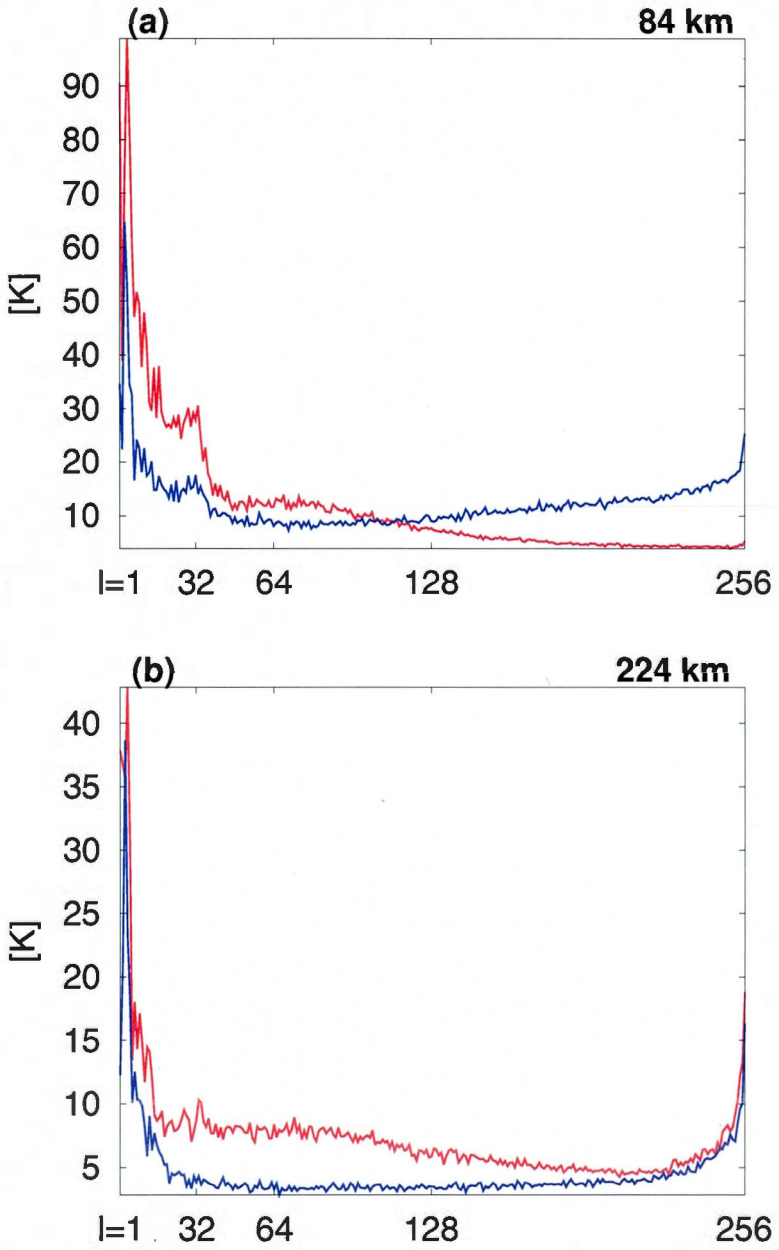

Figure 1.3: The root-mean-square (rms) spectral amplitudes of the mantle temperature heterogeneity (y-axis) as a function of spherical harmonic degree (x-axis) for V2 convection models at different depths: (a) 84 km, (b) 224 km after 250 Myr of time integration from the present-day. The blue line indicates the MV2-N256 model, and the red line shows the MV2x10-N256 model (see text).

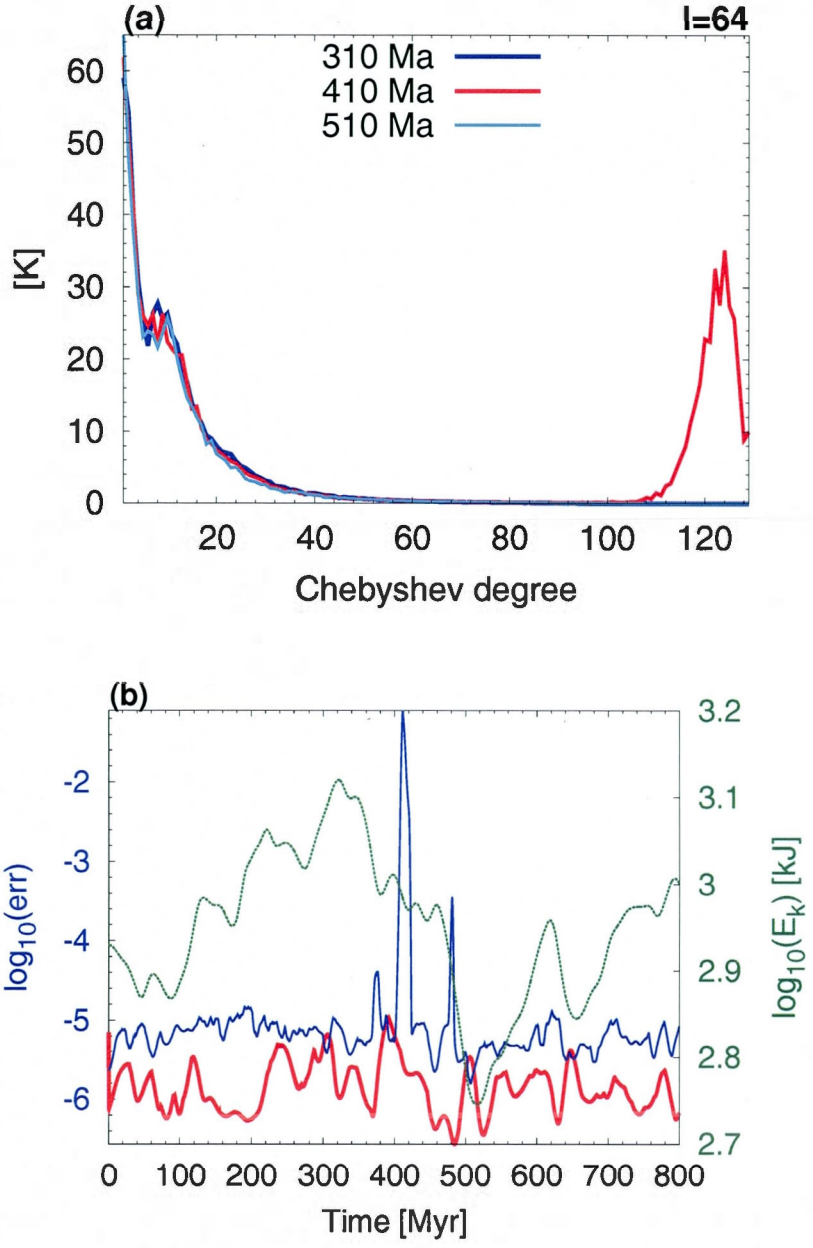

Figure 1.4: (a) The root-mean-square (rms) spectral amplitudes of $\ell = 64$ (y-axis) as a function of Chebyshev polynomial degree (x-axis) for the iso-viscous MI-N128 (without filter) model at different points of time: 310 Ma (blue line), 410 Ma (red line) and 510 Ma (cyan line). (b) The temporal evolution of the local rms error of the predictor-corrector time-stepping method for the iso-viscous simulations: MI-N128 (blue curve) and MI-F128 (with filter, red curve). The green (dashed) curve represents the logarithmic variations of total integrated kinetic energy for the MI-N128 model over 800 Myr.

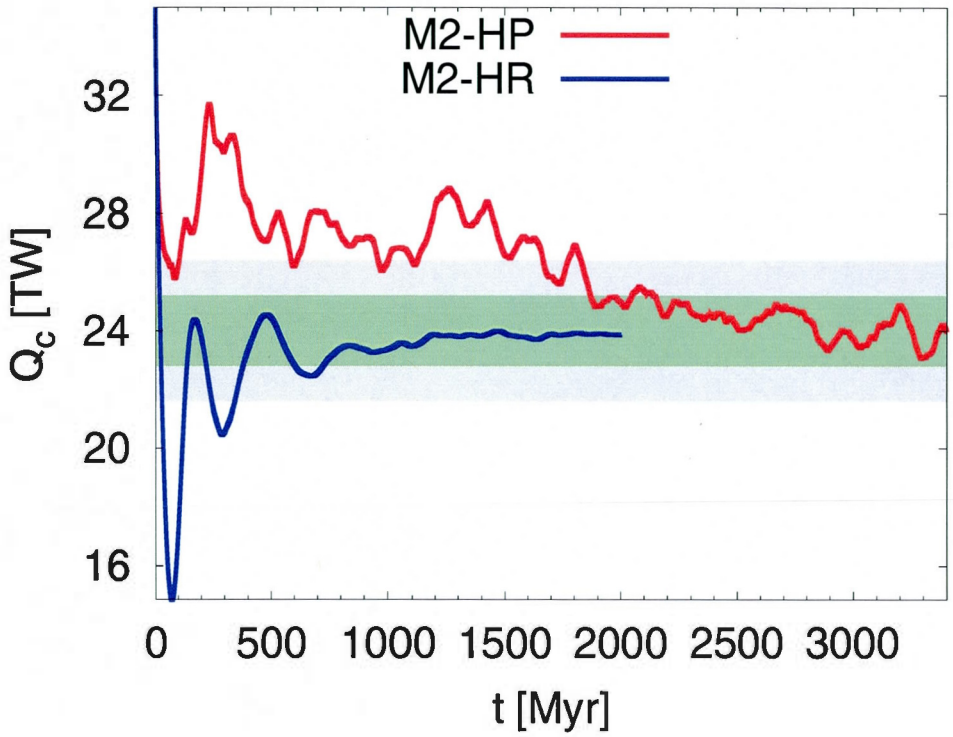

Figure 1.5: Time-dependent internal heating. The temporal evolution of internal heat production (Q_c) for two convection simulations (M2-HP, with surface plates and M2-HR, with rigid surface) is calculated by differencing the heat flux at the surface (F_s) and CMB (F_c), such that $Q_c = F_s - F_c$. The green rectangle represents a 5% deviation with respect to the expected steady-state value (i.e., 24 TW of imposed internal heating), while the grey represents a 10% deviation.

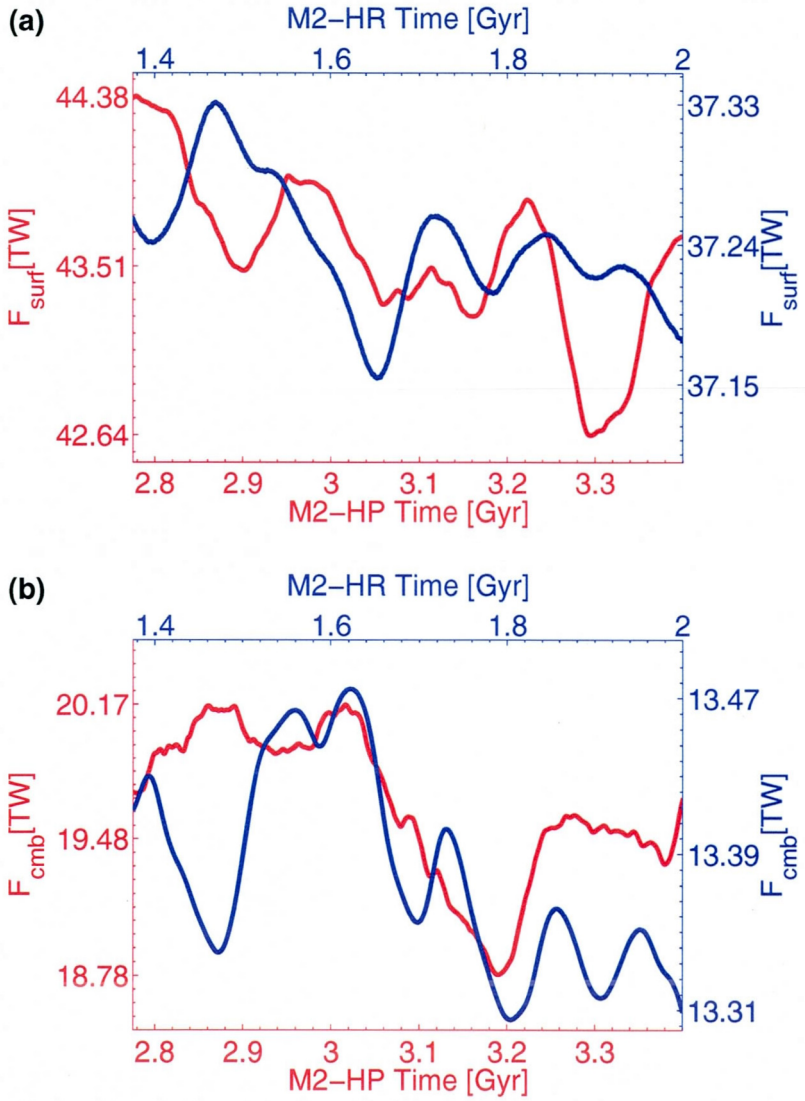

Figure 1.6: Time-dependent heat flux at the surface and CMB. The top and bottom frames show temporal variations of (a) surface and (b) bottom heat flux, respectively, for the M2-HP (with surface plates) and M2-HR (rigid surface) convection simulation over the final 625 Myr during which steady-state conditions prevail.

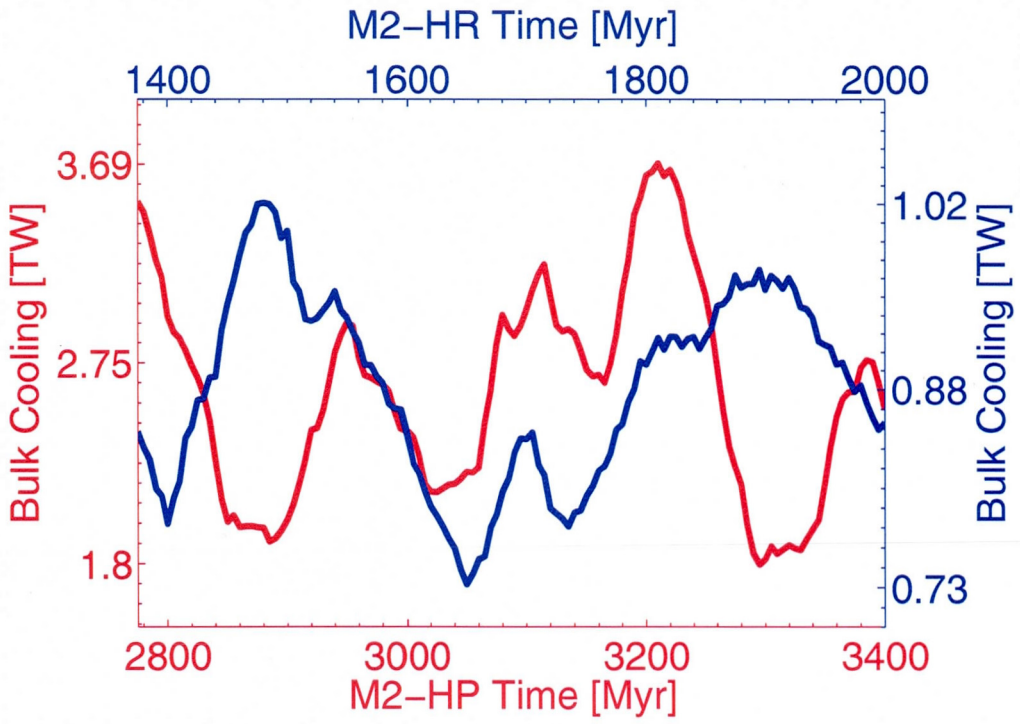

Figure 1.7: Temporal evolution of bulk cooling. The red and blue curves show the numerically determined bulk cooling of the mantle for the M2-HP (surface plates) and M2-HR (rigid-surface) convection simulations, respectively. These numerically-calculated bulk cooling rates measure the extent to which the mantle geotherm departs from steady-state conditions.

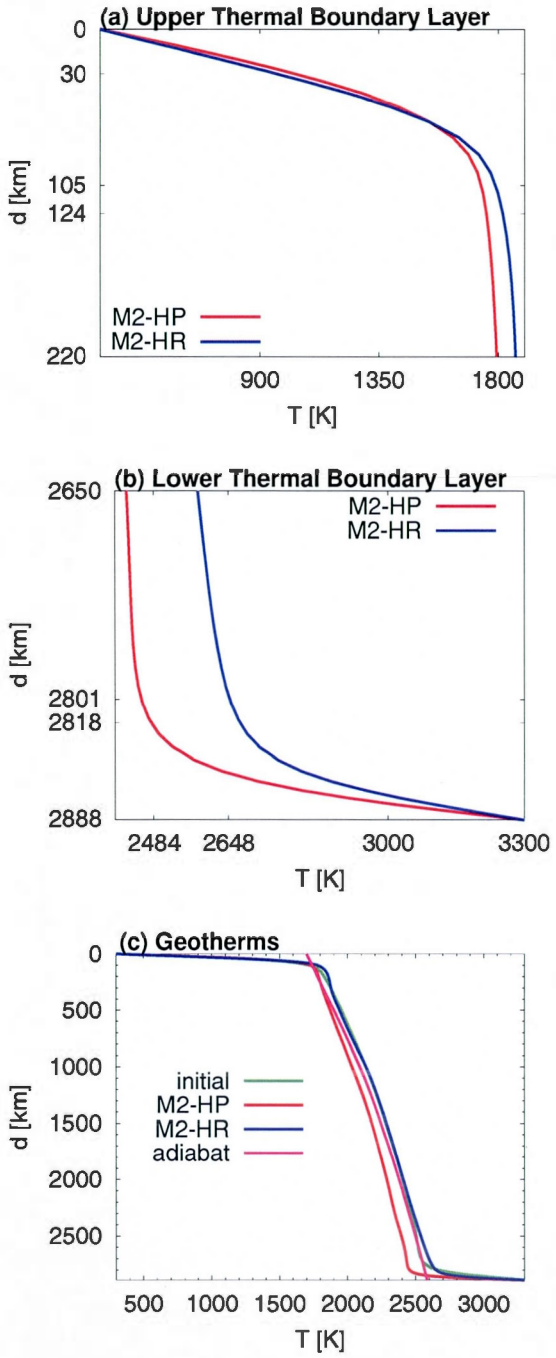

Figure 1.8: Global horizontally-averaged mantle thermal structure at the end of the steady-state interval for the M2 convection simulations.

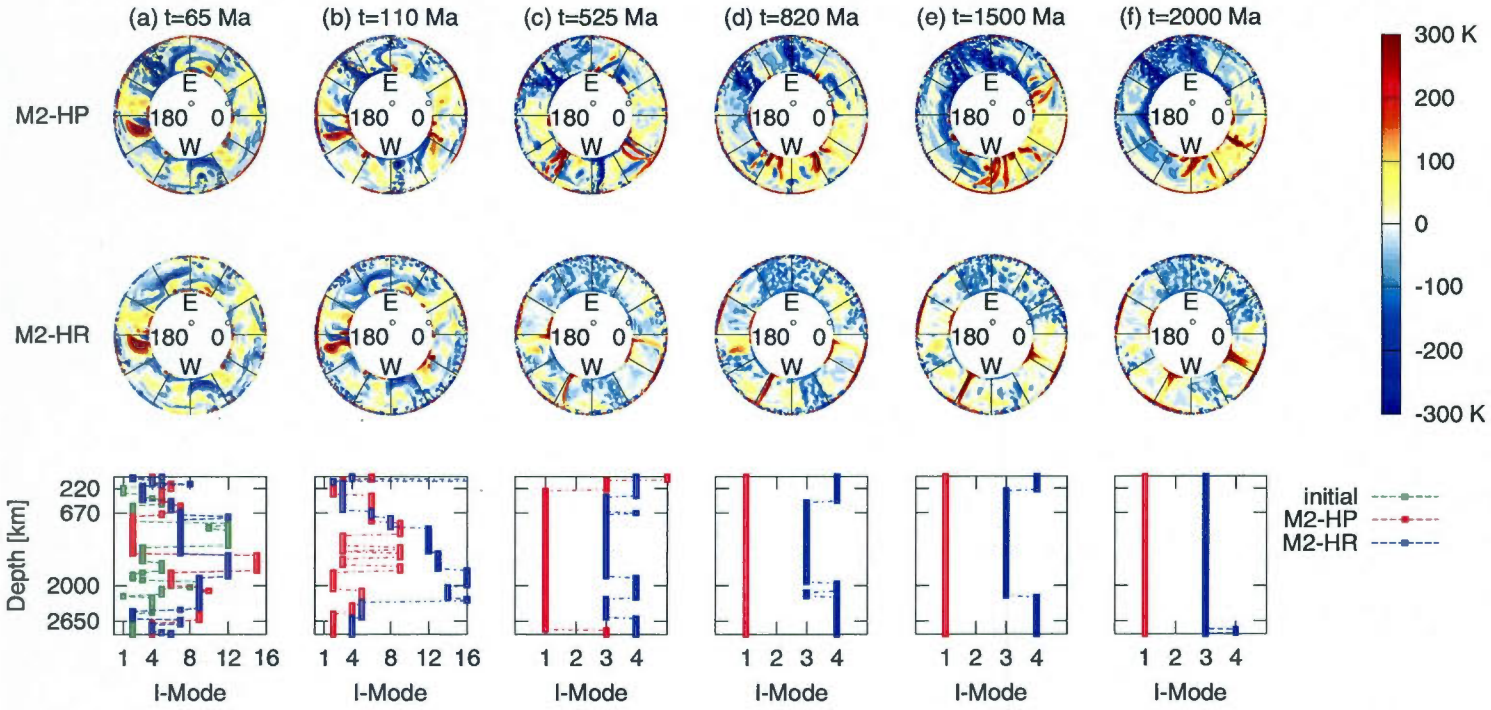

Figure 1.9: Time-dependent evolution of lateral temperature variations driven by mantle convection. In the top two rows are shown equatorial cross-sections of evolving temperature heterogeneity from 65 Ma (left), estimated from seismic tomography (Simmons et al. (2009)), to 2 Ga into the future (right). The 1st and 2nd rows show the M2-HP (surface plates) and M2-HR (rigid surface) results, respectively. The bottom (3rd) row shows the dominant mode of convection (i.e. maximum spectral amplitude of thermal heterogeneity) as a function of depth at each instant in time.

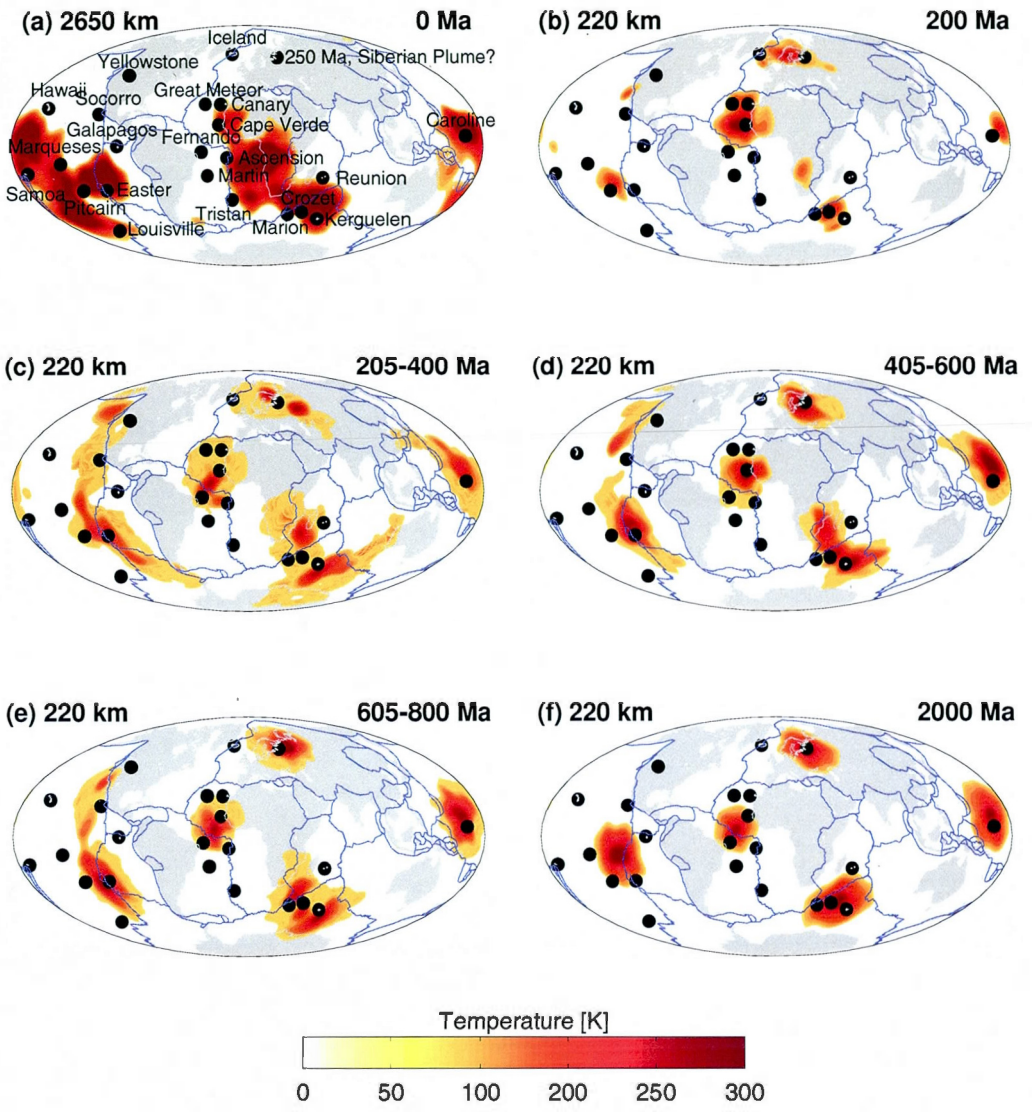

Figure 1.10: The first map (a) shows the present-day positive heterogeneity ($T \geq 100$ K) at a depth of 2650 km. The maps from (b) to (f) represent positive lateral temperature variations ($T \geq 100$ K) at a depth of 220 km obtained by the M2-HR (rigid surface) convection simulations at different points/intervals of time: (b) 200 Ma, (c) 205-400 Ma, (d) 405-600 Ma, (e) 605-800 Ma and (f) 2 Ga. The black circles show the location of present-day hotspots (Courtillot et al. (2003)).

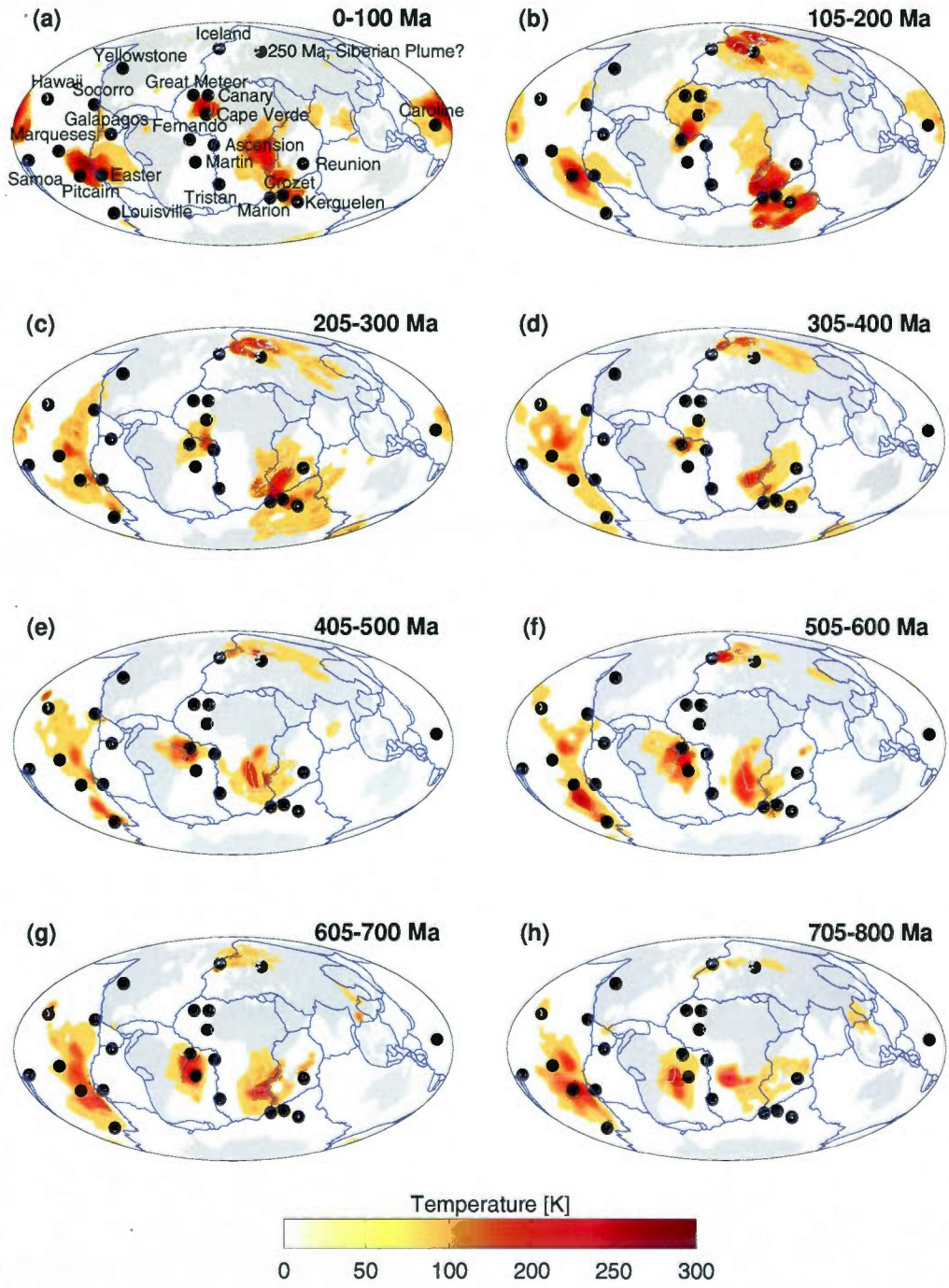

Figure 1.11: The superimposed 5-Myr time-sequences of positive heterogeneity ($T \geq 100$ K) at the depth of 220 km obtained by the M2-HP (plates) model at different time-windows (Ma): (a) 0-100, (b) 105-200, (c) 205-300, (d) 305-400, (e) 405-500, (f) 505-600, (g) 605-700 and (h) 705-800. The black circles show the location of present-day hotspots (Courtillot et al. (2003)).

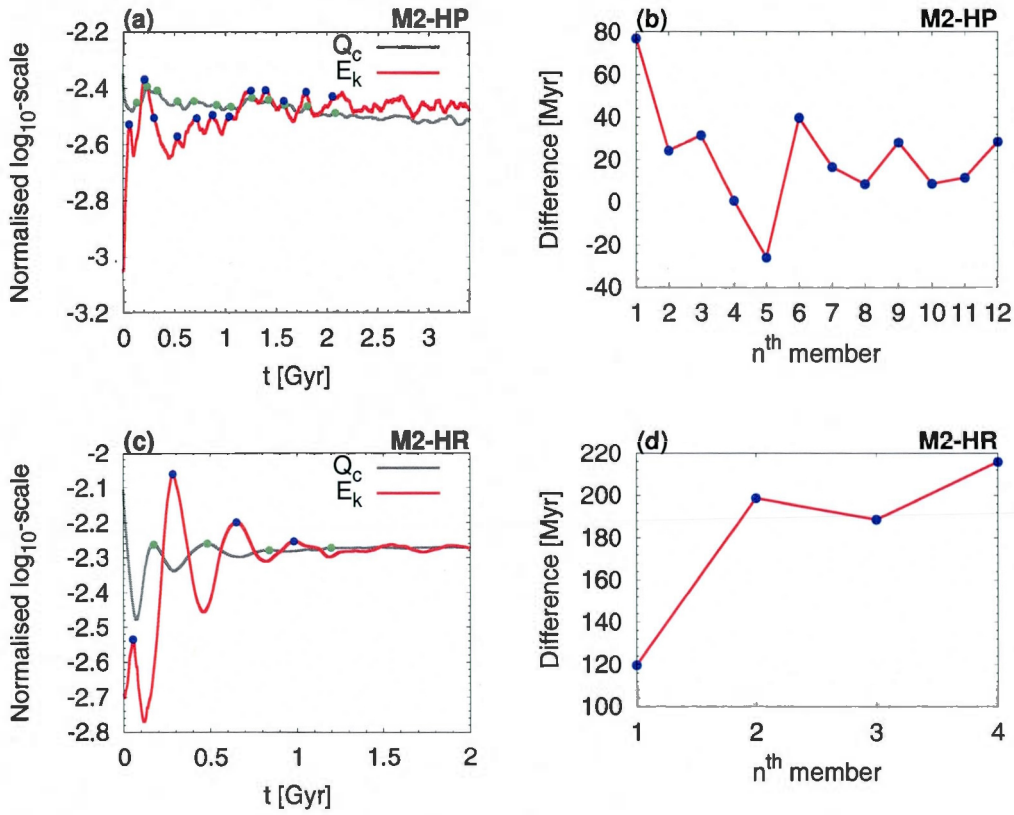

Figure 1.12: The temporal variation of total integrated kinetic energy (E_k) in (a) the surface plates and (c) rigid-surface convection simulations. It seems that the fluctuations of kinetic energy (red curve) and the estimated internal heating (Q_c, grey curve) are closely coupled. Making a sequence of coupled maximum values for E_k (blue circles) and Q_c (green circles) over successive time-windows up to 2 Ga and 1 Ga for the M2-HP and M2-HR models, respectively, we can calculate the difference between the moments of maximum as a function of sequence member - (b) and (d).

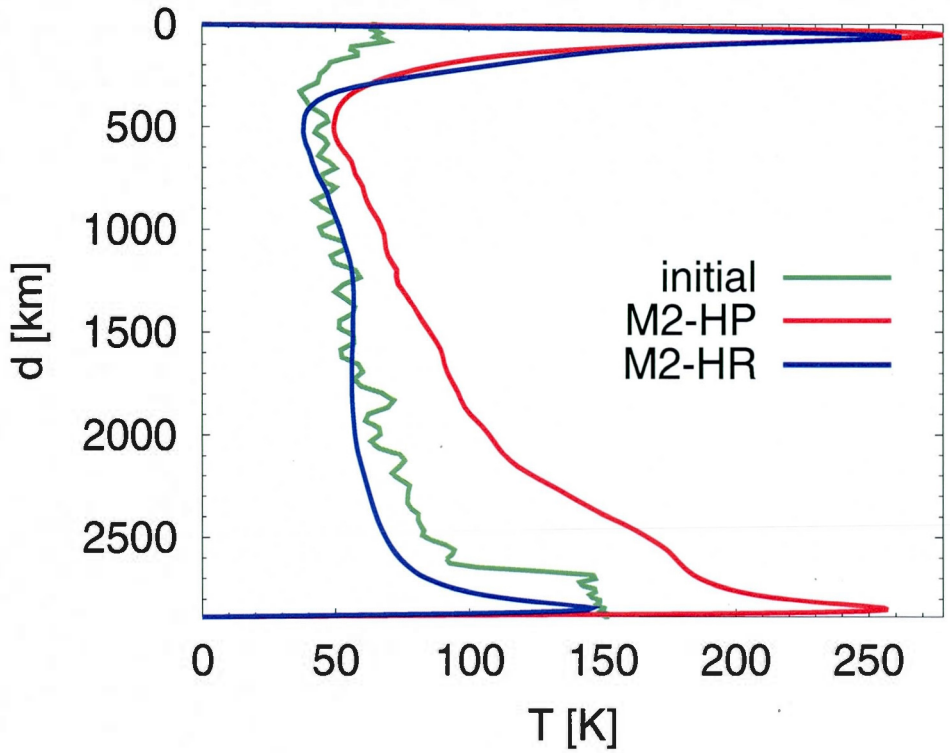

Figure 1.13: Globally-averaged, root-mean-square (rms) amplitude of lateral temperature variations as a function of depth. The green curve shows the present-day rms temperature anomalies derived from seismic tomography (Simmons et al. (2009)). The red and blue curves shows the steady-state temperature anomalies for the M2-HP (surface plates at time 3.4 Ga) and M2-HR (rigid surface at time 2 Ga) convection simulations, respectively.

Table 1.1: Physical parameters and values employed in simulations of thermal convection of the mantle. Values in this table were kept constant in all simulations of thermal convection of the mantle. Details of viscosity profiles are given by Fig. 1.1.

Parameter	Value	Unit of Measure
Outer shell radius	6368	km
Inner shell radius	3480	km
Temperature (surface)	300	K
Temperature (cmb)	3300	K
Density ρ	PREM model	kg m^{-3}
Reference viscosity η_{ref}	1×10^{21}	Pa.s
Heat capacity c_p	1.25×10^{3}	J kg^{-1} K^{-1}
Thermal expansion α (surface)	3.5×10^{-5}	K^{-1}
Thermal expansion α (670 km)	2.5×10^{-5}	K^{-1}
Thermal expansion α (CMB)	1.0×10^{-5}	K^{-1}
Thermal conductivity k (surface)	3.3	W m^{-1} K^{-1}
Thermal conductivity k (80 km)	2.5	W m^{-1} K^{-1}
Thermal conductivity k (2650 km)	6.25	W m^{-1} K^{-1}
Thermal conductivity k (CMB)	4.8	W m^{-1} K^{-1}
Internal heating rate Q_{int}	6.0×10^{-12}	W kg^{-1}

Table 1.2: Values of mean heat flow and its standard deviation for M2-HP and M2-HR models on two equal time intervals with maximum 5% deviation from true steady-state values. Evolution of heat flow on the last 625 Myr of M2-HP and M2-HR simulations is presented in Fig. 1.6.

	M2-HP		M2-HR		Mareschal et al. (2012)
	[2150,2775]	[2775,3400]	[750,1375]	[1375,2000]	
F_s	44.09	43.58	37.24	37.24	[37,41]
σ_{F_s}	0.27	0.41	0.07	0.04	
F_c	19.52	19.67	13.68	13.38	[4,14]
σ_{F_c}	0.20	0.38	0.22	0.05	
Q_s	3.37	2.60	0.61	-0.88	
σ_{Q_s}	0.39	0.50	0.23	0.07	

Table 1.3: The location of the plume-centres obtained by the M2-HR simulation at t=2 Ga (Fig. 1.10) that may be connected by the present-day hotspots with its indicator of deep origin track.

The location of the plume-centres in convection model	The present-day hotspots (Courtillot et al. (2003))	Deep origin track (Courtillot et al. (2003))
11°S 114°W	Easter (27°S 110°W)	yes
	Pitcairn (26°S 130°W)	yes
	Galapagos (0°S 92°W)	yes?
	Marqueses (10°S 138°W)	yes
4°N 28°W	Fernando (4°S 32°W)	yes?
	Ascension (8°S 14°W)	no
	Cape Verde (14°N 20°W)	no
44°S 56°E	Kerguelen (49°S 69°E)	yes
	Marion (47°S 38°E)	yes
	Crozet (45°S 50°E)	yes?
	Reunion (21°S 56°E)	yes
10°N 164°E	Caroline (5°N 164°E)	yes
62°N 39°E	n/a	n/a

Table 1.4: The location of present-day hotspots, and the approximate time interval of their appearance at the depth of 220 km for both convection simulations (M2-HR and M2-HP) during the first 800 Myr.

The present-day hotspots (Courtillot et al. (2003))	Period of activity detectable by theM2-HR (see Fig. 1.10)	Period of activity detectable by the M2-HP (see Fig. 1.11)
Samoa (14°S 170°W)	none	none
Marqueses (10°S 138°W)	none	205-400 & 705-800
Pitcairn (26°S 130°W)	up to 800	up to 200 & 505-800
Easter (27°S 110°W)	205-800	up to 300
Louisville (0°S 92°W)	none	405-700
Hawaii (20°N 156°W)	none	405-800
Socorro (19°N 111°W)	205-400 & 605-800	up to 300 & 405-500
Galapagos (0°S 92°W)	none	up to 100
Yellowstone (44°N 111°W)	205-400	none
Great Meteor (28°N 32°W)	up to 400	up to 200
Canary (28°N 20°W)	up to 400	up to 200
Cape Verde (14°N 20°W)	up to 800	up to 400
Fernando (4°S 32°W)	205-800	105-800
Martin (20°S 29°W)	none	505-800
Ascension (8°S 14°W)	205-600	205-400
Tristan (37°S 12°W)	none	none
Iceland (65°N 20°W)	up to 400	505-800
Siberian Plume?	up to 800	105-300 & 405-600
Reunion (21°S 56°E)	205-400	205-300 & 605-800
Marion (47°S 38°E)	up to 400 & 605-800	105-400 & 505-700
Crozet (45°S 50°E)	up to 800	up to 400 & 505-700
Kerguelen (49°S 69°E)	up to 800	up to 400
Caroline (5°N 164°E)	205-800	up to 100

Table 1.5: Computational properties of the numerical convection code.

L	# of CPUs	RAM (Gb) per CPU	Calculation Time per iteration (sec)
128	32	0.60	28
128	128	0.55	14
256	64	1.51	49
256	128	1.50	40
512	128	4.77	-

CHAPTER II

IMPORTANCE OF INITIAL BUOYANCY FIELD ON EVOLUTION OF MANTLE THERMAL STRUCTURE: IMPLICATIONS OF SURFACE BOUNDARY CONDITIONS

Submitted to *Physics of the Earth and Planetary Interiors* (2012).

2.1 Résumé

Bien qu'il y ait eu des progrès récents dans la modélisation sismique de l'hétérogénéité actuelle du manteau, il existe toujours la question concernant la distribution inconnue des forces d'Archimède dans le lointain passé géologique et de son impact sur l'évolution de la structure thermique du manteau. Afin de répondre à cette question, nous présentons des modèles de convection dépendant du temps en géométrie sphérique tridimensionnelle, dans un manteau compressible et dissipatif, initialisés par différentes variations latérales de température. Nous démontrons que la structure initiale thermique est fortement imprimée sur l'évolution future du manteau, et aussi que la mesure dans laquelle l'hétérogénéité initiale du manteau détermine la distribution finale de la température dépend des conditions limites à la surface de la Terre. Nous proposons également que les profonds panaches mantelliques sous les points chauds suivants : Pitcairn, Pâques, Galápagos, Crozet, Kerguelen, Caroline, et le Cap-Vert sont les mieux résolues dans les images de la tomographie sismique globale.

2.2 Abstract

Although there has been recent progress in the seismic modelling of mantle heterogeneity, the question regarding importance of the initial buoyancy field constrained by tomography on the evolution of mantle thermal structure still exists. In order to address this outstanding question, we present time-dependent, compressible, and dissipative convection models in three-dimensional spherical geometry initialised by different lateral temperature variations. We demonstrate that an initial thermal structure is strongly imprinted on the future mantle evolution, and also that the extent to which a starting mantle heterogeneity determines the final temperature distribution depends on the surface boundary conditions. We also suggest that the deep-mantle plumes beneath the following hotspots: Pitcairn, Easter, Galapagos, Crozet, Kerguelen, Caroline, and Cape Verde are most-likely resolved by the present-day tomographic imaging.

2.3 Introduction

Time-dependent models of mantle flow are most often initialised by a theoretically perturbed buoyancy field with free-slip surface boundary condition (e.g., Davies & Davies (2009)), that may, in some cases, also include surface geological constraints such as tectonic plate velocity histories (e.g., Schuberth et al. (2009b)). A more realistic internal loading state of the mantle can be provided by seismic tomography. Seismic images of present-day mantle heterogeneity have commonly been used in models of the instantaneous flow where the goal has been to fit convection-related surface geodynamic data (Hager & Clayton (1989); Forte (2007)). More recently, Glišović et al. (2012) showed that the present-day lateral temperature variations constrained by tomography may provide an essential imprint on the mantle flow organisation, however, the importance of the initial buoyancy field on the evolution of Earth's internal structure is still unclear.

Additional complexity in determining the extent to which the 'final' (i.e. steady-state) temperature distribution depends on the initial mantle heterogeneity is introduced by surface boundary conditions. Namely, the dynamic impact of plates plays a crucial role in the Earth's mantle flow - organizing and modulating cold downwellings and hot upwellings (e.g., Quéré & Forte

(2006)). This impact is highly constrained by: (1) constantly evolving plate geometries over the past 200 million years (e.g., Müller et al. (2008)); (2) the inability to reconstruct mantle heterogeneity after 100 Ma (Bunge et al. (2002)); (3) no currently accepted theory for accurately predicting the future evolution of plate geometries over very long geological time spans, in a manner that is dynamically self-consistent with the underlying mantle flow. Despite the highly questionable assumption that plates retain their present-day configuration over very long time spans, this is still one of the possibilities for modelling 'Earth-like' convection circulation.

Another possibility is to explore long-time convection simulations with a rigid surface (i.e., no-slip) boundary condition to avoid eventual geometric and dynamical bias of assuming fixed plate locations. Glišović et al. (2012) have shown the ability of a model with a rigid surface, first, to reinforce the hot, plume-like structures in the starting tomography, and then, to produce stable and long-lived deep-mantle plumes that reveal an intriguing spatial relationship to the surface constellation of hotspots and other manifestations of intra-plate volcanism (e.g., Siberian traps). Additional perspective of modelling terrestrial mantle flow with a rigid surface may be gained from the facts that: (1) Venus is planet without tectonics (Schubert et al. (1990)), and (2) in terms of size, mass, and density, Venus is the planet most similar to the Earth (Schubert et al. (2001)).

Therefore, the main objective of this study is to determine the influence of initial mantle heterogeneity on the final temperature distribution and in particular, how this influence depends on surface boundary conditions.

2.4 Numerical model, initial conditions and reference frame

We used a dissipative and compressible 3-D pseudo-spectral method (Glišović et al. (2012)) to model the thermal convection in the mantle. This method requires the initialization of different thermal structures described by both the horizontally-averaged temperature and lateral variations in temperature.

2.4.1 Initial geotherm

The sensitivity of geotherm to the reference state (e.g., depth-dependent rheology) and surface boundary conditions is well-known. Therefore, we used previously determined steady-state geotherms (Glišović et al. (2012)) characterized by thermal boundary layers (TBLs) bounding an adiabatic portion (see Fig. 2.1a). These profiles of the global horizontally-averaged temperature deliver surface heat flux in the range of Earth-like values (Jaupart et al. (2007)): 37 TW for a rigid surface and 44 TW for the surface with tectonic plates coupled to the mantle flow. Moreover, the core-mantle boundary (CMB) heat flux is on the high end of previously estimated values (Lay et al. (2006)), namely 13 TW and 20 TW, for rigid and plate-like surface boundary conditions, respectively.

2.4.2 Initial mantle heterogeneity

In convection simulations with coupled surface plates, Glišović et al. (2012) showed a strong reinforce of present-day topographically-inferred heterogeneity mainly owing the intense accumulation of subducted cold material that enters the lower mantle directly under the Indonesian and Western Pacific. These strong downwellings have a crucial role in forming the steady-state hemispherical mantle flow characterized by degree-1 structure. The geologically-inferred dominance of subduction along the margins of the paleo-Pacific since the Precambrian (e.g., Scotese (2001)) may suggest that this hemispherical pattern of cold downwelling is not unreasonable. In order to address the importance of this region for mantle evolution, we perform a convection simulation (IND model) initialised only by negative temperature anomalies beneath the equatorial part of Indonesia. The negative anomaly is given by a box: 15° in longitude, 5° in latitude (15° × 5°), in the first 220 km of mantle depth.

Opposite to the Western Pacific subduction chains is the East Pacific Rise - a divergent tectonic boundary that separates the Pacific plate from the North American plate, the Rivera plate, the Cocos plate, the Nazca plate, and the Antarctic plate. The Pacific plate constitutes an essentially uniform surface boundary and consequently theoretical modelling of flow in the Pacific hemisphere should be less complex than in sub-continental mantle where there may be interactions with continental roots (Gaboret et al. (2003)). Therefore, initializing the lateral

temperature variations by the positive anomaly beneath the equatorial part of the East Pacific Rise we create the antipodal simulation (EPR model) to the previously defined IND model. The signal of hot material is a $15° \times 5°$ area inside the D"-layer.

It has long been assumed that large-scale, deep-mantle dynamics under the African plate is dominated by the influence of a superplume located under southern Africa (e.g., Behn et al. (2004)). Recently, the application of thermochemical convection modelling to the problem of African mantle dynamics revealed a deep-seated, large-scale, active hot upwelling below the western margin of Africa (Forte et al. (2010)). The scale and dynamical intensity of this 'West African Superplume' (WASP) is comparable to the 'South African Superplume' (SASP). However, Forte et al. (2010) showed that the negative chemical buoyancy inferred within the core of the SASP opposes its positive thermal buoyancy and thereby exerts a strong stabilising control on the mantle flow driven by this plume. Thus, it would be worthwhile to perform a thermal convection simulation initialised by the hot region ($15° \times 15°$) inside the D"-layer beneath South Africa (SAP model).

2.4.3 Surface boundary conditions

The surface boundary conditions are another important constituent of mantle convection. Fundamentally, there are three different boundary conditions: rigid surface (R), free-slip (F), and rigid plates (P). In this study we use two of them: the R- and P-boundary conditions.

The no-slip (R) boundary condition would be applicable in the event that all tectonic plates simultaneously resist the underlying mantle flow, or for the planets without plate tectonics (e.g., Venus).

The free-slip boundary condition is usually coupled with a high-viscosity lithospheric lid and a weaker interior, either depth- or temperature-dependent, often refereed as 'stagnant-lid' (e.g., Roberts & Zhong (2006)), or 'sluggish-lid' convection (e.g., Yoshida (2008)). Therefore, for the stagnant- or sluggish-lid convection, surface deformation may occur continuously because the upper bounding surface is free-slip.

In the case of the P-boundary condition, the plate velocities are predicted at each instant in time, on the basis of the evolving distribution of buoyancy forces in the mantle avoiding the

approach where prescribed surface plate velocities (e.g., McNamara & Zhong (2005)) require an external driver of energy source that can compromise the energy balance of the mantle. The one drawback of coupled tectonic plates (P-boundary condition) is that the plate geometry itself is assumed constant. This is clearly questionable, in terms of evaluating whether we are modelling the 'real Earth' a billion or more years from now. It is important to underline that despite the drawback of assumed plate geometry, a present-day subduction zone is free to evolve into a future spreading centre, and vice versa, in response to the evolving heterogeneity in the mantle. Also, the P-boundary condition involves the generation of toroidal flow via the surface-plate rotations and this is not the case for the two other boundary conditions (R or F). The toroidal flow is expected to be the result of significant lateral viscosity heterogeneities (e.g., Forte & Peltier (1987)) and it contributes almost 50% of the kinetic energy of the plate (Hager & O'Connell (1978)). Moreover, the coupling of surface plates employing the P-boundary condition requires a consideration of both rigid and free-slip flow kernels and hence this condition is, in a sense, intermediate between the R- and F-boundary conditions.

2.4.4 Reference state of the mantle

The effect of lateral viscosity variations (LVV) may be important, but the key outstanding issue, one that is far from resolved in the current convection models, is how to model the LVV in such a way that yields a fit to the surface geodynamic constraints and also to the mineral physics. There are a number of fundamental uncertainties in the mineral physical interpretations of the origin of LVV in the mantle and confronted with this difficulty we have therefore opted, as a prudent alternative, to use the depth-dependent viscosity profile (Fig. 2.1b) that directly fits the convection-related surface observables (Forte et al. (2010)) as well as the independent mineral physical modelling (Ammann et al. (2010)) and data associated with the response of the Earth to ice-age surface mass loading (Mitrovica & Forte (2004)).

In this study we employ a thermal conductivity profile given by Hofmeister (1999) that considers the effect of TBLs inside the mantle and the possibility that thermal conductivity decreases with the depth across both layers (Fig. 2.1c).

Tackley (2000) suggested a few scenarios for the radiogenic heat distribution in the man-

tle, but this distribution remains unknown. Also, the heat production of the crust is the only reliable data set in the equation of the present mantle energy budget, where other constituents are unknown (Mareschal et al. (2012)). Thus, values of secular cooling lie between 8 and 18 TW, and the radioactive heat ranges from 9 to 16 TW (Jaupart et al. (2007)). Combining these assumptions to fit the energy balance produced by the steady-state geotherms (Glišović et al. (2012)), we designed the depth-dependent profile of heat production as the summation of two components: the radiogenic and the secular cooling (Fig. 2.1c). We assumed the secular cooling to be uniform giving the total of 12 TW (i.e. ~ 76 K per Gyr). The radiogenic heat is also uniform from the surface to 2200 km depth producing 4 TW, but from 2200 km to CMB it linearly increases delivering 8 TW; therefore, the total value of mantle heating due to radioactive sources is 12 TW.

The radial density profile, which describes the reference hydrostatic state in our compressible convection model, is taken directly from the seismic reference Earth model PREM (Dziewonski & Anderson (1981)). The corresponding radial gravity field is obtained by the integration of reference density (Fig. 2.1d).

Other physical parameters and values employed in the simulations of mantle convection are summarised in Table 2.1, and with all others, they are kept constant during the time-integration of models.

All models are run until they have reached the statistical steady-state.

2.5 Results and discussion

2.5.1 Rigid surface

Models with a rigid surface are not impacted by the projection of present-day plate geometries, and we expect to observe the establishment of both the strong deep-mantle plumes and weak downwellings (Schubert et al. (1990); Glišović et al. (2012)). Therefore, hot upwellings are dominant thermal structures in the case of the no-slip boundary condition, and the vigour of plumes is directly connected to the intensity of CMB heat flux (e.g., Schuberth et al. (2009b), Glišović et al. (2012)). Analysing temporal variations in the heat flux at the CMB (Fig. 2.2a), we notice a peak between 300 and 400 Ma for all models which coincides with the first appear-

ance of numerous hot diapirs (reinforced or created inside the D"-layer depending on the initial buoyancy field) at sub-lithospheric depths (Figs 2.3a, 2.3b, and 2.3c). However, the system is still in a transient period allowing the additional reorganisation of mantle circulations (e.g., around 700, 1000, and 1300 Ma, see Fig. 2.2a). Namely, these changes in the mantle flow may be explained by the merging of a pair of plumes that exist for the IND and SAP R-simulations (Figs 2.3d and 2.3f).

After the additional merging of mantle plumes, the total number of hot upwellings for the IND, SAP and EPR models with a rigid surface is 4, 7, and 7, respectively. We notice that these steady-state, hot upwellings are almost regularly distributed across the globe (Figs 2.3g, 2.3h, and 2.3i) i.e., a mean length of great circle between plumes is 10003 km (90°), 8804 km (79°), and 9318 km (84°) for the IND, EPR, and SAP R-simulations, respectively (Table 2.2). This demonstrates that rigid surface models probably try to establish a degree-4 convective pattern inside both the lithosphere and D"-layer which corresponds to the solutions of no-slip simulation based on the present-day tomography images (Glišović et al. (2012)).

However, ℓ=4 is not the absolute dominant long-wavelength for these models, because the mantle flow inside different layers is characterised by various spherical harmonic degrees. We first notice that degree-2 structure is established through the mantle adiabat for the IND-R model (Fig. 2.4a), while for the EPR-R simulation, some layers inside the upper part of the mantle and also the last 800 km depth are described by ℓ=5 formation of the mantle circulation (Fig. 2.4b). Models with the no-slip boundary condition develop a strong short-scale structure at the depths between 670 and 2000 km where the depth-dependent rheology used for this study (V2-profile, see Fig. 2.1b) increases by 2 orders of magnitude. The EPR-R and SAP-R simulations are characterised by ℓ=12-14 and ℓ=13, respectively (Figs 2.4b and 2.4c), while the IND-R and a rigid surface model initialised with the present-day tomographic image (here called TOMO model, Glišović et al. (2012)) develop a relatively strong satellite peak of the dominant convection wavelength around ℓ=12 and ℓ=8-14, respectively (Figs 2.4a and 2.4d).

Clearly, a steady-state solution to the direct problem of thermal convection in the mantle with a rigid surface is dependent on the starting lateral temperature variations (Fig. 2.3). Models with the no-slip boundary condition also emphasise the importance of depth-dependent rheol-

ogy. Yoshida & Kageyama (2006) have shown that the strong LVV only in combination with the depth-dependent rheology profiles can cause the dominance of long-wavelength structures of stagnant-lid convection ranging from ℓ=1 to ℓ=4. Using a constant spatial viscosity Schubert et al. (1990, 1997) have demonstrated that mantle flow with the no-slip boundary condition can be described by ℓ=1-3 structures. Also, many authors argue that the plume stability and longevity depend on the important rheological stabilisation associated with a high lower-mantle viscosity (e.g. Duncan & Richards (1991); Steinberger & O'Connell (1998); Lowman et al. (2008); Glišović et al. (2012)). Therefore, we should probably expect that different depth-dependent viscosity profiles can produce different long-wavelength structures of mantle convection, i.e., the dominant degree of mantle flow driven by a rigid surface is sensitive to the radial rheology profiles.

Another important characteristic of no-slip boundary models initialised by a theoretical temperature perturbation is that each starting thermal structure is preserved, and its geographical location is fixed during the evolution of mantle flow (see Fig. 2.3). A tomography based convection (TOMO) model with a rigid surface demonstrates a similar ability (Glišović et al. (2012). The TOMO model is able to reinforce some of the plume-like structures in the starting tomography, and then produce fixed and durable deep-mantle plumes. Also, this model reveals an interesting spatial relationship with the surface constellation hotspots and other manifestations of intra-plate volcanism (see Fig. 2.5).

The hot mantle plumes are theoretically expected (e.g. Morgan (1971)), and they occur in numerous laboratory and numerical experiments. A critical test of the plume hypothesis relies on direct observational evidence provided by the 3-D seismic mapping of the mantle structure beneath hotspots. The present-day 3-D tomographic images are able to distinguish two superplumes inside the D"-layer: one under the Pacific Hemisphere, and another under the mid-Atlantic ridge, South Africa, and the Antarctica plate (e.g. Zhao (2004); Simmons et al. (2009)). Zhao (2007) has done an analysis of whole-mantle tomographic images beneath 60 major hotspots on Earth suggesting about 12 whole-mantle plumes originating from the core-mantle boundary (CMB), ~ 5 upper-mantle plumes, and one mid-mantle plume. However, we should be careful with the interpretation of the seismic imaging, because Styles et al. (2011)

illustrated the importance of considering the dynamic plume shape, uncertainties in velocity-temperature sensitivity, and seismic resolution filtering in analysis of 3-D tomographic images.

Can we use a long-time scale convection model with a depth-dependent rheology to address which deep-mantle (super-)plume origin is most-likely resolved by the present-day tomography images? First, we know that the no-slip surface boundary condition coupled with the depth-dependent V2-viscosity profile probably tends to organise degree-4 mantle flow inside the lithosphere and D"-layer regardless of the initial buoyancy field, hence, some of the developed hot upwellings from the seismic images may be generated due to this effect of singular-plate on the mantle circulation. Second, and probably the most important, the initial temperature anomaly (Fig. 2.3) is preserved during the evolution of the rigid system; therefore, comparing the locations of starting and steady-state positive mantle heterogeneity may detect the origin of deep-mantle plumes in the present-day tomographic images, though this detection depends on the radial viscosity profile.

Fig. 2.5 shows possible candidates beneath the following present-day hotspots: Marqueses, Pitcairn, Easter, Galapagos, Marion, Crozet, Kerguelen, Reunion, Caroline, Cape Verde, and Ascension. But, if we compare these results to those obtained by the mobile surface plates (P-boundary condition) then a more complete answer to the previous question is possible.

2.5.2 Surface with tectonic plates coupled to the mantle flow

As in the case of models with a rigid surface, we also notice a peak in temporal variations of the CMB heat flux obtained by P-simulations between 200 and 300 Myr (Fig. 2.2b) that coincides with the appearance of numerous plumes at the depth of 220 km. From Fig. 2.6 we observe the clustering of plumes beneath some specific regions (e.g., the Eastern part of the North-American plate, the Southern parts of the African and Somalian plates, and Siberia) for all theoretical models (IND-P, EPR-P and SAP-P). This similarity in the geographical location of plumes during the period of the mantle flow initialisation is not surprising at all because Quéré & Forte (2006) have shown that plates play a key role in organising and modulating the large-scale cold downwellings in the deep mantle, and how these subduction zones are of crucial importance in understanding the production and location of hot thermal plumes in the

deep mantle. Such complementary dynamics of cold subducted material and hot upwellings can be also illustrated by the following results of this study.

The EPR-P model is initiated by the hot temperature anomaly inside the D"-layer beneath the equatorial part of the East Pacific Rise. At the depth of 220 km, this starting hot-upwelling is active 'only' between 185 and 215 Myr of model time, continuously moving eastward (Fig. 2.7a). The EPR plume is not stationary due to the impact of subducted cold material on the hot upwelling inside the D"-layer. The 'North' and 'South' subduction zones, mainly caused by the position of the starting positive temperature anomalies first shift the source of initial upwelling southward, and then separate the low-velocity mantle heterogeneity in two different parts, destroying the original signal of the EPR plume (Fig. 2.7b). However, due to the continuous organisation of convective flow, new mantle plumes are generated reaching the sub-lithosphere around 260 Ma, and one of them is located around the equatorial zone underneath the mid-Pacific Hemisphere (Fig. 2.6).

The newborn 'mid-Pacific' plume remains active inside a ~ 20° × 20° area at the depth of 220 km during the next 800 Myr (Fig. 2.7d). We also observe that the conduit of upwelling is stationary between 500 and 900 Ma. About 900 Ma, the 'East Pacific' cold superswell becomes very broad and much more intensive, continuing to push the plume more to the east (Fig. 2.7d). The upwelling remains in positions between 180°W and 150°E longitudes for almost 1.1 Gyr (Fig. 2.7e). During this time-window, 1.2-2.4 Ga, the hot thermal diapir takes the westernmost point (~ 150°E at t=1.6 Ga), and almost immediately the cold material arrives from ~ 70°E longitude pushing the plume back to the east (Fig. 2.7e). We also notice that the stability of upwellings can be compromised by the interaction of ascending hot material with the upper mantle or by the intensity of plume clustering in the lower mantle during some short time-windows, when the plume signal is lost in sub-lithosphere. This transient characteristic of hot thermal diapirs is much more detectable for other mantle plumes generated by theoretical models, as well as those obtained by a tomography based P-convection simulation (Glišović et al. (2012)). After 2.5 Ga the observed plume starts to migrate north-eastward, first, restoring its initial position around 3.1 Ga, and then, losing the equatorial signal about 3.7 Ga mostly because the east cold downwelling becomes very weak, and almost 'destroyed' by a new plume (Figs 2.7f and 2.7c).

A few results stand out from the evolution of the 'mid-Pacific' plume created by the EPR model with P-boundary condition. Once created and bounded by 'antipodal' subduction zones, the plume source can be tracked continuously over a very long period of time (~ 3.5 Gyr) that is comparable with the results obtained by a rigid surface. However, the plume conduit is not fixed to approximately the same position for more than ~ 400 Myr, in contrast to results for the no-slip surface models, but the activity of such deep-mantle plumes at sub-lithospheric depths is possible up to ~ 800 Myr inside a ~ $20° \times 20°$ region. These approximative life times are comparable to those obtained by a tomography based model with the surface tectonic plates (Glišović et al. (2012)) emphasising again the importance of the rheological stabilisation associated with a very-high lower-mantle viscosity peak inferred from geodynamic constraints (Forte & Mitrovica (2001); Mitrovica & Forte (2004)). Therefore, the deep-mantle plumes require no presence of a chemically stratified boundary layer to be stable and long-lived mantle structures, in contrast to suggestions by Davaille et al. (2002).

Even theoretical models with P-boundary condition demonstrate the ability of the convecting system to reinforce the dominant starting temperature anomaly such that this signal is transmitted to the upper or lower part of the mantle (Figs 2.6 and 2.7). Therefore, tracking the appearance of upwellings at sub-lithospheric depths obtained by the tomography-based models with the mobile surface plates can provide the missing piece of the puzzle for the question: which deep-mantle (super-)plume origin is most-likely resolved by the present-day seismic images and a specific depth-dependent viscosity? Glišović et al. (2012) have shown that the following hotspots: Pitcairn, Easter, Galapagos, Crozet, Kerguelen, Caroline and Cape Verde are detectable by a model with the P-boundary condition in the first 200, 300, 100, 400, 400, 100, and 400 Myr of model time, respectively. Other steady-state mantle plumes obtained by a rigid model (Marqueses, Marion, Reunion, Fernando, and Ascension) appear at sub-lithospheric depths after the first 100 or 200 Myr of model time for the P-convection model. Comparing results obtained by both P- and R-models based on the present-day tomographic image, we may suggest that the deep-mantle plumes resolved by the seismic tomography originate beneath the following present-day hotspots: Pitcairn, Easter, Galapagos, Crozet, Kerguelen, Caroline, and Cape Verde. It is interesting to note that only Crozet is not indicated with high probability to be a surface representation

of a deep-mantle plume based on the five different criteria of Courtillot et al. (2003).

Glišović et al. (2012) have also shown that models with surface plates coupled to the underlying mantle circulation are dominated by degree-1 structure during equilibrium. Therefore, we should probably expect to detect two antipodal hemispheres for models initialised by a randomly perturbed mantle heterogeneity. Indeed, the IND and EPR models with the P-boundary condition converge to the dominant degree-1 after ~2.0 and ~4.6 Gyr, respectively, while the SAP-P model is not able to deliver even after 5 Gyr the $\ell = 1$ thermal structure inside the upper part of the mantle and the lower TBL (Fig. 2.8). Also, the IND-P model is able to establish a system of dominant collision and subduction zones beneath Zagros, Himalayas, Indonesia (Java trench) and the Western part of the Pacific Hemisphere (Fig. 2.9b) that is similar to the results obtained by Glišović et al. (2012) using the present-day tomographic image as the initial mantle heterogeneity (Fig. 2.9a). There is also similarity between cold steady-state hemispheres for the SAP and EPR simulations, but with two important differences that lead to the inability of the SAP model to establish degree-1 structure inside some mantle layers (see Fig. 2.8). First, the inability of the SAP-P model to develop the strong system of Indonesia-Philippine-Bougainville trenches, contrary to the EPR and other P-simulations (Figs 2.9c, 2.9b, 2.9a). Second, the SAP model establishes the cold superswells at the location of the mid-Indian ridge (Fig. 2.9d), while the EPR simulation generates subduction beneath the Atlantic-Indian ridge (Fig. 2.9c), although we expect to observe no present-day downwellings at these locations. Therefore, the absence of cold downwelling structures at the locations of present-day Western Pacific trenches and Atlantic-Indian ridge causes the activity of subduction beneath the Nazca and Cocos plates to separate two hot regions beneath the southern and northern part of the South-American and Pacific plate, respectively.

Even with the obvious similarity in their steady-state (i.e. final) temperature distribution we note that P-models initialised by different mantle heterogeneity show distinct evolution.

2.6 Conclusions

Although an initial thermal structure is strongly imprinted on the future mantle evolution, the extent to which a starting mantle heterogeneity determines the final temperature distribution de-

pends on the surface boundary conditions. We have shown that a steady-state mantle-flow pattern obtained by a thermal convection simulation with a rigid surface is dependent on the starting mantle heterogeneity. Contrary to this case, a model with surface tectonic plates coupled to the mantle flow delivers a relatively similar final temperature distribution regardless of the initial buoyancy field. This is the direct consequence of the imposition of the present-day configuration of plate geometry. Also, a comparative analysis of steady-state upwellings obtained by the rigid surface model and the transient hot thermal diapirs reinforced by the mobile surface plates in the first few hundred million years, as well as their spatial connection to the present-day hotspots, can serve as an indicator of deep-mantle plumes resolved by seismic tomography (assuming a specific depth-dependent rheology). Using this approach on the previously obtained solutions of thermal convection by Glišović et al. (2012), we suggest that the tomography based (Simmons et al. (2009)) deep-mantle plumes are beneath the following present-day hotspots: Pitcairn, Easter, Galapagos, Crozet, Kerguelen, Caroline, and Cape Verde.

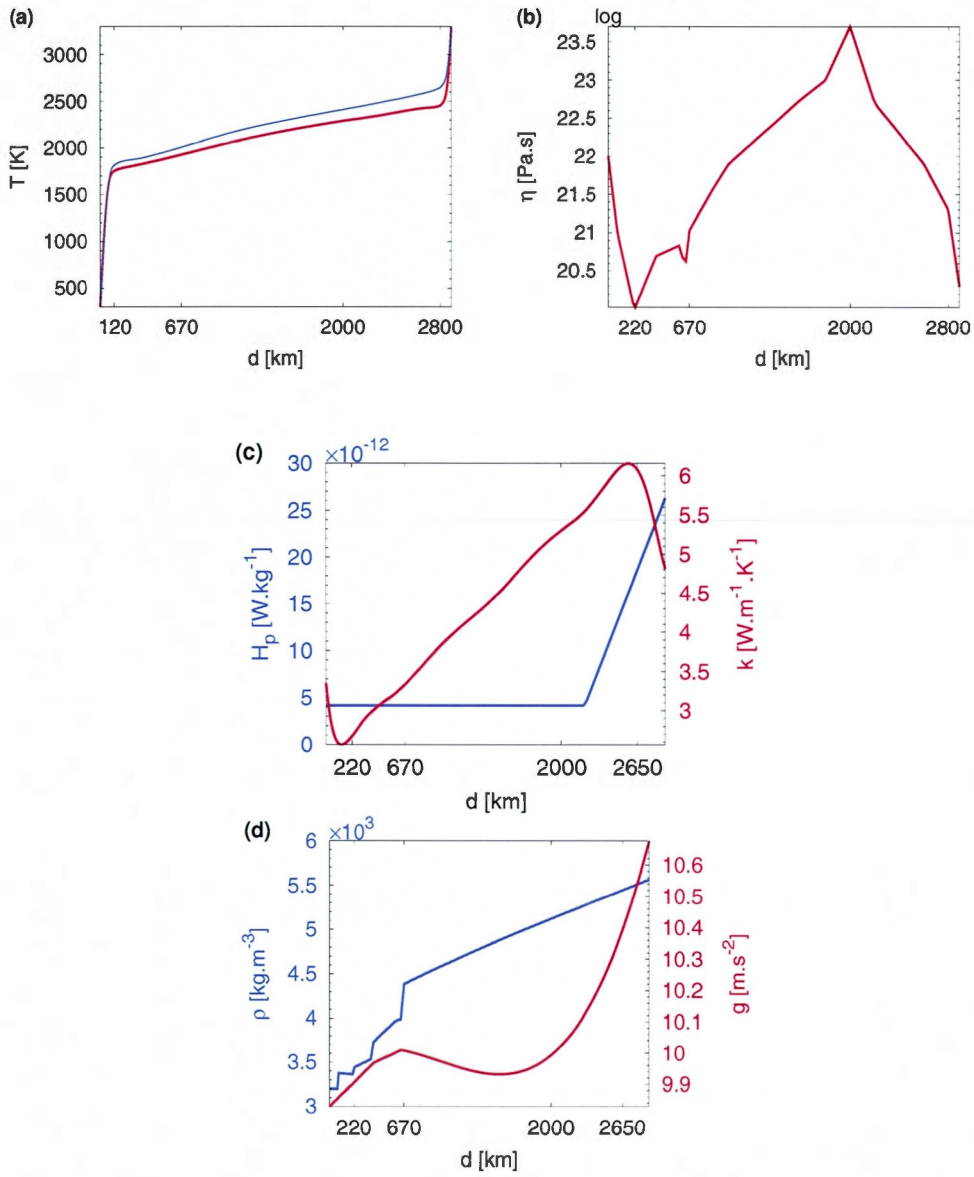

Figure 2.1: The initial horizontally-averaged temperature (i.e., geotherm) and the physical parameters as a function of depth (x-axis) which are used in this study. (a) The initial geotherms taken from a steady-state solution of the thermal convection in the mantle with different surface boundary conditions (Glišović et al. (2012)): a rigid surface (blue line) and the dynamically coupled plates (red line). (b) The viscosity profile V2 (Mitrovica & Forte (2004); Forte et al. (2010)). (c) The blue line represents the internal heating due to both the radiative isotopes and the secular cooling, and the red line shows the thermal conductivity profile (Hofmeister (1999)). (d) The density is shown by the blue line, while the red line represents the gravity profile (the PREM model of Dziewonski & Anderson (1981)).

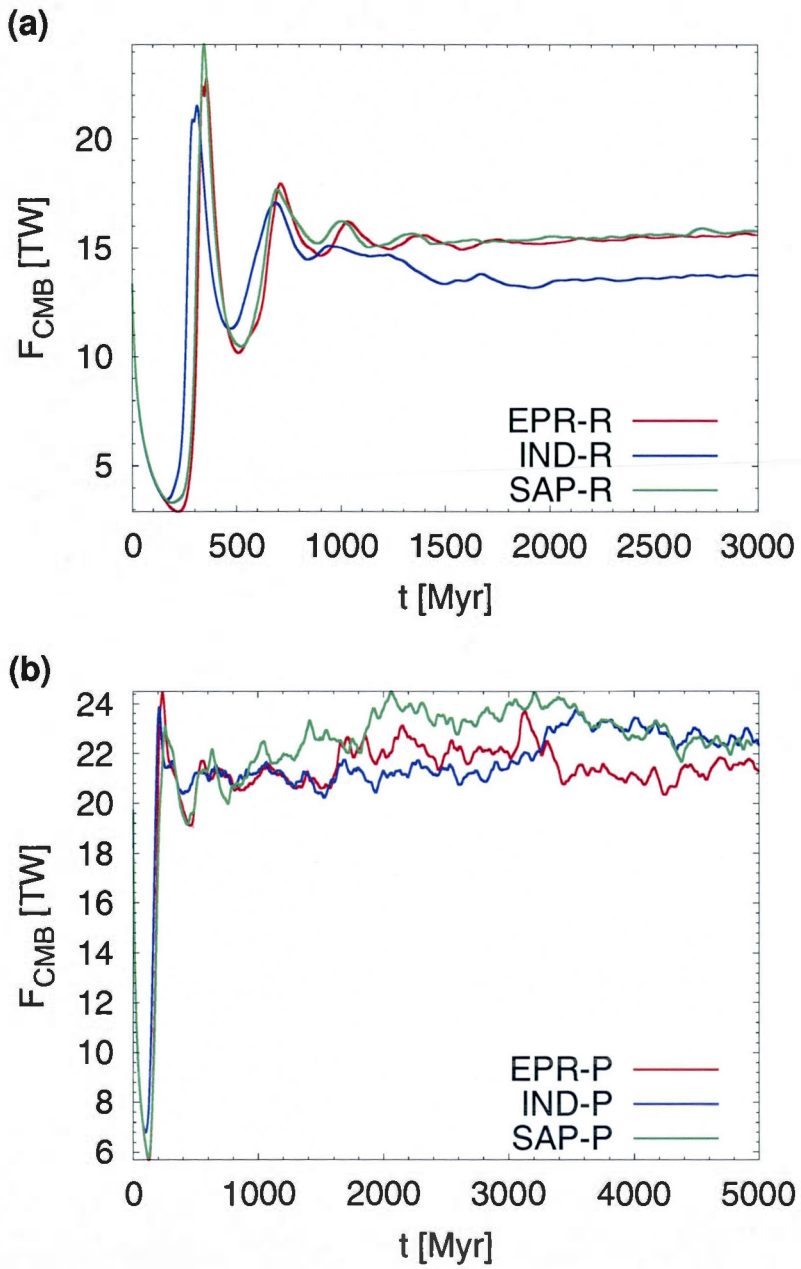

Figure 2.2: The CMB heat flux (y-axis) as a function of time (x-axis) obtained by: (a) a rigid surface (R-boundary condition) and (b) the surface tectonic plates coupled to the mantle flow (P-boundary condition).

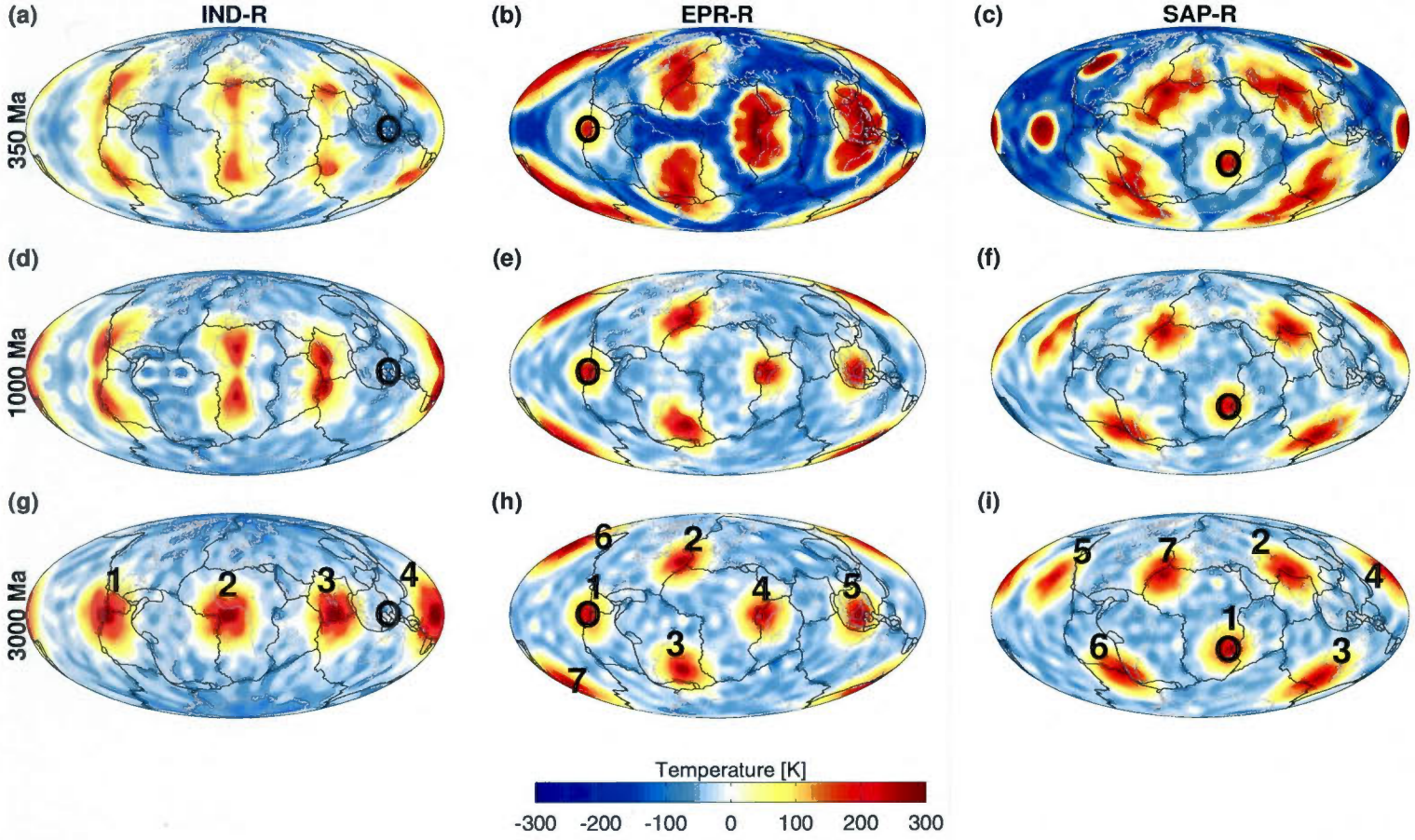

Figure 2.3: The maps show the lateral temperature variations (in Kelvin) at a depth of 220 km obtained by the IND, EPR, and SAP models with a rigid surface (given by columns) at the different points of time: 350, 1000, and 3000 Ma (given by rows). The black letter 'O' denotes the location of starting mantle heterogeneity, while the steady-state plumes are labelled by numbers (see Table 2.2).

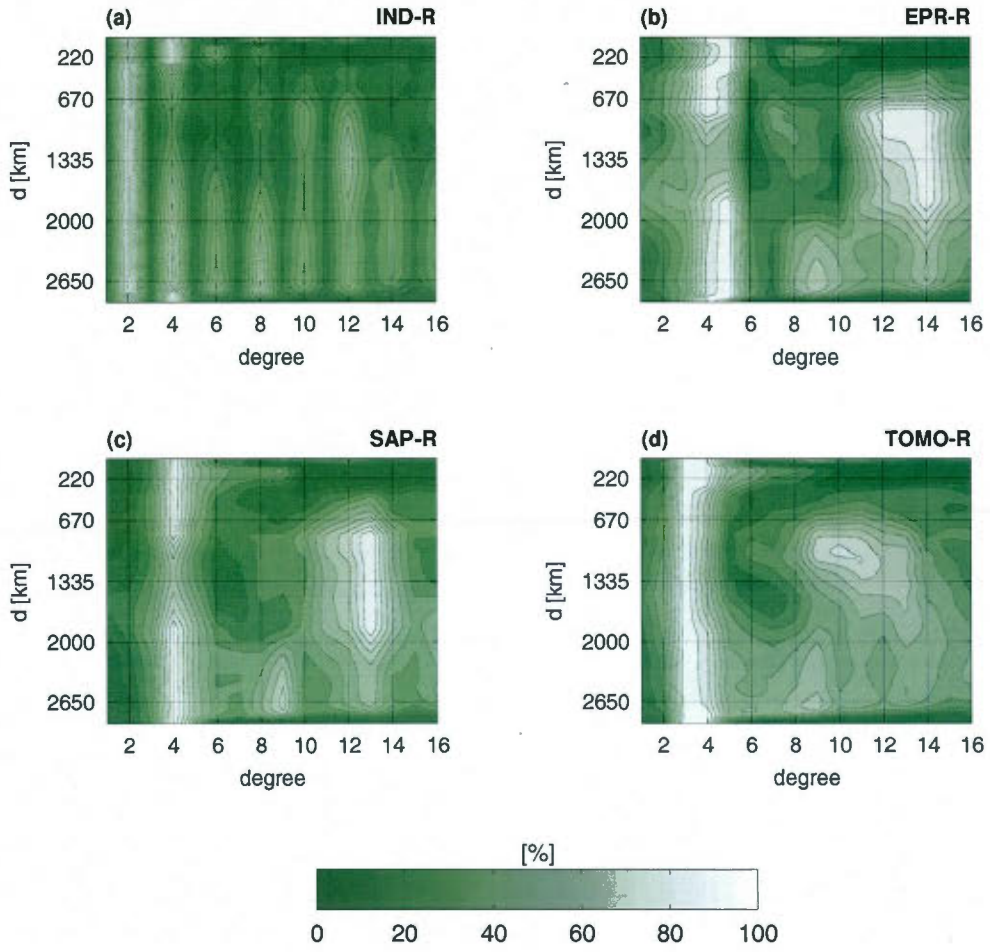

Figure 2.4: The percentage ratio between the amplitudes of the spherical harmonic degree (x-axis) and the dominant mode of convection as a function of depth (y-axis) for the (a) IND , (b) EPR, and (c) SAP simulations with the rigid surface at 3 Ga.

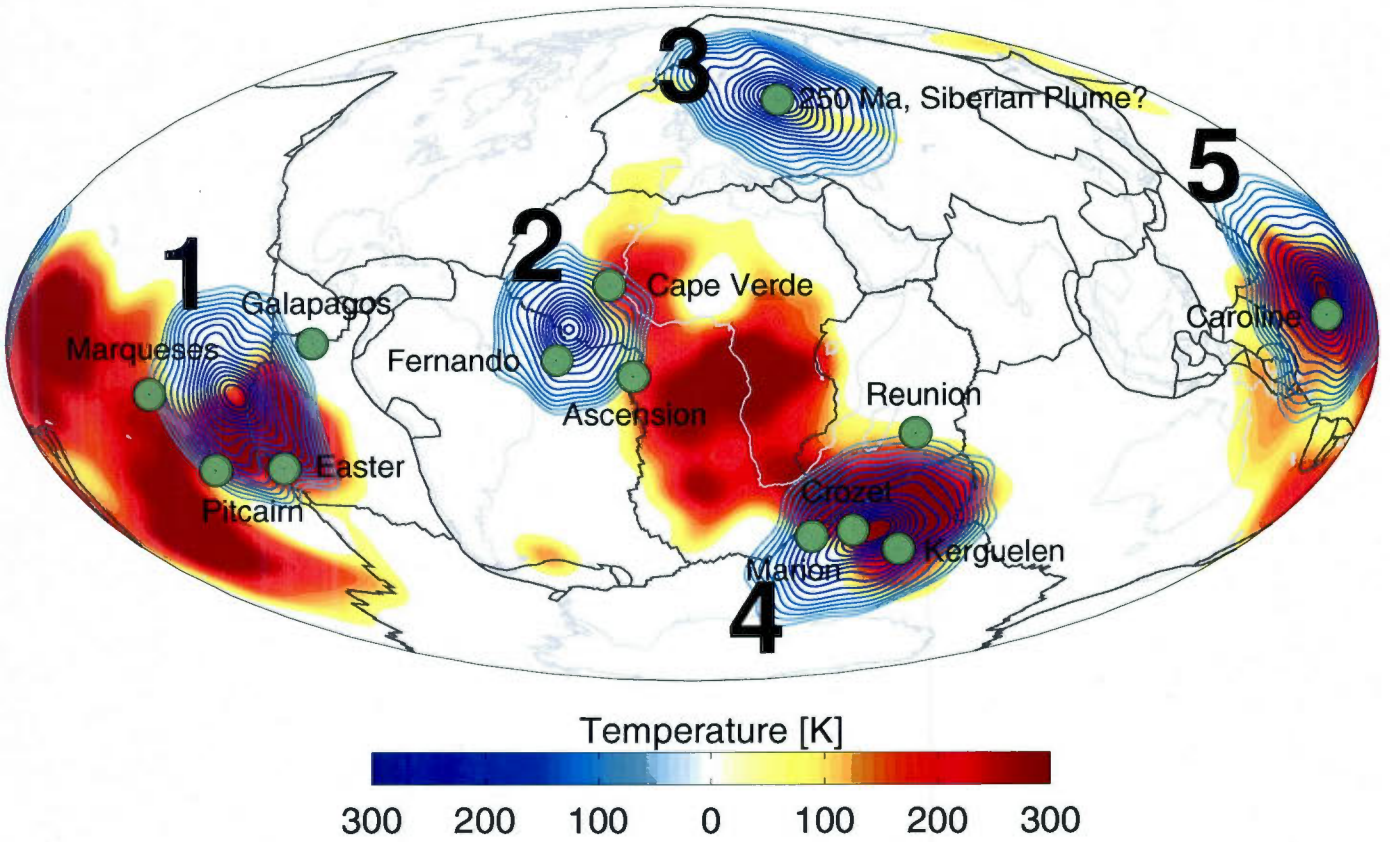

Figure 2.5: Map of positive temperature anomaly (red) determined by the present-day seismic image (Simmons et al. (2009)) at the depth of 2650 km superimposed by the filtered steady-state mantle heterogeneity ($100 \leq T \leq 300$ K, blue contour lines) at the depth of 220 km estimated by a reinforced rigid surface model (Glišović et al. (2012)) at 3 Ga. The green circles represent the location of some present-day hotspots (Courtillot et al. (2003)), while the steady-state plumes are labelled by numbers (see Table 2.2).

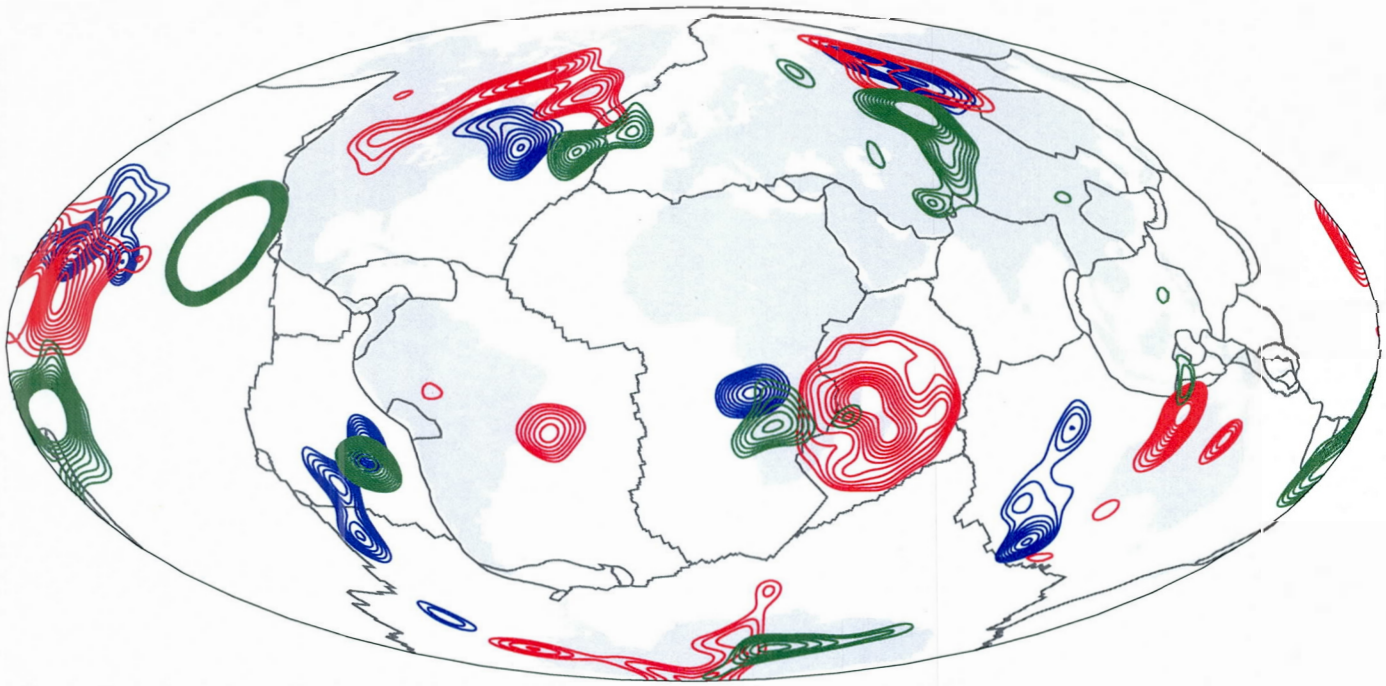

Figure 2.6: Map of positive mantle heterogeneity ($100 \leq T \leq 300$ K, contour lines) at the depth of 220 km obtained by the following simulations with the P-boundary condition (i.e., the mobile surface plates): (a) IND (blue), (b) EPR (red), and (c) SAP (green) at 260 Ma of model time.

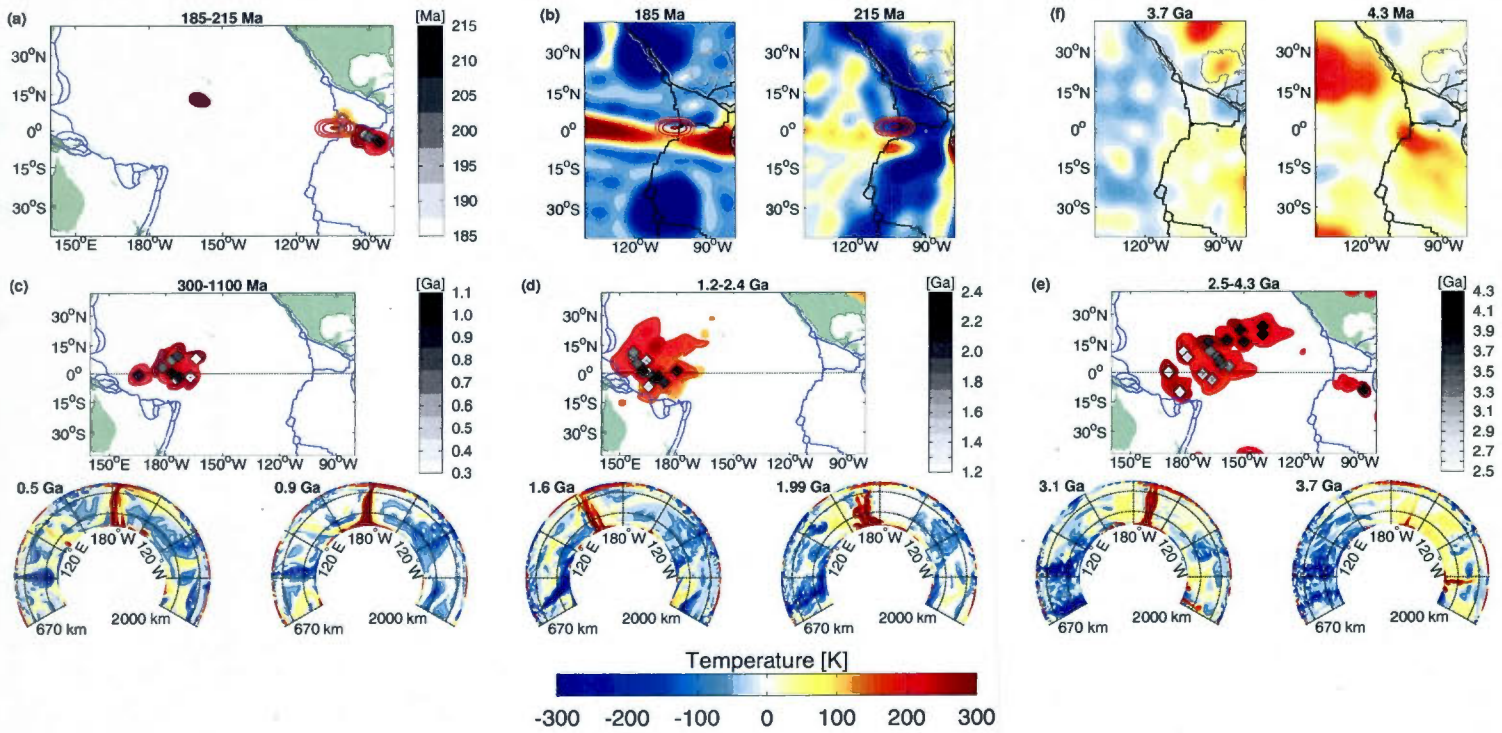

Figure 2.7: The evolution of mantle heterogeneity obtained by the EPR-P model beneath the Pacific plate from 185 Ma to 4.3 Ga. (a) Map of activity of the starting EPR plume at the depth of 220 km between 185-215 Myr. (b) Maps of mantle heterogeneity at 2650 km depth and 185 Ma (left) and 215 Ma (right) superimposed by the initial EPR plume (red contour lines) at the depth of 2850 km. The (c), (d), and (e) maps represent both the appearance of plumes ($100 \leq T \leq 300$ K) at the depth of 220 km during different time-windows: 300-1100 Ma, 1.2-2.4 Ga, and 2.5-4.3 Ga (top maps), and the equatorial cross-section of mantle heterogeneity at different points of time (two bottom maps). (f) The maps show the lateral temperature variations at 220 km depth, and 3.7 Ga (left) and 4.3 Ga (right) of model time. Diamonds indicate the locations of maximum plume temperature - the white represents maximum at the beginning of time-series which gradually decreases in brightness to the black at the end of observed interval (grayscale).

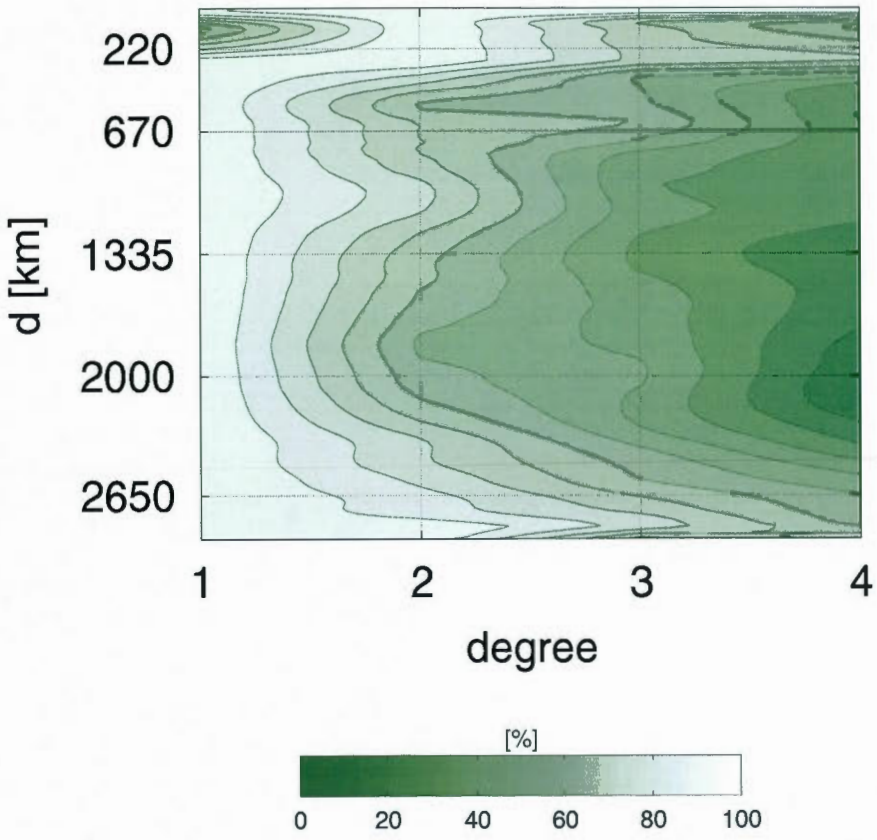

Figure 2.8: The percentage ratio between the amplitudes of the spherical harmonic degree (x-axis) and the dominant mode of convection as a function of depth (y-axis) for the SAP-P model (with the P-boundary condition) at 5 Ga.

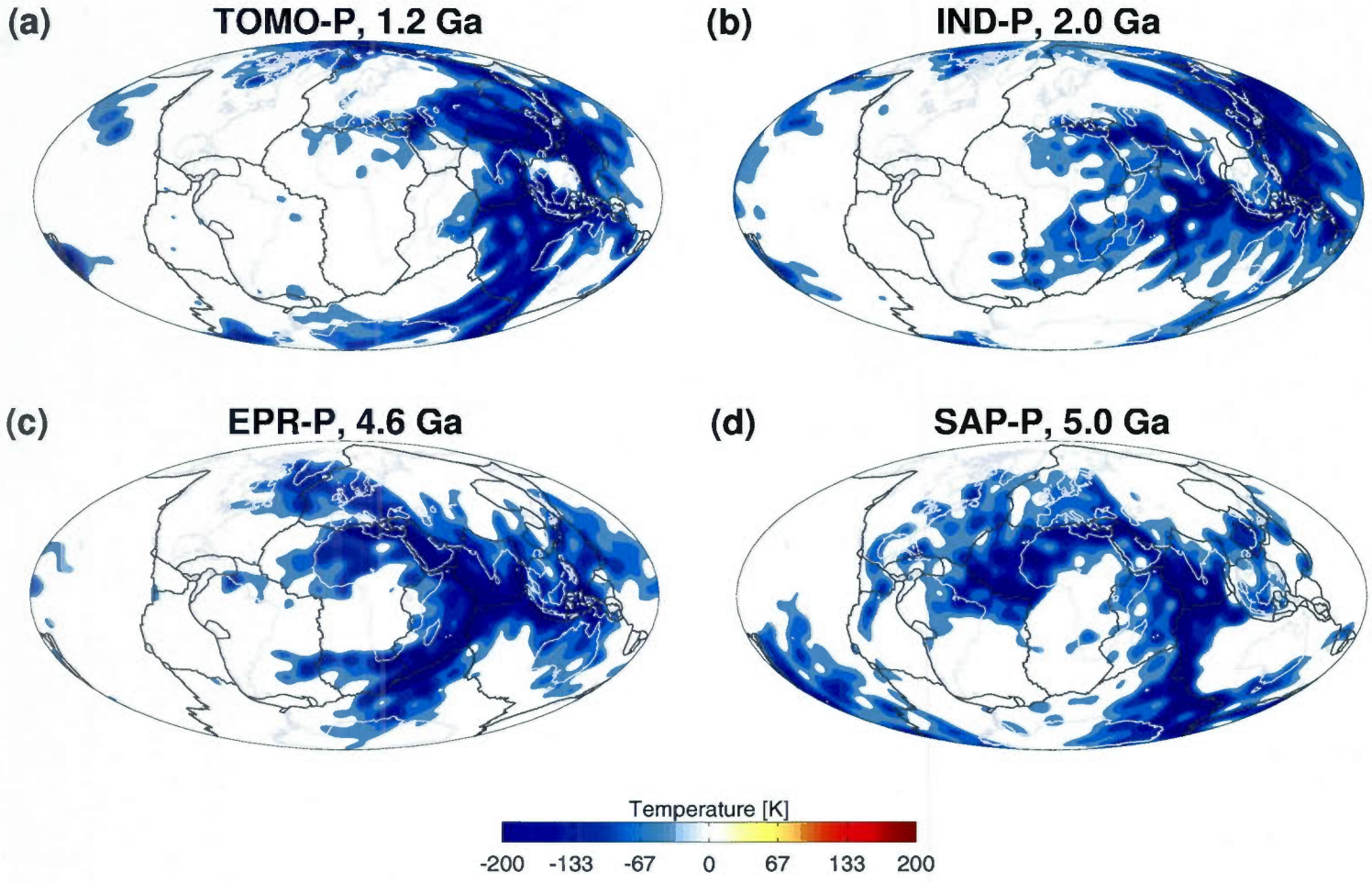

Figure 2.9: Maps of negative mantle heterogeneity (in Kelvin) at the depth of 220 km obtained by the TOMO (Glišović et al. (2012), IND, EPR, and SAP P-simulations (surface tectonic plates boundary condition) at different points in time: (a) 1.2 Ga, (b) 2.0 Ga, (c) 4.6 Ga, and (d) 5.0 Ga, respectively.

Table 2.1: Physical parameters and values employed in simulations of thermal convection of the mantle. Values in this table were kept constant in all simulations of thermal convection of the mantle.

Parameter	Value	Unit of Measure
Outer shell radius	6368	km
Inner shell radius	3480	km
Temperature (surface)	300	K
Temperature (CMB)	3300	K
Heat capacity c_p	1.25×10^3	$\mathrm{Jkg^{-1}K^{-1}}$
Thermal expansion α (surface)	3.5×10^{-5}	$\mathrm{K^{-1}}$
Thermal expansion α (670 km)	2.5×10^{-5}	$\mathrm{K^{-1}}$
Thermal expansion α (CMB)	1.0×10^{-5}	$\mathrm{K^{-1}}$

Table 2.2: The orthodromic distance between two plume maxima obtained by the IND, EPR, SAP and TOMO (Glišović et al. (2012)) models with the no-slip boundary condition at 3 Ga (see Fig. 2.3).

Model	Plume No.	Plume maximum (lon,lat)	Distance I pair	Distance I km (°)	Distance II pair	Distance II km (°)	Distance III pair	Distance III km (°)
IND-R	1	(104°W, 0°N)	(1,2)	10892 (98)				
	2	(6°W, 1°S)	(2,3)	9449 (85)				
	3	(79°E, 1°N)	(3,4)	10225 (92)				
	4	(171°E, 0°N)	(4,1)	9447 (85)				
			σ_{tot}	10003 (90)				
EPR-R	1	(104°W, 0°N)	(1,2)	8236 (74)	(6,7)	9669 (87)	(2,4)	8551 (77)
	2	(36°W, 43°N)	(1,3)	8314 (75)	(2,3)	9559 (86)	(3,4)	8472 (76)
	3	(35°W, 43°S)	(1,6)	8420 (76)	(6,2)	9475 (85)	(4,5)	8780 (79)
	4	(36°E, 0°N)	(1,7)	8393 (76)	(7,3)	9611 (86)	(5,6)	8498 (76)
	5	(115°E, 0°N)					(5,7)	8472 (76)
	6	(174°W, 44°N)	σ_1	8341 (75)	σ_2	9579 (86)	σ_3	8555 (77)
	7	(174°W, 43°S)	σ_{tot}	8804 (79)				
SAP-R	1	(24°E, 28°S)	(1,6)	8968 (81)	(7,6)	9798 (88)	(4,2)	9354 (84)
	2	(80°E, 33°N)	(1,7)	8915 (80)	(2,7)	9862 (89)	(4,3)	9079 (82)
	3	(131°E, 45°S)	(1,2)	8990 (81)	(3,2)	10079 (91)	(5,6)	9146 (82)
	4	(179°E, 24°N)	(1,3)	9048 (81)	(6,3)	9622 (87)	(5,7)	9256 (83)
	5	(130°W, 25°N)						
	6	(81°W, 44°S)	σ_1	8980 (81)	σ_2	9840 (89)	σ_3	9209 (83)
	7	(32°W, 32°N)	σ_{tot}	9318 (84)				
TOMO-R	1	(114°W, 11°S)	(1,2)	9522 (86)				
	2	(29°W, 3°N)	(2,3)	8391 (75)				
	3	(36°E, 61°N)	(2,4)	9925 (89)				
	4	(57°E, 45°S)	(3,5)	11013 (99)				
	5	(164°E, 9°N)	(4,5)	12042 (108)				
			(5,1)	9332 (84)				
			(3,4)	11932 (107)				
			σ_{tot}	10308 (93)				

CHAPTER III

TIME-REVERSED MANTLE CONVECTION BASED ON THE 3-D TOMOGRAPHIC IMAGES: QUANTIFYING ROBUSTNESS OF THE QRV AND BAD MODELS OVER THE CENOZOIC ERA

Submitted to *Earth and Planetary Science Letters* (2012).

3.1 Résumé

Le manque de connaissance des conditions initiales dans le passé géologique pour l'évolution de la convection mantellique est un problème fondamental en suspens. Une préoccupation majeure est donc le développement des reconstitutions de l'évolution 3-D du manteau qui ont maximum de compatibilité avec une large suite de contraintes géophysiques. La quantification de la robustesse des modèles de convection inversées dans le temps est une autre question importante. Afin de résoudre et estimer la robustesse du problème inverse de la convection dans le manteau, nous considérons et comparons deux différentes techniques numériques actuellement utilisées dans la modélisation de la convection inversée dans le temps: les méthodes de quasi-réversibilité (QRV) et de l'advection vers l'arrière (BAD), sur un intervalle de temps de 65 millions d'années. Pour réaliser cet objectif nous utiliserons un modèle pseudo-spectrale de convection que nous avons développé en géométrie 3-D sphérique, dans un manteau dissipatif et compressible. Nous avons défini un nouveau paramètre de régularisation pour la méthode QRV qui varie dans le temps, et nous avons quantifié la robustesse au cours de l'ère cénozoïque en termes des incerti-

tudes suivantes : [7 à 29]%, [11 à 37]%, [8 à 33]% et [6 à 9]% pour la divergence des plaques tectoniques, les anomalies de gravité à l'air libre, la topographie dynamique de surface, et la topographie dynamique à la limite noyau-manteau, respectivement. Les questions dominantes pour le problème inverse de la convection mantellique sont le choix d'un profil de température moyenne (le géotherme) et les conditions aux limites à la surface : soit avec des plaques mobiles, soit avec une de surface rigide. Toutefois, l'impact critique sur la reconstruction de l'évolution du manteau dépend de l'interaction entre le géotherme et les variations latérales de température dans les couches limites thermiques. Les modèles QRV initialisés par une solution convective en état d'équilibre sont en mesure d'obtenir une reconstruction très robuste de la température du manteau (avec incertitudes < 10%) pour tout type de géotherme et de conditions aux limites de surface.

3.2 Abstract

The lack of knowledge of initial conditions for mantle convection at some point in the geological past is an outstanding problem. A key concern is developing reconstructions of 3-D mantle evolution that have maximum consistency with a wide suite of geophysical constraints. Quantifying the robustness of time-reversed convection models is another important issue. To solve and estimate the robustness of the inverse problem of mantle convection, we consider and compare two different numerical techniques currently used in backward convection modelling: the quasi-reversibility (QRV) and the backward advection (BAD) methods over a 65 Myr interval using a dissipative and compressible pseudo-spectral approach in 3-D spherical geometry. We have defined a new regularization parameter for the QRV method as a time-dependent function quantifying the range of uncertainties $[7, 29]\%$, $[11, 37]\%$, $[8, 33]\%$ and $[6, 9]\%$ for the surface divergence, the free-air gravity anomalies, the dynamic surface and core-mantle boundary topography, respectively, over the Cenozoic era. The dominant issues for the inverse problem of mantle flow are the choice of a horizontally-averaged temperature (i.e. geotherm) and the adopted surface boundary condition (mobile surface plates or a rigid surface). However, the system ability to create stable thermal boundary layers has a critical impact on the reconstruction of mantle evolution. The QRV models initialized by a steady-state solution are able to

obtain a very robust reconstruction of mantle temperature (uncertainties < 10%) for any type of geotherm and surface boundary condition.

3.3 Introduction

The first efforts to infer the time-dependent changes in lateral heterogeneity in the mantle were based on estimated trajectories of subducted slabs derived from reconstructions of Mesozoic and Cenozoic plate histories (Richards & Engebretson (1992); Ricard et al. (1993)). Although such models of subducted slab heterogeneity have been useful (e.g. Richards et al. (1997), Lithgow-Bertelloni & Richards (1998)), they remain essentially kinematic to the extent that the slabs are not advected self-consistently on the basis of the mantle flow field. In addition, the slab models do not account for the presence and evolution of hot thermal plumes in the mantle which have been imaged by global seismic tomography (e.g. Forte et al. (2010)). These difficulties have motivated an alternative approach in which the past evolution of mantle heterogeneity is estimated on the basis of present-day temperature anomalies derived from seismic tomography and subsequently time-reversing the full set of convective field equations (Forte & Mitrovica (1997); Steinberger & O'Connell (1997); Conrad & Gurnis (2003); Bunge et al. (2003)). This alternative approach will be exploited in this study using the tomography-based convection model developed below.

Recent developments in seismic tomography (e.g. Simmons et al. (2009)) allow the geodynamically constrained mapping of mantle thermal heterogeneity. Lateral variations of the Earth's mantle obtained in this manner represent the present-day observation and the starting point to predict or reconstruct thermal evolution of the Earth's mantle by convection processes. The former is the direct problem characterized by problems of existence, uniqueness and stability of a solution, contrary to the reconstruction which belongs to time-reversed (inverse) problems. In other words, we are unable to naturally model thermal convection backward in time because of thermal diffusion and viscous dissipation both of which are irreversible. Despite this fact, there are a few advanced numerical techniques for solving this problem.

One of them is data assimilation that can be defined as the incorporation of present (observations) and past data (initial conditions) in an explicit dynamic model to provide continuity

and coupling among the physical fields (e.g. velocity and temperature). The basic principle of data assimilation is to find the initial condition in order to minimize the discrepancy between the observations and the initial conditions of the model. In the recent treatments of the inverse problem for mantle convection there are two particular data assimilation methods: sequential (Bunge et al. (2002)) and four-dimensional variational (4-D Var) data assimilation (e.g. Bunge et al. (2003), Ismail-Zadeh et al. (2004)).

Ismail-Zadeh et al. (2007) used the quasi-reversibility (QRV) method to solve the backward mantle convection problem. The use of QRV method implies the introduction into the backward heat equation of an additional term involving the product of a small regularization parameter and a higher order temperature derivative allowing additional boundary conditions. The data assimilation in this case is based on a search of the best fit between the forecast model state and the observations by minimizing the regularization parameter. The accuracy of the QRV data assimilation is lower than that of the 4-D Var, but the QRV method does not require any additional smoothing of the input data or filtering of temperature noise as the 4-D Var method does (Ismail-Zadeh et al. (2007)). Based on the results and the comparison of the methods, we consider the QRV method to be a highly promising approach to assimilation of data related to mantle dynamics, and it will be tested in the work presented here.

Besides data assimilation techniques there is a method that ignores the diffusivity and dissipation term in the equation of energy if the interior of the convective region is characterized by a high Rayleigh number. This method is often called the BAD method because it performs only the advection term backward in time, and it will be used to estimate the past initial conditions of temperature in this study.

Our ultimate goal is to reconstruct the Cenozoic era addressing uncertainties using both the QRV and BAD methods. The Cenozoic era is significant from a wide spectra of geodynamical manifestation of the mantle flow. From a tectonic perspective, in the last 65 Myr of Earth's evolution the continents moved into their current positions. Among other tectonic events during this period, the Atlantic Ocean widened, and India collided with Asia around 55 Ma. Based on data from marine magnetic profiles, the rapid India plate motion begins at the same time as the first pulse of Deccan flood basalts, which is dated at 67 Ma. This correlation is probably driven

by the push force of the Reunion plume head (Cande & Stegman (2011)).

Equally important evidence for deep mantle circulation comes from paleomagnetic observations of so-called 'True Polar Wander' (TPW), defined with respect to some global reference frame, e.g. hotspots or no-net lithospheric rotation. TPW is often taken to represent motion of the rotation axis with respect to the deep mantle (Jurdy (1981)) arising from changes in Earth's inertia tensor in response to large-scale reorganizations of mantle density anomalies (Ricard et al. (1992)). Recent analysis of uncertainties in the amplitude of TPW throughout the Cenozoic era suggest the past inferences (e.g. Courtillot & Besse (1987)) have significantly over-estimated the magnitudes of TPW. This suggests that the mantle-convective origin of TPW continues to be an outstanding problem in geodynamics.

The motion of the Solar System is chaotic to the extent that the precise positions of the planets are predictable for a period of only about 20 Myr (Laskar (1990)). The Earth's precession, obliquity and insolation parameters over this time period can be influenced by secular variations in the dynamic ellipticity of the planet which are driven by long-term geophysical processes, such as post-glacial rebound. Forte & Mitrovica (1997) investigated the influence of mantle convection on these parameters. Once determined, these parameters can be used for studying Milanković orbital theory of climate change and for re-calibrating Cenozoic time-scales.

While these examples illustrate the influence of mantle convection on the evolution of our planet, they also demonstrate clearly that we cannot hope to investigate these events without a better knowledge of the temporal character of mantle flow.

The numerical modelling of the backward mantle flow is briefly summarized as follows. First, we outline the basic hydrodynamic theory relevant to this study, followed by a presentation of the numerical implementation of the pseudo-spectral method for integrating both the direct and inverse governing field equations, respectively. We then discuss the reference frame and initial conditions used in this study. We next present a number of tests designed to estimate the uncertainties of the pseudo-spectral approach for the QRV and BAD methods. The main objective is to determine the influence of initial conditions and the horizontally-averaged temperature on reconstructions of thermal structure of the mantle. We conclude with a discussion of the main results and limitations of tomography-based time-reversed mantle convection models

presented in this study.

3.4 Numerical Method

We employ the numerical model of thermal convection based on standard hydrodynamic equations describing principles of conservation of mass, momentum and energy for a Newtonian fluid (e.g., Landau & Lifshitz (1959)):

$$\frac{\partial \rho}{\partial t} + \nabla \cdot (\rho \mathbf{u}) = 0 \tag{3.1}$$

$$\rho \frac{d\mathbf{u}}{dt} = \nabla \cdot \boldsymbol{\sigma} + \rho \mathbf{g} \tag{3.2}$$

$$\rho c_p \frac{\partial T}{\partial t} = -\rho c_p \mathbf{u} \cdot \nabla T + \nabla \cdot k \nabla T + \alpha T \frac{dp}{dt} + \Phi + Q \tag{3.3}$$

in which thermodynamical variables are the (absolute) temperature T, the pressure p, the specific heat c_p, the thermal conductivity k and the thermal expansion α, while other variables are the velocity field $\mathbf{u}$, the stress tensor $\boldsymbol{\sigma}$, the gravitational acceleration $\mathbf{g}$ and the density ρ. The body force term $\rho \mathbf{g}$ in the conservation of momentum equation (3.2) describes the buoyancy forces due to variations of temperature which drive the mantle flow. The equation of energy conservation (3.3) is constituted by the following terms: $\mathbf{u} \cdot \nabla T$ is the advection of temperature, $\nabla \cdot k \nabla T$ is the diffusion, Φ is the dissipation due to internal viscous friction, $\alpha T \frac{dp}{dt}$ is the work associated with adiabatic changes of volume, and the last term Q is the internal heating rate per unit volume of fluid. Here we present only equations governing the pseudo-spectral approach of thermal convection; for more details see Glišović et al. (2012).

It is well-known that a backward time-integration of the energy equation (3.3) is an ill-posed problem because of the existence of viscous dissipation and thermal diffusion, which are both irreversible terms. One of the proposed numerical methods to transform this ill-posed problem into a well-posed problem is the quasi-reversibility (QRV) method (e.g, Lattes & Lions (1969), Ismail-Zadeh et al. (2007)). The QRV method construction is simple, and involves the product of a small regularization parameter (β), and a high-order temperature derivative in the energy equation (3.3) introducing additional boundary conditions (3.29). The quasi-reversibility term

is related to diffusion in a 'classical' approach, but here we will consider the existence of a dissipation term in the regularized equation of energy. This equation has the following form

$$\rho c_p \frac{\partial T}{\partial t} + \beta \Lambda\left(\frac{\partial T}{\partial t}\right) = \rho c_p \mathbf{u} \cdot \nabla T - \nabla \cdot k \nabla T - \alpha T \frac{dp}{dt} - \Phi - Q \tag{3.4}$$

where β is a small regularization parameter and $\Lambda\left(\frac{\partial T}{\partial t}\right)$ is the biharmonic diffusion operator (see Appendix 3.A). The approximate solution of the regularized backward conservation energy problem is stable for $\beta > 0$ and it converges to the solution of the forward conservation energy problem, in some spaces, where the conditions of well-posedness are met (Samarskii et al. (2004)).

In order to derive an equation for the backward advection (BAD) method, eq.(3.3) may be rewritten in terms of the surface Rayleigh number Ra_s (for more details, see Glišović et al. (2012)),

$$\frac{\partial T}{\partial t} = -\mathbf{u} \cdot \nabla T + \frac{1}{\rho Ra_s}\left(\nabla \cdot k \nabla T + Q\right) + \frac{Di}{\rho}\left(-\alpha T \frac{dp}{dt} + \Phi\right) \tag{3.5}$$

where Di is the dissipation number (Peltier (1972)) which measures the importance of compressional work and frictional heating. If we assume that the mantle flow is characterized by high Rayleigh number, then we may neglect the diffusion and internal heating term inside the energy equation (3.5). The dissipation term is small and thus may be empirically neglected. After these simplifications, and inverting the sign of the advection term, eq.(3.3) becomes the simple backward advection equation

$$\frac{\partial T}{\partial t} = \mathbf{u} \cdot \nabla T \tag{3.6}$$

which will be the base for our second approach (the BAD method) in the reconstruction of mantle flow.

3.5 Description of Models

3.5.1 Reference Properties of the Mantle

We use a radial viscosity (V2) profile (Fig. 3.1) constrained by global joint inversion of convection-related surface observables (Forte et al. (2010)) and data associated with the response of the Earth to ice-age surface mass loading (Mitrovica & Forte (2004)).

The radial density profile $\rho_0(r)$ which describes the reference hydrostatic state in our compressible convection model is taken directly from the seismic reference Earth model PREM (Dziewonski & Anderson (1981)). The corresponding radial gravity field $g_0(r)$ is obtained by the integration of $\rho_0(r)$.

In this study we employ a thermal conductivity profile given by Hofmeister (1999) that considers the effect of thermal boundary layers (TBLs) inside the mantle and the possibility that thermal conductivity decreases with depth across both layers (Fig. 3.1).

Also, we use a constant heat capacity $c_p = 1.25 \times 10^3$ $\mathrm{Jkg^{-1}K^{-1}}$, while the coefficient of thermal expansion, $\alpha(r)$, is assumed to vary linearly from a value of 3.5×10^{-5} $\mathrm{K^{-1}}$ at the top of the mantle to a value of 2.5×10^{-5} $\mathrm{K^{-1}}$ at 670 km depth (Stacey (1998), Jackson (1998)), decreasing to 1.0×10^{-5} $\mathrm{K^{-1}}$ at the CMB.

We employ a total value of internal heating that is the sum of two components: radioactive sources (12 TW) and estimated secular cooling (12 TW).

3.5.2 Initial Conditions

We use two types of boundary conditions for modelling thermal convection flow in the mantle: rigid surface (R) and surface tectonic plates (P). The P-boundary condition involves the reconstructed geometry of the major tectonic plates over the past 57.5 Myr and modelling the plate-coupling to mantle flow is carried out in the no-net rotation reference frame. One important difference between them is that the P-boundary condition involves the generation of toroidal flow via the surface-plate rotations and this is not the case in either of the two other boundary conditions: the rigid surface or free-slip (F). Also, the coupling of surface plates employing the P-boundary condition requires a consideration of both rigid and free-slip flow

kernels and hence this condition is, in a sense, intermediate between the R- and F-boundary conditions (e.g. Glišović et al. (2012)).

The present-day tomographic model (Simmons et al. (2009)) is not a perfect representation of the Earth's mantle heterogeneity despite fits of 93%, 92%, 99% and 82% to seismic, gravity, divergence and topography data, respectively. In particular the seismic image of the Earth's interior does not carry information about a gradient slope of TBLs, because seismic amplitudes are more or less equal through them. This is an impassable obstacle for the QRV method which generates numerical instabilities from the start of backward integration. Therefore, the initial seismic image must be altered. One of the recommended solutions considers the smoothing of present-day mantle heterogeneity by diffusion over a very short time-window. Such a procedure introduces information on the TBLs' existence to the starting tomographic image. In order to justify this smoothing technique, we diffused the present-day tomographic image over the 1 Myr time interval (29 time steps) making a new initial internal loading state that preserves about 98% of the original convection-related observables.

Information about the slope of TBLs is introduced to the system by the horizontally-averaged temperature profile i.e. the geotherm. The choice of geotherm has a critical impact on the evolution of Earth's thermal structure. The system, a modified present-day seismic image plus an 'Earth-like' geotherm with two boundary layers, is far from the state of equilibrium. This system is in a transient period, especially over the first 65 Myr of evolution, and the level of integration between mantle heterogeneities and the geotherm inside the TBLs is very low. In other words, during this period, subduction and plumes will be reinforced, increasing the amplitude of lateral variations in temperature inside the TBLs (Glišović et al. (2012)). To address this difficulty we created two separate classes of models for both boundary conditions: the SS-class that covers steady-state solutions over a 65 Myr interval, and the CE-class over the Cenozoic era (from the present-day to 65 Ma).

The SS-class is initialized by the steady-state mantle temperature field at 3.4 Ga for the P-boundary condition, and at 2 Ga for the rigid surface (Glišović et al. (2012)). Similar to the SS-class, we designed two models for the CE-class depending on the type of surface boundary condition, CE-R and CE-P, respectively. For the CE-R model we use a steady state 'Earth-like'

geotherm which produces 37 TW at the top of the mantle and 13 TW at the CMB. The CE-P model is initialized by the energy balanced 2BL-geotherm generating 44 TW at the surface and 20 TW at the bottom of the mantle. The 2BL-geotherm is characterized with T_{surf} = 300 K and T_{cmb} = 3300 K. Both CE-models are initialized using the present-day 3-D mantle heterogeneities that were previously diffused over the 1 Myr interval. The adiabatic (A) geotherm does not provide information about TBLs, so among other simulations it must be used for the BAD simulations. The A-geotherm is characterized by ΔT = 885 K, i.e. T_{surf} = 1700 K and T_{cmb} = 2585 K.

To quantify uncertainties for both the QRV and BAD solutions, we use two different data-assimilation algorithms depending of the class type. For the SS-class of models we define the following algorithm:

1. Solve the direct problem of mantle flow in N time samples over a 65 Myr interval.
2. Take the Nth-solution as a new initial temperature field, and perform one of the proposed inverse methods over a 65 Myr time-window. For the QRV method we tested a number of various values for the β-parameter.
3. Compare the forward and backward sequence of solutions at the same points in time, calculating errors in the heat flux and the convection-related (geodynamical) observations: the dynamic surface and CMB topography, the free-air gravity anomalies and the horizontal divergence of the tectonic plates.

The CE-algorithm is slightly different to the SS one, and can be described by the following steps:

1. Solve the inverse problem of thermal convection in the mantle for N time samples over the Cenozoic era using the BAD and QRV methods.
2. Take a solution at 65 Ma as a new internal loading state and then perform a forward integration up to the present-day.
3. Same as the final step of the SS-class algorithm, but without the calculation of uncertainties in the heat flux.

The uncertainty of the inverse (I) model may be expressed by the formula for the total root-mean square (rms) error:

$$Err(I) = \sqrt{\sum_{\ell=0}^{L} \frac{\mathcal{D}_\ell^0 \overline{\mathcal{D}}_\ell^0 + 2\sum_{m=1}^{\ell} \mathcal{D}_\ell^m \overline{\mathcal{D}}_\ell^m}{\mathcal{P}_\ell^0 \overline{\mathcal{P}}_\ell^0 + 2\sum_{m=1}^{\ell} \mathcal{P}_\ell^m \overline{\mathcal{P}}_\ell^m}} \cdot 100\,\% \tag{3.7}$$

where L is a maximum of spherical harmonic degree, and $\mathcal{D}$ is the difference between a predicted ($\mathcal{P}$) and reconstructed ($\mathcal{R}$) geodynamical solution, while $\overline{\mathcal{D}}$ and $\overline{\mathcal{P}}$ represent their complex conjugates. Similar to this formula, we may calculate the heat flux uncertainties using simple relative error:

$$Err(F) = \frac{F_{\mathcal{R}} - F_{\mathcal{P}}}{F_{\mathcal{P}}} \cdot 100\,\% \tag{3.8}$$

where $F_{\mathcal{R}}$ and $F_{\mathcal{P}}$ are the reconstructed and predicted heat flux, respectively.

3.6 Results

3.6.1 Reconstruction of Steady-State Solution over 65 Myr Interval

We tested three different β-parameterisations for the SS-P and SS-R models (Fig. 3.2). Two of them are constant during the inverse integration ($\beta_1 = 1 \times 10^{-7}$ and $\beta_2 = 1 \times 10^{-10}$), while the third one is given as a function of dimensionless time

$$\beta(t) = \beta_0 t \tag{3.9}$$

where $\beta_0 = 1 \times 10^{-13}$ for the SS-class.

From Fig. 3.3 we notice that the most accurate reconstruction of mantle heterogeneities for both boundary surface conditions is achieved using both the time-varying β-function (eq. 3.9) and $\beta_2 = 1 \times 10^{-10}$ - in this case uncertainties are $\leq 10\%$.

The BAD method for the P-boundary condition is able to keep the uncertainty in free-air anomalies, the surface topography and divergence below 10% for 10 Myr time-windows (Figs 3.3a, e and g). An approximation of reconstructed CMB topography (Fig. 3.3c) extends the valid 10%-interval to 30 Ma. The BAD model with the rigid surface establishes the end

of 10%-interval around 25 Ma for the CMB and surface topography, while the uncertainty of gravity anomalies is lower than 10% only for the first 10 Myr, as for the P-boundary condition case (Figs 3.3b, d and f).

We also examined the effect of higher horizontal discretization on the QRV solutions by increasing the maximum spherical harmonic degree from 32 to 64. From Fig. 3.4, we notice that increased horizontal resolution for both boundary conditions produces higher uncertainties in the reconstructions of convection-related observables compared to the lower horizontal discretization. Even if we consider only the first half of the horizontal spectrum for a 64-degree reconstruction the robustness of the QRV models does not increase . However, a 64-degree QRV solution for the SS-P simulation models is under or slightly over 10% uncertainty level for the surface divergence, the CMB and dynamic surface topography over the entire 65 Myr time-window (Figs 3.4g, c and e), while the reconstructed 10%-uncertainty for the free-air anomalies is achievable up to 45 Ma (Fig 3.4a).

The QRV reconstruction for the R-boundary condition using a maximum of 64 degrees has slightly shifted and higher misfit compared to the P-boundary condition reconstruction. This implies that a 10%-uncertainty reconstruction for the dynamic surface topography is possible over ~ 55 Myr intervals (Fig 3.4f), while this time-window is 10 Myr shorter for the free-air anomalies (Fig 3.4b). However, we can use the spherical harmonic expansion up to 64 for a very robust CMB topography reconstruction (~ 90%) over the entire 65 Myr interval (Fig 3.4d). After summarizing all L=64 results, we note that modelling of mantle heterogeneity with the QRV yields 90% predictability only on a 40 Myr time-window.

Considering the level of predictability for the reconstructed heat flux, we notice that higher horizontal resolution (64-degrees) for the SS-P model reveals a 'weakness' in the choice of $\beta_2 = 1\times10^{-10}$ in the reconstruction of CMB flux, contrary to the 32-degree simulation (Figs 3.5c and d). The other two formulations of the regularization parameter, the constant $\beta_1 = 1\times10^{-7}$ and the time-varying β-function, are able to deliver the reconstructed heat flow with ~ 10% uncertainty (Fig. 3.5). It is interesting to note that $\beta_1 = 1 \times 10^{-7}$ is able to control heat flux uncertainties for both studied horizontal resolutions (32 and 64) even if the uncertainty in mantle heterogeneities is the highest for this constant formulation (see Table 3.1).

The SS-R compared to the SS-P model delivers slightly different results that show almost no difference between the 32-degree and 64-degree reconstructions of the heat flux using the QRV method with different β-parameters. The SS-R models can provide 90% and higher accuracy reconstructions of the CMB flux with all previously defined β-values (Figs 3.6c,d). Note also the continuous increasing of surface flux errors, up to ~ 30%, for the constant $\beta = 1 \times 10^{-7}$ over a 65 Myr interval (Figs 3.6a,b). The SS-R model again demonstrates that the most reliable reconstruction of heat flux, and therefore geotherm, is delivered with the time-dependent β-function (Fig. 3.6).

Obviously the accuracy of mantle flow reconstructions depends on the maximum spherical harmonics degree and the 32-degree expansion allows us to quantify the backward convection process with error below 10%. We can justify the adoption of such low horizontal resolution by comparing the geodynamical observations calculated with two different spherical harmonic expansions: 32 and 128. The relative error between the present-day 32-degree and 128-degree solutions is below 2% for the convection-related observables. Analyzing all studied scenarios for the β-parameter, we conclude that the time-varying β-function (eq. 3.9) is the optimal set for the QRV method (Table 3.1), and it will be used for the CE-class of models.

As described above, the QRV method is able to restore the heat flux with less than 10% error for the steady-state solutions over the 65 Myr time-windows. However, Glišović et al. (2012) have shown that the Earth's mantle, initialized by the present-day tomographic image and an 'Earth-like' geotherm, is in a transient phase for a few hundreds of Myr, a period characterized by perturbations in the heat flux that can exceed a few TW. Most likely such high perturbations in the heat flux are not the characteristic of the real Earth. However, the change of heat flux can be described by secular cooling. If we assume 11 TW of secular cooling, then we expect to see about 0.7 TW of change in the heat flux over 65 Myr. Also, the value of 0.7 TW is in the range of a geotherm deviation from a true solution (Glišović et al. (2012)) and thus it is appropriate to consider the horizontally-averaged temperature to be constant for the next CE-class of simulations.

3.6.2 Reconstruction of Cenozoic Era

In order to quantify the robustness of backward methods for both boundary conditions over the Cenozoic era, we performed the following models:

1. QRV-2BL is initialized with a corresponding 2BL-geotherm.
2. QRV-2BL-120 is based on the previous one, but to estimate uncertainties, we calculate geodynamic observables considering mantle heterogeneities only between 120 and 2768 km depth.
3. QRV-A is initialized with the adiabatic geotherm.
4. BAD-2BL, where the initial condition at 65 Ma is obtained by the BAD method with the adiabatic geotherm first, and after that, we performed forward integration with the 'Earth-like' geotherm up to the present-day.
5. BAD-2BL-120 is originally based on BAD-2BL. Here we remove, in the post-processing, the first 120 km of mantle heterogeneities from the surface down and from the CMB up.
6. BAD-A, where both integration directions, first the backward and then the forward, are performed using the adiabatic geotherm.

All simulations are initialized with the present-day 3-D tomographic image whose temperature anomalies are diffused over the 1 Myr interval. Also, the QRV simulations are done using the β-function defined by eq. 3.9 and $\beta_0 = \{1 \times 10^{-12}, 1 \times 10^{-13}\}$.

The QRV-2BL model with the P-boundary condition shows the collapsing of oceanic spreading centres only after a few Myr. This collapsing is a purely artificial feature produced by the combination of the 2BL-geotherm and the coupled motion between underlying mantle flow and mobile tectonic plates. We decided to show here only the evolution of the East Pacific Rise (EPR) as an example of this non-geological appearance. From Fig. 3.7 we may notice that this problem is avoided with two models: the QRV-A with the P-boundary condition and the QRV-2BL with the rigid surface.

Analysing the uncertainties for predicted global free-air anomalies over the last 65 Myr we have found that the difference between the observables, calculated with both the whole and truncated mantle heterogeneities, is negligible for the backward methods tested here (Figs 3.8a and b). However, by removing mantle heterogeneities from the TBLs region (~ 120 km, see Glišović et al. (2012)) we can avoid a high misfit in the CMB and, especially, surface topography for the QRV simulation with $\beta_0 = 1 \times 10^{-13}$ (QRV-2BL) during the first 20 Myr of the Cenozoic era (Figs 3.8c and d). At the end of the 65 Myr interval (the present-day), both simulations, the QRV-2BL and QRV-2BL-120, show almost the same level of uncertainty (see Table 3.2).

It is also interesting to notice that use of the R-boundary condition delivers the QRV solutions that are characterized by uncertainties a factor 2 lower than the reconstructions estimated by P-boundary condition (see Table 3.2).

From Fig. 3.8 we observe the uncertainties in the BAD-A simulation that are within 25% but still about two times higher than the QRV-A model errors. Similar to these results, the prediction of geodynamical observables estimated by the BAD-2BL model is far inferior to that obtained by the QRV-2BL simulation over the Cenozoic era. Moreover, a BAD-2BL solution reaches the 65 Myr deviation maximum of the QRV-2BL reconstruction over a very short time-window (~ 20 Myr). However, the effect of surface boundary conditions on the reconstruction of mantle flow with the BAD-A model is negligible (see Table 3.2).

It could be worthwhile to consider an alternative algorithm for the QRV method over the Cenozoic era. Namely, from Figs 3.9e and f, we can spot a peak of surface topography misfit for the model with $\beta_0 = 1 \times 10^{-13}$ at around 20 Myr of elapsed time (i.e. about 45 Ma) and this is avoided by a simulation performed with $\beta_0 = 1 \times 10^{-12}$. Even so, in the last third of the Cenozoic era, 0-20 Ma, the most accurate prediction is provided by $\beta_0 = 1 \times 10^{-13}$. Perhaps we should combine these two sets of QRV-2BL solutions, for both surface boundary conditions, using $\beta_0 = 1 \times 10^{-13}$ for the last 20 Myr and $\beta_0 = 1 \times 10^{-12}$ for the rest of the Cenozoic era. This approach is applicable for the CMB topography (Figs 3.9c and d), but for both the free-air anomalies and surface divergence it appears that the most robust inverse solution is obtained with $\beta_0 = 1 \times 10^{-13}$ (Figs 3.9a, b and g). However, for the P-boundary condition, the uncertainty of $\beta_0 = 1 \times 10^{-12}$ reconstructions around 20 Ma is almost equal to the maximum $\beta_0 = 1 \times 10^{-13}$

misfit (Figs 3.9a and g). Therefore, we can also use this alternative algorithm for both the free-air anomalies and surface divergence reconstructions.

Fig. 3.10 shows the difference between the present-day global free-air gravity anomalies and those estimated from an initial mantle heterogeneity obtained by backward convection models at 65 Ma. We notice that the QRV-2BL model with the P-boundary condition (Fig. 3.10c) yields a higher deviation (37%) from the true solution (Fig. 3.10a) which can be explained by a poor reconstruction under the Pacific trench system. The QRV-2BL simulation with the R-boundary condition delivers reconstructions that are free of uncertainties under the Cocos and Caribbean plates, the Peru-Chile trench (especially Peru and the Altiplano) and the Indonesia and Western Pacific trench systems (Fig. 3.10d). These regions stand out as unresolvable for the BAD-2BL model with the P-boundary condition (Fig. 3.10i); however, contrary to the plate-like boundary condition, the rigid surface delivers a prediction of free-air anomalies of higher accuracy, but uncertainties are still very high (62%) and distributed entirely over the Earth's surface (Fig. 3.10j).

If we change the prediction part of the BAD algorithm and use the adiabatic geotherm (BAD-A model), instead of the 'Earth-like' (BAD-2BL model), to perform integrations forward in time, then we are able to estimate the present-day free-air anomalies from an initial mantle heterogeneity obtained by the BAD method at 65 Ma with significantly increased accuracy (Figs 3.10g and h). Similarly, the QRV-A model, where both backward and forward solutions are calculated with the adiabatic geotherm, delivers a very robust prediction of free-air gravity anomalies (Figs 3.10 e and f). Therefore, these results emphasize the crucial role of initial conditions for the inverse problem of mantle convection.

Figs 3.11 and 3.12 show the difference between a prediction for both the surface topography and the surface divergence calculated from an initial mantle heterogeneity estimated by time-reversed convection models at 65 Ma and present-day values. The same analysis as we performed for the free-air anomalies can be applied to these two geodynamical observables, yielding similar results.

Comparing the present-day value with a predicted solution of the CMB topography (Fig 3.13), we notice that the QRV method does not highlight any particular region with a high uncertainty; moreover, the robustness of the reconstructions is above 90% for all models. However, the BAD

models (especially the BAD-2BL) are not able to be competitive with the QRV reconstructions, emphasizing the uncertainties of predicted broad regions of CMB topography (Figs 3.13g-j).

3.7 Discussion

The robustness of quasi-reversibility (QRV) reconstructions is constrained by the maximum degree of spherical harmonic expansion, and we prescribed L=32 as an optimal horizontal resolution for the pseudo-spectral approach of the QRV method on 65 Myr intervals. However, a higher horizontal resolution (for example, L=64) can be used for the QRV modelling of past mantle heterogeneity over shorter time-windows (~ 40 Myr).

We have formulated the regularization parameter as a time-dependent function (i.e. the β-function, see eq. 3.9) that is able to solve the inverse problem of mantle convection for the steady-state solutions within 10% uncertainty level on an interval equivalent to the duration of the Cenozoic era. Depending on elapsed time, the β-function introduces a very small regularization term into the backward energy equation at the start of integration. It seems that these small starting values of the biharmonic operator are a key advantage of the time-varying β-function relative to the constant formulation of the regularization parameter.

Comparing the results obtained by the QRV method for two different starting internal loading states of the mantle, a steady-state versus the present-day 3-D tomographic image, we have discovered a high sensitivity of reconstruction robustness to the initial conditions of the system. Namely, uncertainties of reconstructed geodynamical observables are a few times higher for the models initialized by the present-day mantle heterogeneity (the CE-class) than for the models initialized by steady-state solutions (the SS-class) using a two boundary layer (2BL or 'Earth-like') geotherm for both classes. The CE-class of models emphasizes the 'incompatibility' of instantaneous mantle flow estimated by the 3-D tomographic image and the thermal boundary layers (TBLs) introduced by a 2BL-geotherm. The 'Earth-like' geotherm reinforces the strong subduction zones in the first 30 Myr, and plumes that extend across the mantle to the opposite TBL after 65 Myr of mantle convection (Glišović et al. (2012)). The consequent mixing of this transported thermal heterogeneity rapidly builds the amplitude of lateral variations in temperature inside the boundary layers. There is no doubt that the geotherm with TBLs plays a crucial

role in the thermal evolution of Earth's mantle constraining the reliability of a reconstructed temperature field at some point in the past. Therefore, one should consider two different β_0-values in order to properly cover the Cenozoic era due to an enormous increase of mantle heterogeneity amplitude inside TBLs (especially the upper one) between 30 Ma and 65 Ma. To achieve 71%, 63%, 67% and 91% predictability of the horizontal divergence of the tectonic plates, free-air gravity anomalies, dynamic surface topography and CMB topography, respectively, we have to apply $\beta_0 = 1 \times 10^{-13}$ from 0 to ~ 20 Ma, and $\beta_0 = 1 \times 10^{-12}$ over the rest of the interval using the QRV method with both the surface tectonic plates (P) boundary condition and the 'Earth-like' geotherm (QRV-2BL model).

An additional implication of an 'Earth-like' geotherm can be described by an artificial collapsing of oceanic spreading centres (for example, the East Pacific Rise) during the backward integration with the P-boundary condition. However, if we introduce an adiabatic (A) geotherm into the backward mantle convection algorithm using the QRV method, and the reconstructed geometry of tectonic plates over the Cenozoic era, then, we are able to control artificial features close to mid-oceanic ridges. Also, this model (QRV-A) compared to QRV-2BL does not generate particular regions with relatively high uncertainties in a prediction of mantle heterogeneity predictions from a reconstructed initial temperature field at 65 Ma. The lack of TBLs in an adiabatic geotherm allows the QRV model with both boundary conditions to fit a true solution of geodynamical observables to a ~ 90% accuracy over the Cenozoic era. The QRV-A uncertainty for the CE-class of inversions is about the same magnitude as the error obtained using the QRV-2BL model with steady-state solutions (SS-class). This comparison leads us to speculate that the horizontally-averaged temperature profile derived from the present-day tomographic image is similar to the adiabatic geotherm.

Collapsing of mid-oceanic ridges raises a consideration of the rigid (R) surface as an alternative surface boundary condition using the QRV-2BL model. The QRV-2BL simulation with the R-boundary condition is also able to preserve emerging hot material onto the ocean floor over a considerably long time-window during the past 65 Myr of mantle evolution. With the exception that the QRV-2BL with the rigid surface is able to control collapsing of oceanic spreading centres, it predicts relatively robust reconstructions of the free-air gravity anomalies (81% accu-

racy), the CMB topography (94%) and the dynamic surface topography (90%). However, any rigid surface simulation is not able to provide information regarding the surface divergence.

Estimating a prediction of the geodynamical observables without TBLs (simulations with 120 suffix) is reasonable only for periods characterized with an enormous increase of the amplitude of lateral variations inside TBLs (for example, from 30 Ma to 65 Ma). However, error in predictions obtained with QRV-2BL (with TBLs) and QRV-2BL-120 (without TBLs) is almost equal because such estimations, as well as all others, must be considered with the peak error calculated on the basis of the entire interval.

For the CE-class of simulations we were not able to predict the heat flux over the Cenozoic era, and therefore we used a constant geotherm. However, the steady-state simulations (the SS-class) show the efficiency of the time-varying β-function in keeping the level of predictability around 95% on the 65 Myr interval.

In order to measure the effect of ignoring the irreversible terms (dissipation and diffusion especially) in the energy equation by the BAD method we have to predict the backward solutions using the two boundary layer geotherm. Using an 'Earth-like' geotherm for the direct problem (the BAD-2BL model) indicates that the BAD method failed to deliver a robust initial inverse solution. In other words, the BAD-2BL simulation is not able to preserve the maximum uncertainty estimated by the QRV method over a period more than 20 Myr. Therefore the QRV method is superior in relation to the BAD method which is only able to provide accurate reconstructions using an adiabatic geotherm (the BAD-A models) in both directions of integration over the 65 Myr time-window. The robustness of QRV-A simulation is about two orders of magnitude greater than that of the BAD-A model.

Summarizing all QRV results we define a range of robustness for the free-air gravity anomalies, the CMB topography, the dynamic surface topography and the horizontal divergence of the tectonic plates that are [63,89]%, [91,94]%, [67,92]% and [71,93]%, respectively.

3.A Regularization operator for the QRV method

The Laplacian operator as a function of radius and the spherical harmonics degree is defined by the following relation:

$$\begin{aligned} L &= \frac{1}{r^2}\frac{\partial}{\partial r}\left(r^2\frac{\partial T}{\partial r}\right) - \frac{\ell(\ell+1)}{r^2}T \\ &= \frac{\partial^2 T}{\partial r^2} + \frac{2}{r}\frac{\partial T}{\partial r} - \frac{\ell(\ell+1)}{r^2}T\,. \end{aligned} \tag{3.10}$$

It is easy to show that the first derivative of Laplacian is given by

$$\frac{\partial L}{\partial r} = \frac{\partial^3 T}{\partial r^3} + \frac{2}{r}\frac{\partial^2 T}{\partial r^2} - \frac{2+\ell(\ell+1)}{r^2}\frac{\partial T}{\partial r} + \frac{2\ell(\ell+1)}{r^3}T \tag{3.11}$$

and the formula for the second derivative of Laplacian is

$$\frac{\partial^2 L}{\partial r^2} = \frac{\partial^4 T}{\partial r^4} + \frac{2}{r}\frac{\partial^3 T}{\partial r^3} - \frac{4+\ell(\ell+1)}{r^2}\frac{\partial^2 T}{\partial r^2} + \frac{4+4\ell(\ell+1)}{r^3}\frac{\partial T}{\partial r} - \frac{6\ell(\ell+1)}{r^4}T\,. \tag{3.12}$$

The QRV term is composed by the multiplication of a regularization operator, Λ, and a corresponding parameter, β. We only know that Λ must be a high-order derivative of the regularizing term, and in the case of the pseudo-spectral method, the most appropriate way to construct Λ is to take the Laplacian of the diffusion, D. Thus, we have

$$\Lambda = \frac{\partial^2 D}{\partial r^2} + \frac{2}{r}\frac{\partial D}{\partial r} - \frac{\ell(\ell+1)}{r^2}D \tag{3.13}$$

where

$$D = \frac{\partial k}{\partial r}\frac{\partial T}{\partial r} + kL \tag{3.14}$$

$$\frac{\partial D}{\partial r} = \frac{\partial^2 k}{\partial r^2}\frac{\partial T}{\partial r} + \frac{\partial k}{\partial r}\left(\frac{\partial^2 T}{\partial r^2} + L\right) + k\frac{\partial L}{\partial r} \tag{3.15}$$

$$\frac{\partial^2 D}{\partial r^2} = \frac{\partial^3 k}{\partial r^3}\frac{\partial T}{\partial r} + \frac{\partial^2 k}{\partial r^2}\left(2\frac{\partial^2 T}{\partial r^2} + L\right) + \frac{\partial k}{\partial r}\left(\frac{\partial^3 T}{\partial r^3} + 2\frac{\partial L}{\partial r}\right) + k\frac{\partial^2 L}{\partial r^2}\,. \tag{3.16}$$

We use the thermal conductivity profile considering the effect of thermal boundary layers

(Hofmeister (1999)), and it is a non-linear function of radius, and thus, there are first, second and third derivatives. In the case of a constant conductivity, Λ is a biharmonic operator where all derivatives of k are dropped.

3.B Solution of the regularized equation of energy conservation

3.B.1 Numerical scheme

This section describes the numerical scheme employed to advance the solution of the regularized equation of energy conservation (eq. 3.4) in time. We use the complete predictor-corrector numerical scheme for the time stepping of the non-linear terms. To simplify the writing of the equations, the diffusivity term is written as the expression of the spherical harmonic coefficients

$$(\nabla.k\nabla T)(t) = D_{in}\, T_n(t), \tag{3.17}$$

where

$$D_{in} = \left(\frac{2}{N}\right)^{\frac{1}{2}} k_i \left(\frac{\partial^2 \mathcal{C}_{in}}{\partial r^2} + \frac{1}{r^2 k_i} \frac{\partial r_i^2 k_i}{\partial r} \frac{\partial \mathcal{C}_{in}}{\partial r} - \frac{\ell(\ell+1)}{r_i^2} \mathcal{C}_{in} \right) . \tag{3.18}$$

The non-linear terms are also gathered together in spherical harmonic coefficients such that

$$b_i(t) \;=\; -\rho c_p (\mathbf{u}.\nabla T)_i + (\alpha T \frac{dp}{dt})_i + \Phi_i \, . \tag{3.19}$$

In equation (3.17) the summation over the index n is implicit. The index i denotes the value at depth r_i of the variable considered; for example, $k(r_i) = k_i$. In the particular case of the Chebyshev polynomials, we use the notation $\mathcal{C}_{in} = \mathcal{C}_n(x_i)$.

If we assume that time-integration interval is discretised in the M time-points, $j = 0, ..., M-1$, and the solution is known at time t_j and t_{j-1}, then the numerical scheme employed to compute the solution at time t_{j+1} is described by the following equations:

- Predictor (non-linear terms) + Crank-Nicholson scheme (diffusion)

$$T_i^* + \left(\beta\Lambda_{in} - \frac{\Delta t_j}{2} D_{in}\right) T_n^* = T_i(t_j) + \left(\beta\Lambda_{in} + \frac{\Delta t_j}{2} D_{in}\right) T_n(t_j) + \Delta t_j \left((1 + \frac{\Delta t_j}{2\Delta t_{j-1}}) b_i(t_j) - \frac{\Delta t_j}{2\Delta t_{j-1}} b_i(t_{j-1}) \right) + \Delta t_j Q . \quad (3.20)$$

- Corrector (non-linear terms) + Crank-Nicholson scheme (diffusion)

$$T_i(t_{j+1}) + \left(\beta\Lambda_{in} - \frac{\Delta t_j}{2} D_{in}\right) T_n(t_{j+1}) = T_i(t_j) + \left(\beta\Lambda_{in} + \frac{\Delta t_j}{2} D_{in}^m\right) T_n(t_j) + \Delta t_j \left(\frac{1}{2} b_i^* + \frac{1}{2} b_i(t_j) \right) + \Delta t_j Q . \quad (3.21)$$

Δt_{j-1} and Δt_j are two successive time steps; the time step varies according to the Courant stability criterion described by equation (3.31) below. T^* represents the predicted temperature at time t_{j+1} and before correction, b^* is the corresponding predicted non-linear term.

The above procedure can not be employed for the first iteration because it requires the solutions at two successive time steps. Therefore, the following semi-implicit backward differentiation formula (Ascher et al. (1995)) is employed for the predictor-corrector method for the first iteration:

- Predictor scheme

$$T_i^* + (\beta\Lambda_{in} - \Delta t_j D_{in})\, T_n^* = T_i(t_j) + \beta\Lambda_{in}\, T_n(t_j) + \Delta t_j b_i(t_j) + \Delta t_j Q . \quad (3.22)$$

- Corrector scheme

$$T_i(t_{j+1})\,(\beta\Lambda_{in} - \Delta t_j D_{in})\;T_n(t_{j+1}) = T_i(t_j) + \beta\Lambda_{in}\,T_n(t_j) + \Delta t_j\left(\frac{1}{2}\,b_i^{*} + \frac{1}{2}\,b_i(t_j)\right) + \Delta t_j\,Q\,. \tag{3.23}$$

3.B.2 Thermal boundary conditions

Both, the inverse and the direct problem of the time-dependable mantle convection require boundary conditions at the surface (r_0) and at the CMB (r_N). There are two types of boundary conditions which can be used, either isothermal boundary or constant heat flux. In this study we have employed isothermal conditions for both the surface and the CMB using the spherical harmonic coefficients ($\binom{m}{l}$) representation.

At the surface,

$$T_0^0(r_0) = \left(\frac{2}{N}\right)^{\frac{1}{2}} \sum_{n=0}^{N}{}'' T_{0n}^0\, C_n(x_0) = T_{\text{surf}} \tag{3.24}$$

since $C_n(x_0) = 1$, we are left with

$$\left(\frac{2}{N}\right)^{\frac{1}{2}} \sum_{n=0}^{N}{}'' T_{0n}^0 = T_{\text{surf}}\,. \tag{3.25}$$

The other harmonics vanish as there are no lateral variations of temperature, hence

$$\sum_{n=0}^{N} T_{\ell n}^m = 0 \qquad \forall \ell, m \neq 0\,. \tag{3.26}$$

Similarly, at the core-mantle boundary, we have

$$\left(\frac{2}{N}\right)^{\frac{1}{2}} \sum_{n=0}^{N}{}'' (-1)^n T_{0n}^0 = T_{\text{cmb}} \tag{3.27}$$

and

$$\sum_{n=0}^{N} (-1)^n T_{\ell n}^m = 0 \qquad \forall \ell, m \neq 0\,. \tag{3.28}$$

To properly solve the inverse problem of energy conservation using the pseudo-spectral QRV

method we must consider the additional boundary condition defined as the diffusion operator in spherical harmonic coefficients:

$$D_{\ell i}^{m} = \frac{\partial k_i}{\partial r}\frac{\partial T_i}{\partial r} + k_i L_{\ell i}^{m} = 0 \tag{3.29}$$

where L is the Laplacian operator, and k thermal conductivity. The allowed values for the index i are 0 and N, where 0 denotes the surface, while N represents the CMB boundary.

3.B.3 Solution of the system

The equations of the predictor-corrector scheme coupled with the appropriate boundary conditions can be written in a matrix form for each degree ℓ and order m independently (Glatzmaier (1984)) such as

$$A_{in}X_n = B_i \tag{3.30}$$

where i corresponds to the index of depth and n the degree of Chebyshev polynomials. The size of the matrix A is $(N+3)\times(N+1)$. The $i=0$ and $i=N$ row of the matrix A_{in} correspond to the boundary conditions given by equations (3.25) through (3.28), while the additional boundary conditions (3.29) are represented by the $i=N+1$ and $i=N+2$ line.

There are $l(l+1)/2$ systems of form (3.30) to be solved where l is the maximum degree of the spherical harmonic expansion. Since A_{in} does not depend on m (eq. 3.18), there are only l matrices to be inverted. The singular value decomposition (SVD) method is used to invert the matrices. The decompositions may be stored because the A_{in}'s do not depend on time. However, they depend on Δt which may vary due to numerical stability requirements (eq. 3.31) and we must therefore recompute the matrices.

The solutions X_n of the systems (3.30) are the Chebyshev and spherical harmonic coefficients of the temperature $T_{\ell n}^{m}(t)$. These coefficients will be used to recompute the new radial derivatives of temperature needed for the evaluation of the spherical harmonic coefficients of the diffusive and the regularization terms. Then, the spherical harmonic coefficients $T_{\ell}^{m}(r,t)$ will be synthesized at every depth to evaluate non-linear terms of the energy equation (for more details see Glišović et al. (2012)).

3.B.4 Numerical stability requirements

The Crank-Nicholson scheme is unconditionally stable whereas restrictions apply on the size of the time step which are necessary to maintain the stability of the advective scheme (Glatzmaier (1984)). The length of the time step is controlled by the Courant criterion which must be satisfied at any time:

$$\Delta t \leq \left|\frac{\Delta r}{u_r}\right|_{\text{MIN}} \text{ and } \Delta t \leq \left|\frac{r}{\sqrt{l(l+1)(u_\theta^2+u_\phi^2)}}\right|_{\text{MIN}} \tag{3.31}$$

where u_r, u_θ and u_ϕ are velocity components. Typically, in actual numerical simulations, we set Δt to be half of the maximum value allowed by the above expressions, and for time-reversed mantle convection simulations the time step is negative.

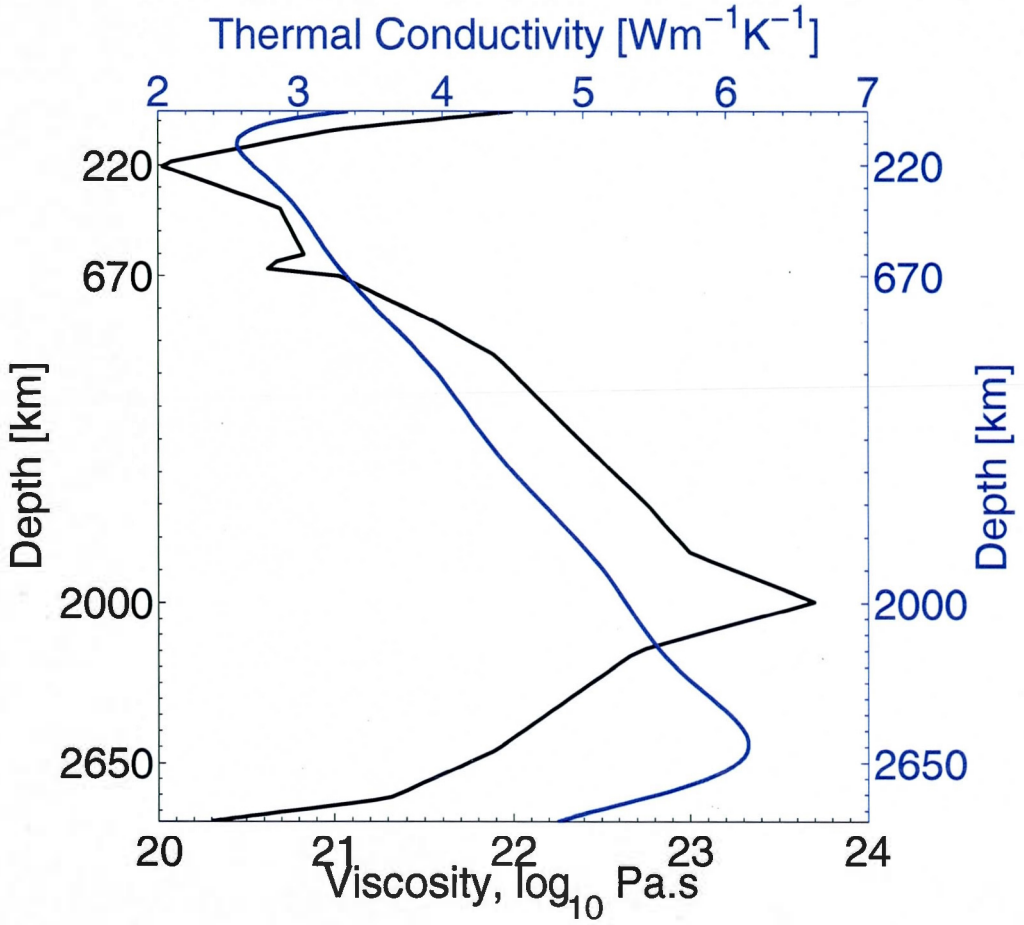

Figure 3.1: The V2-profile (black line) is characterized by a two order of magnitude reduction in viscosity across the uppermost mantle, where 220 km is the depth at which the V2-profile has minimum viscosity. Deeper in the mantle, there is a great increase in viscosity, about 1600×, from 635 km to 2000 km depth - where the latter corresponds to the depth of maximum viscosity in the mantle. In the lower 900 km of the mantle, the V2 profile exhibits a 3-order of magnitude decrease of viscosity extending down to the CMB. The thermal conductivity (blue line) decreases inside the upper TBL from 3.3 $\mathrm{Wm^{-1}K^{-1}}$ to 2.5 $\mathrm{Wm^{-1}K^{-1}}$, and at the top of the D"-layer k takes the maximum value of 6.25 $\mathrm{Wm^{-1}K^{-1}}$, while at the CMB its value is 4.8 $\mathrm{Wm^{-1}K^{-1}}$.

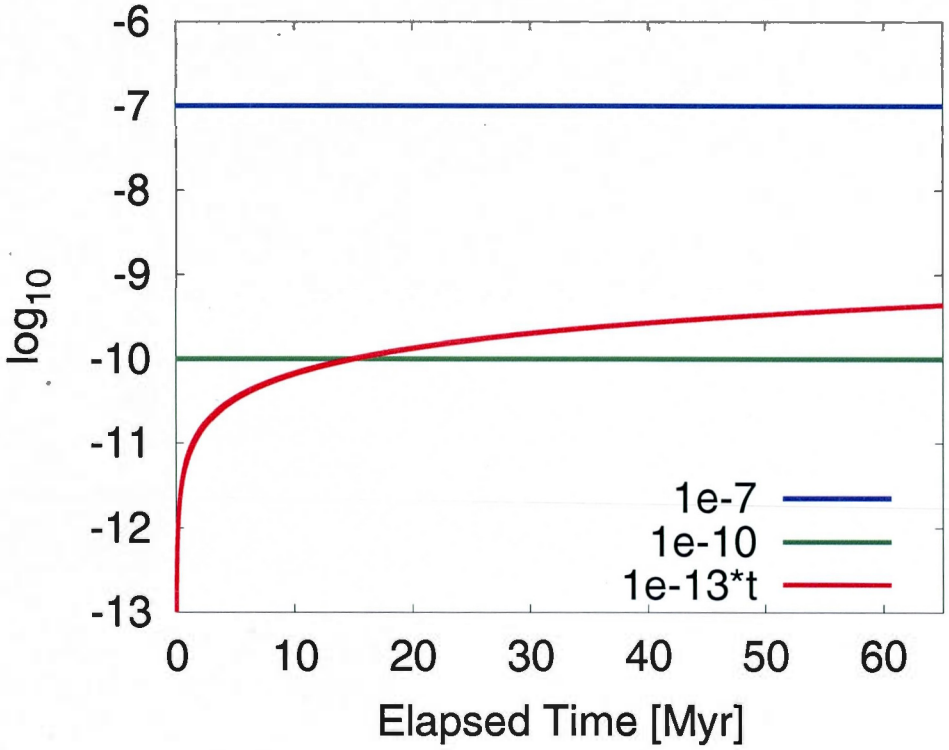

Figure 3.2: The values of regularization β-parameter for the QRV method defined as (1) a constant value (green and blue lines) and (2) a function of dimensionless time (red line) over a period of 65 Myr.

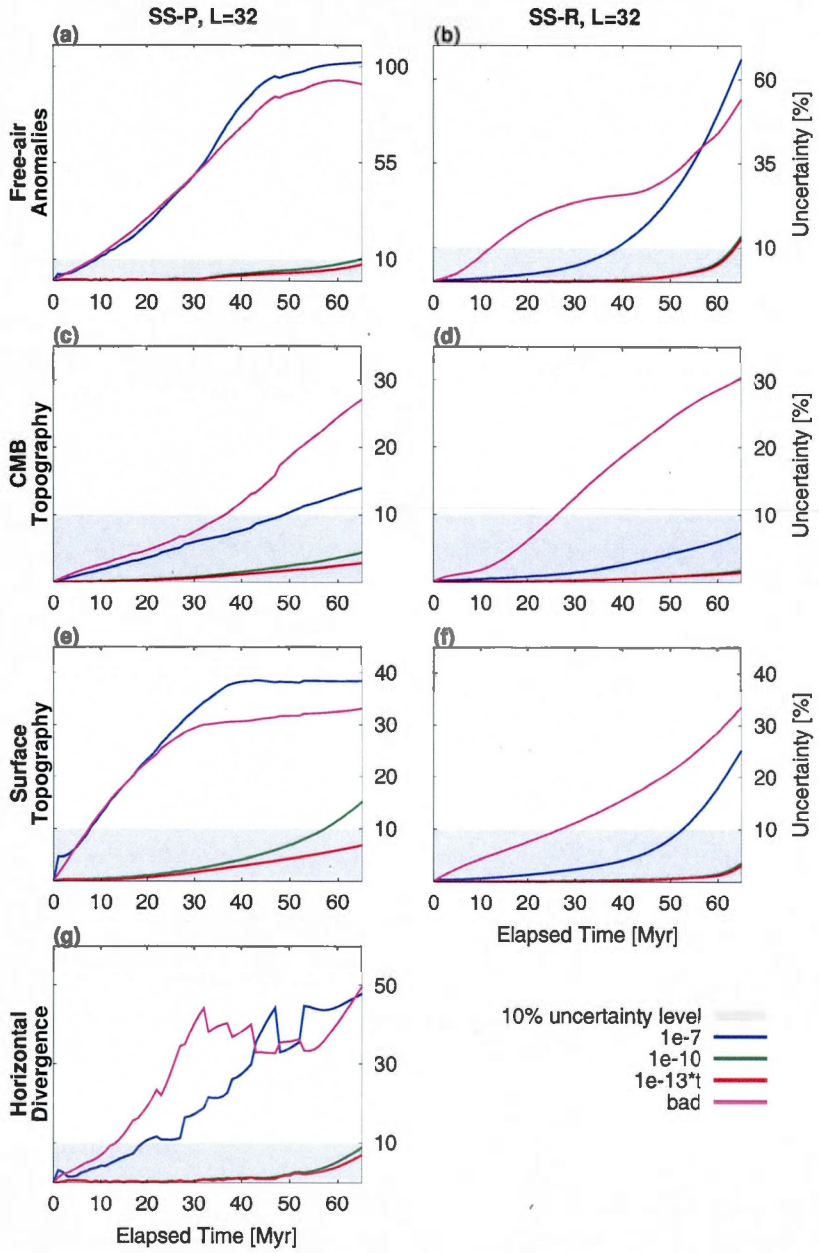

Figure 3.3: The geodynamical observables uncertainties for the backward methods (QRV and BAD) calculated on a 65 Myr time-window using a steady-state solution as an initial temperature field for the corresponding boundary condition (represented by columns). The uncertainties (free-air gravity anomalies, the dynamic CMB and surface topography and the horizontal divergence of tectonic plates - given by rows) are estimated for different β parametrization. The magenta line represents the BAD method uncertainty. Also, uncertainties are compared with the 10% uncertainty level (grey area).

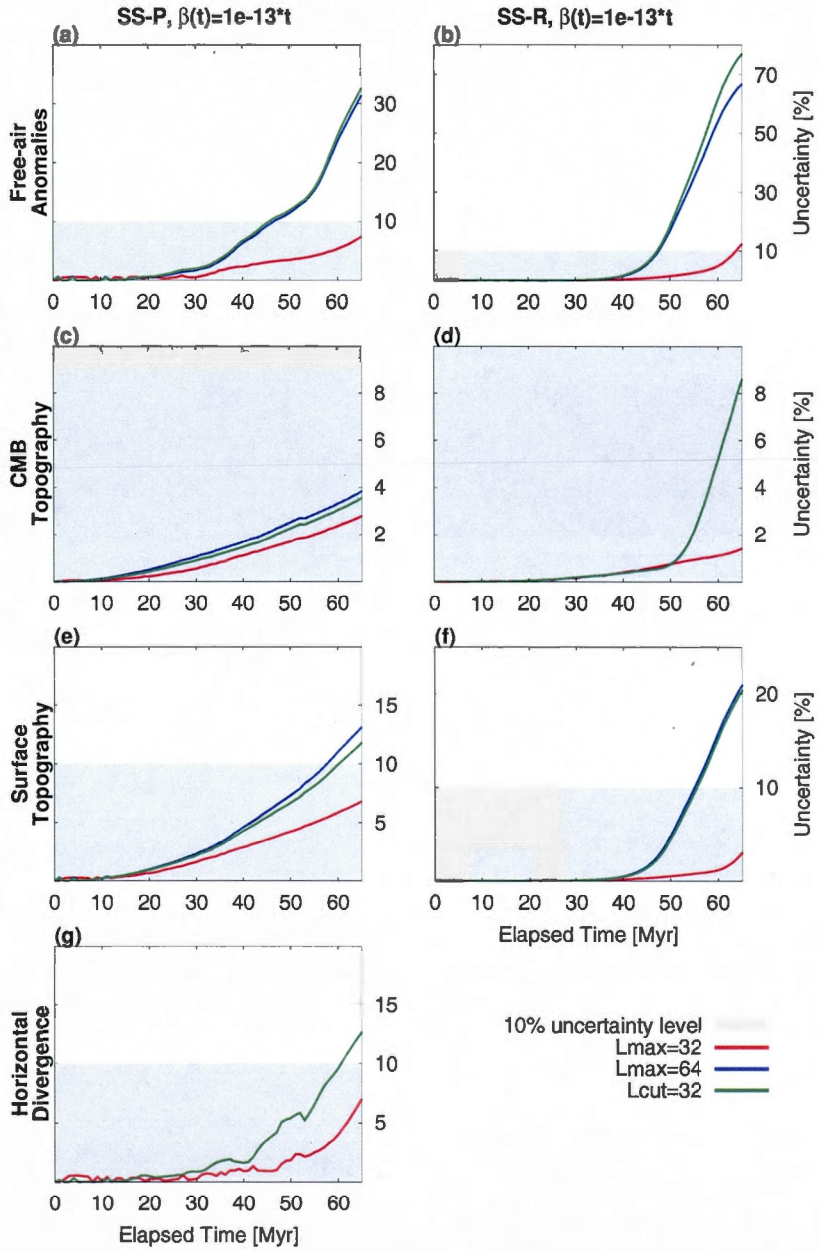

Figure 3.4: The implications of a higher horizontal discretization on the QRV reconstruction of free-air gravity anomalies, the dynamic CMB and surface topography, and the horizontal divergence of the tectonic plates (represented by rows) for different boundary conditions (given by columns). The red and blue lines represent uncertainties of geodynamic observables calculated with the maximum of 32 and 64 spherical harmonics, respectively. The green line shows uncertainties estimated for the half of 64-degree simulation (the blue line).

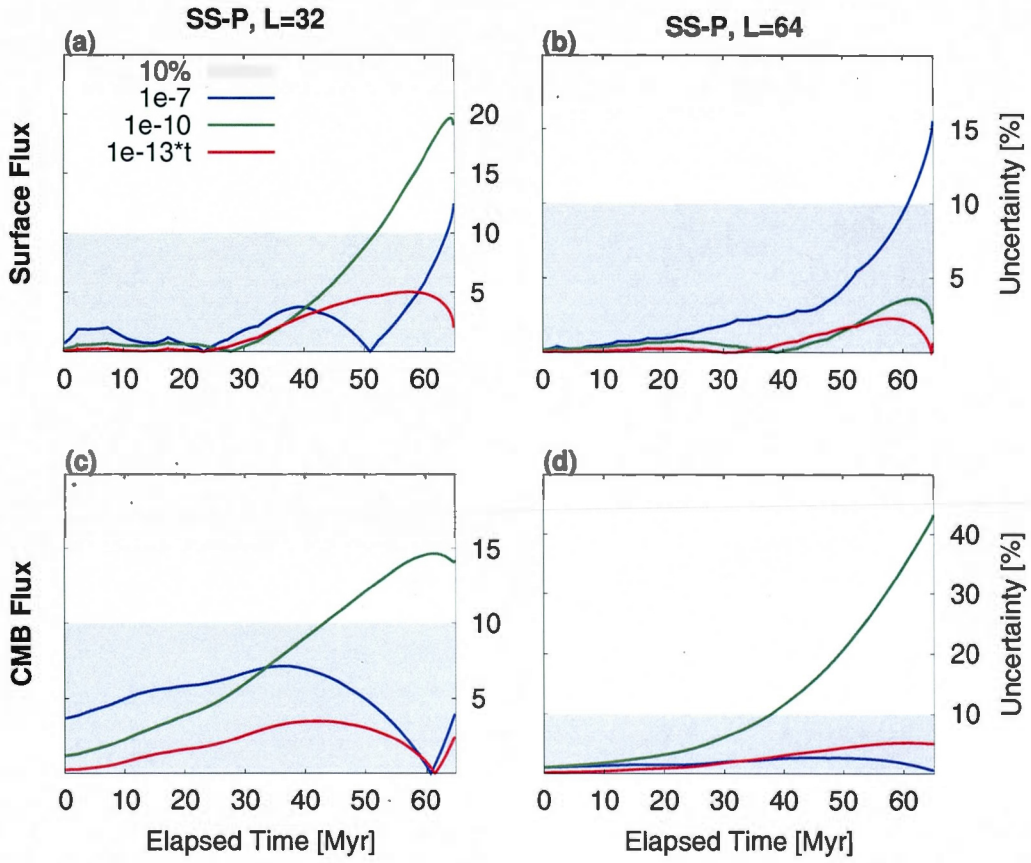

Figure 3.5: The implications of a higher horizontal discretization on the QRV estimation of the heat flux for the plates (P) boundary condition. The reconstructed heat flux uncertainties are calculated for different β-parameters and then compared with the 10%-level.The 32- and 64-degree results are separated by columns.

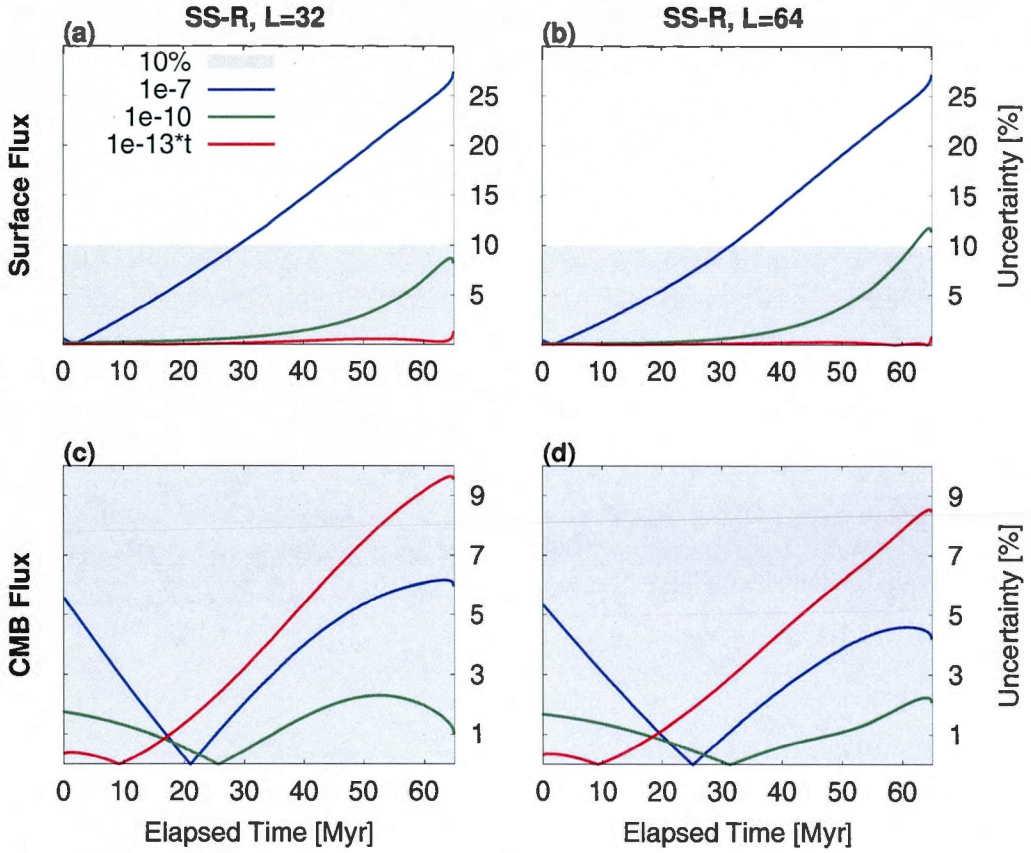

Figure 3.6: The implications of a higher horizontal discretization on the QRV estimation of the heat flux for the rigid surface (R-boundary condition). Uncertainties of reconstructed heat flux are calculated for different β-values and compared with the 10%-level. The 32- and 64-degree results are separated by columns.

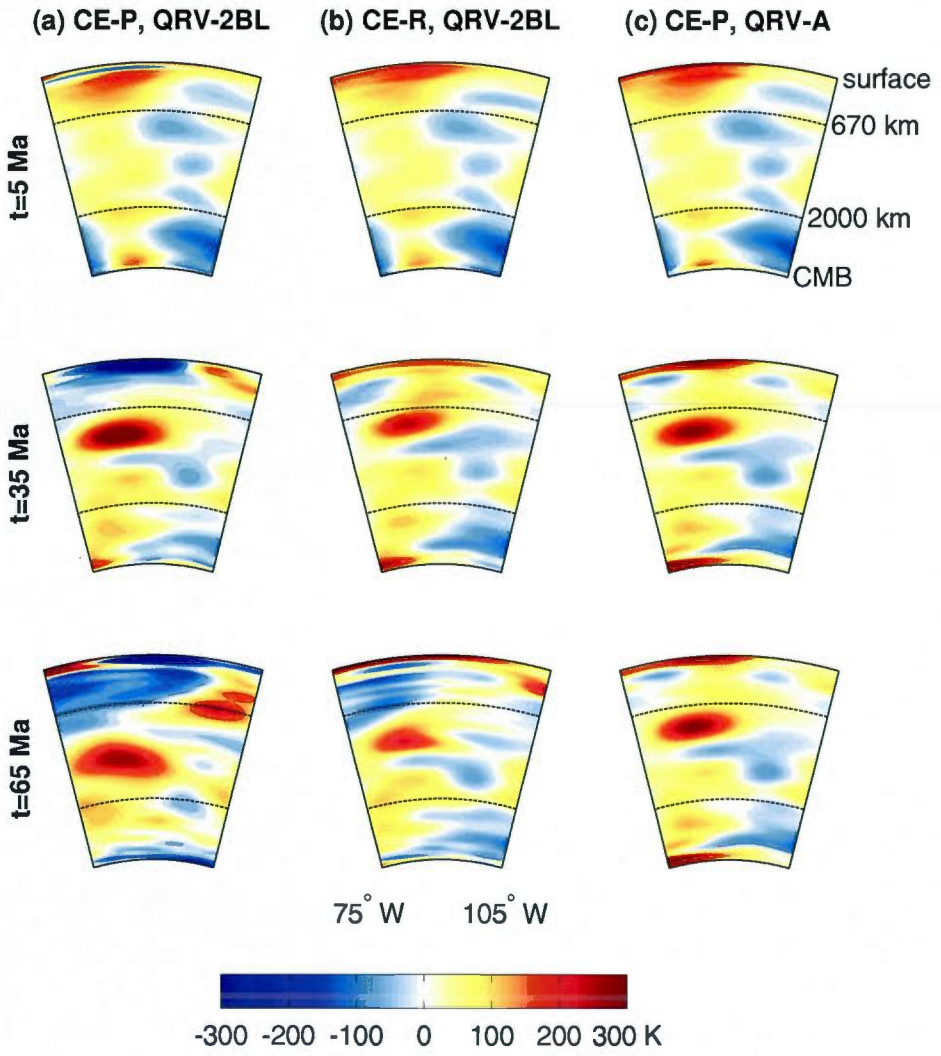

Figure 3.7: The equatorial cross-section of reconstructed mantle heterogeneities under part of the East Pacific Rise (EPR) from 75°W to 105°W (the CE-class). The inverse solutions for different QRV models are given by columns at 5, 35, and 65 Ma represented by rows respectively. The QRV-2BL model with the P-BC (1st column) shows collapsing of the EPR in the first 5 Myr. Other models, the QRV-2BL with the R-BC (2nd column) and the QRV-A with the P-BC (3rd column), demonstrate the persistence of hot anomalies under the centre of EPR for a time that exceeds 30 Ma.

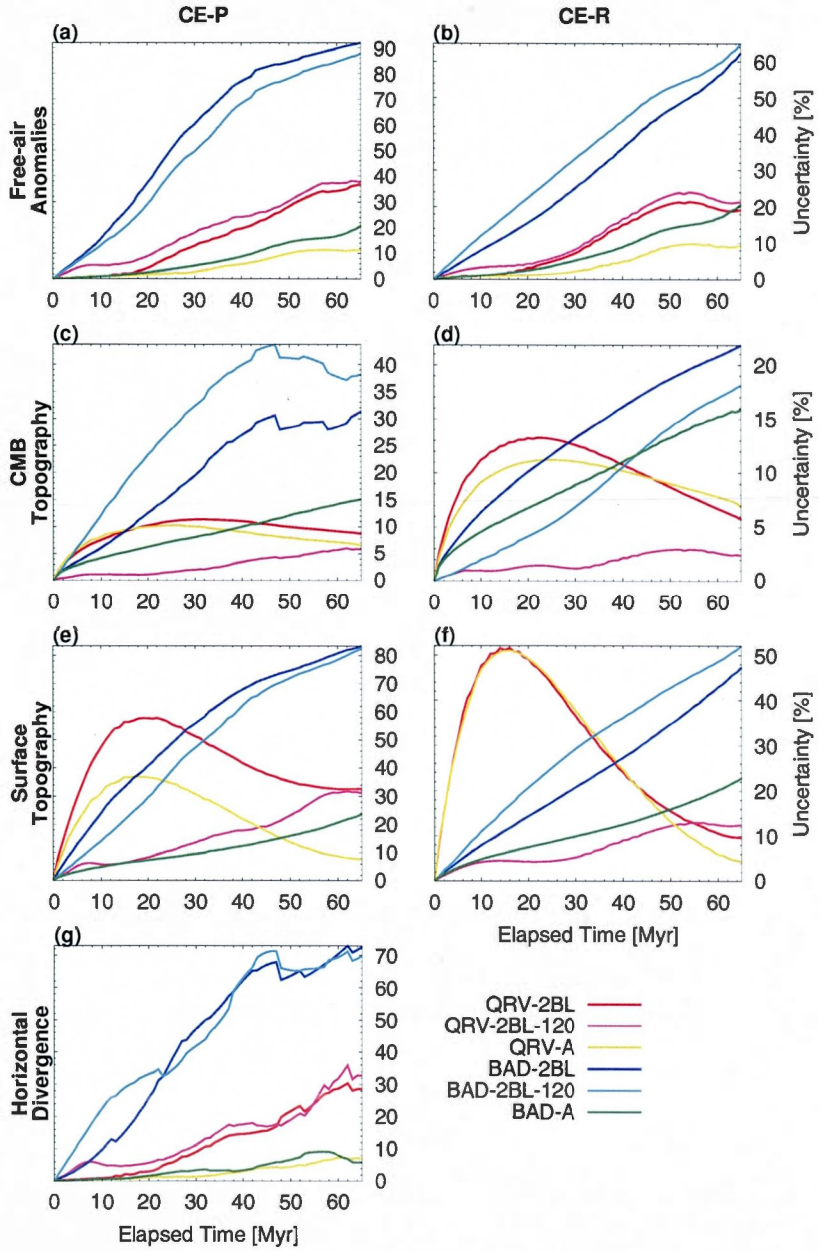

Figure 3.8: The uncertainties of predicted geodynamical observables (given by rows) initialized with the QRV and BAD inverse solutions at 65 Ma. The backward method starting conditions are the present-day tomographic image and a steady-state geotherm using both boundary conditions (represented by columns). The red and blue lines consider total mantle heterogeneities in the mistrust estimations. The magenta and cyan represent uncertainties calculated only with lateral variations in temperature between 120 and 2768 km depth. The green and gold lines show 'errors' of reconstructions obtained by the adiabatic geotherm.

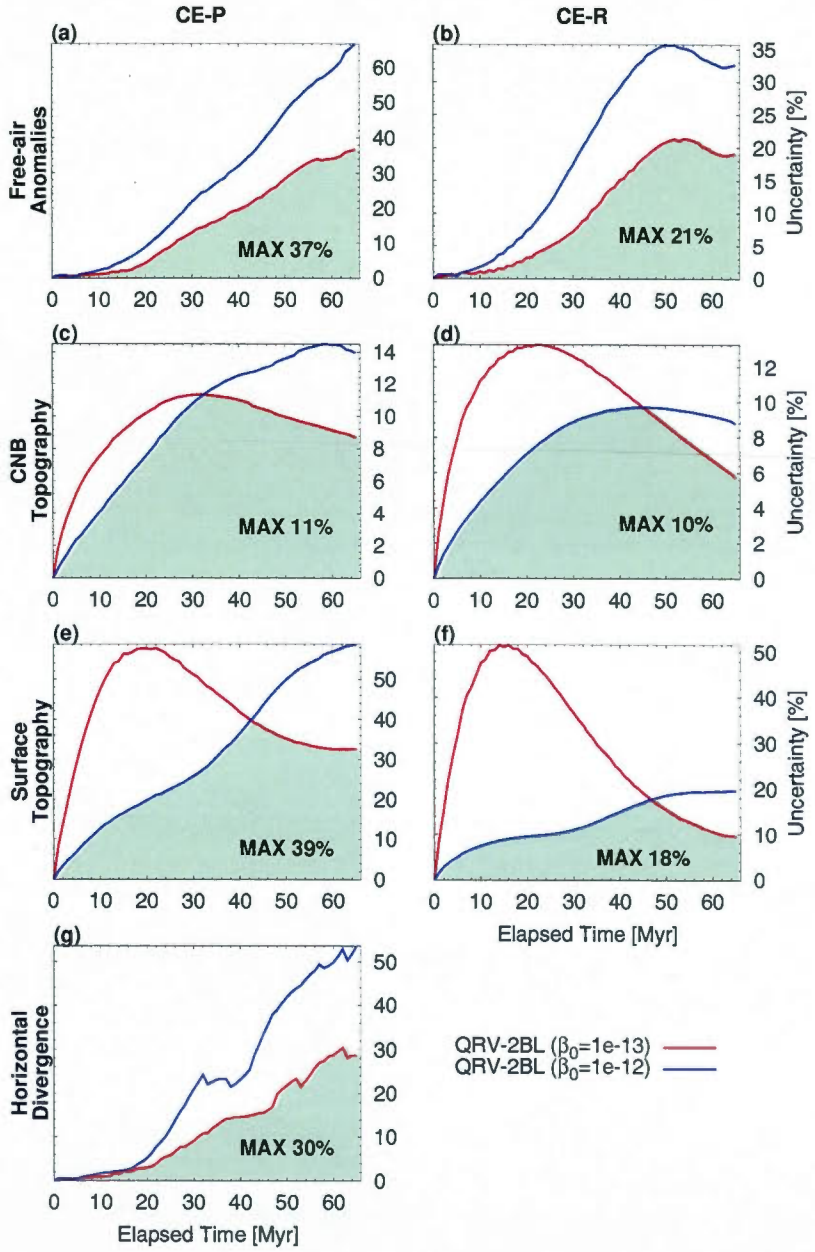

Figure 3.9: The robustness of geodynamical observables (rows) for the QRV-2BL models using the β-function and two different values of β_0-parameter, 1×10^{-12} (blue line) and 1×10^{-13} (red line) over the Cenozoic era for the rigid plates (1st column) and the rigid surface (2nd column) boundary conditions. The light-green area represents the optimal range of uncertainties combining two QRV reconstructions of mantle convection.

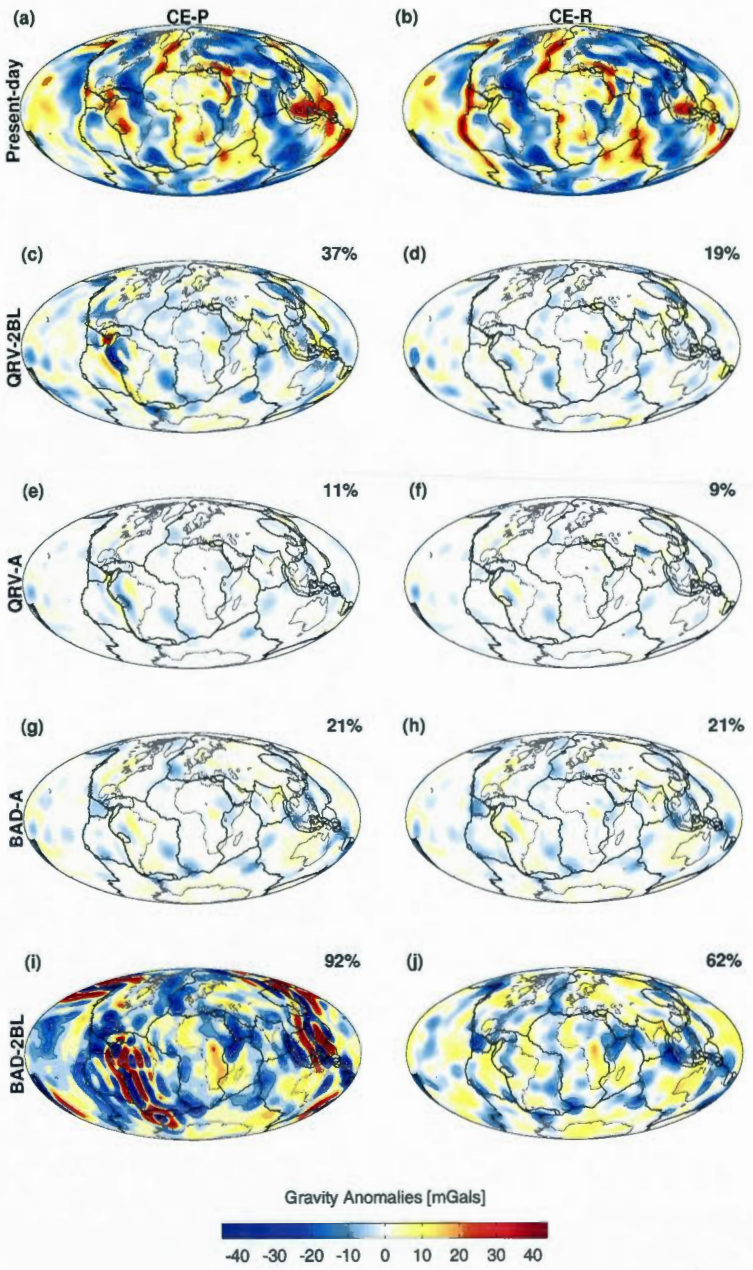

Figure 3.10: The differences between the present-day (1st row) and predicted free-air gravity anomalies from an initial mantle heterogeneity obtained by the time-reversed mantle convection models at 65 Ma. The deviation of estimated gravity anomalies for P- and R-boundary condition is given by columns. Each reconstruction model (given by the rows 2-5) is characterized with the total value of uncertainty [%].

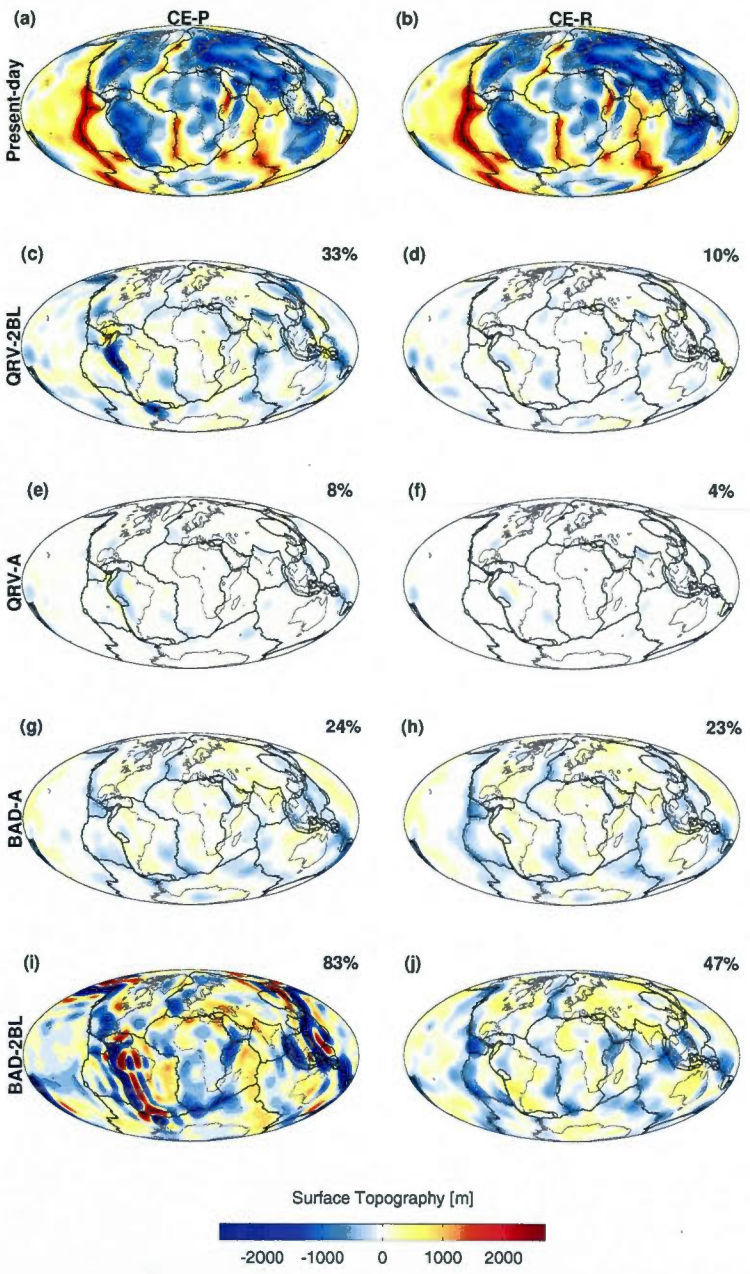

Figure 3.11: The differences between the present-day (1st row) and predicted dynamic surface topography from an initial mantle flow estimated by time-reversed models at 65 Ma. The deviation of calculated surface topography for the P- and R-boundary condition is given by columns. Each reconstruction model (represented by rows 2-5) is characterized with the total value of misfit [%].

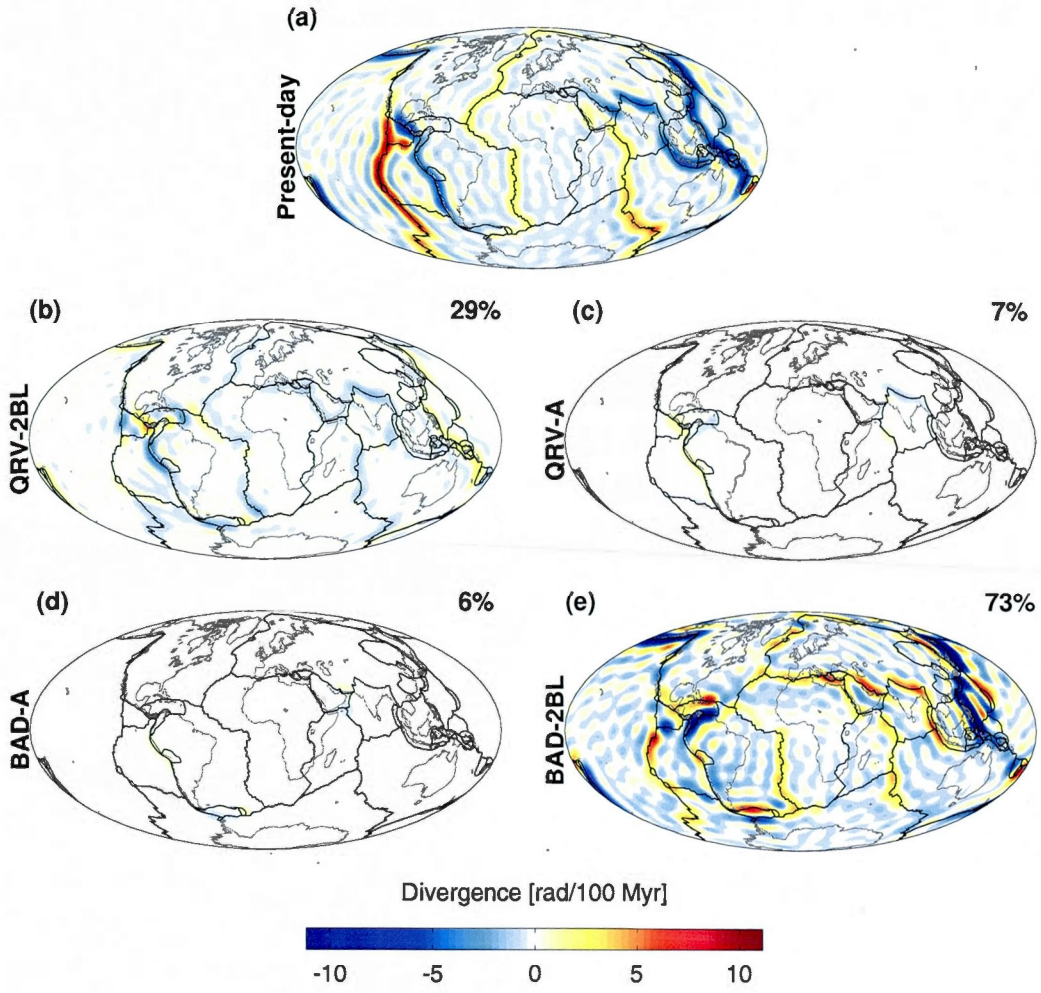

Figure 3.12: The differences between the present-day (1st map at the top) and predicted horizontal divergence of the tectonic plates from an initial mantle heterogeneity obtained by backward mantle convection models at 65 Ma.

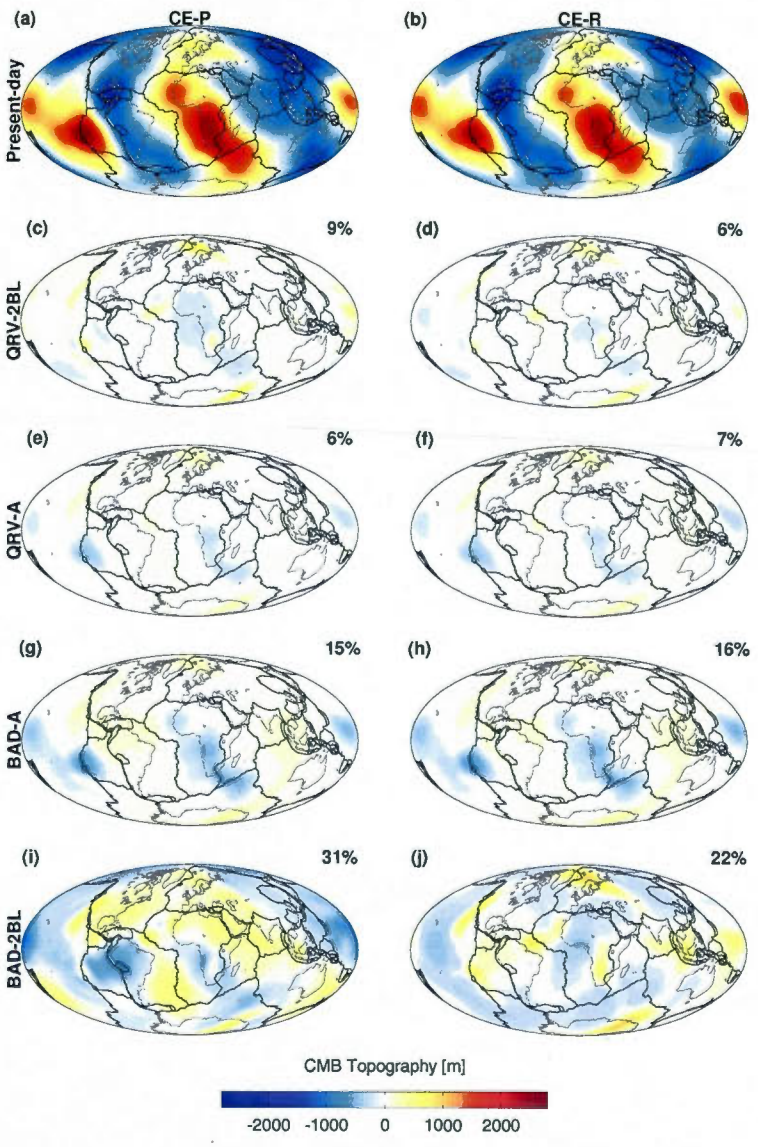

Figure 3.13: The differences between the present-day (1st row) and predicted CMB topography from an initial mantle heterogeneity obtained by time-reversed mantle convection models at 65 Ma. The deviation of estimated CMB topography for mobile surface plates (P-BC) and the rigid surface (R-BC) is represented by columns. Each reconstruction model (rows 2-5) is characterized with the total value of uncertainty [%].

Table 3.1: The Global Uncertainties of the Steady-state Class Predictions for the Geodynamical Observables and Heat Flux. The global uncertainties for free-air gravity anomalies, the dynamic CMB and surface topography, the horizontal divergence of the tectonic plates and the heat flux are based on a reconstructed mantle flow for the SS-class, i.e. the class of steady-state solutions, over a 65 Myr interval using two inverse methods (QRV and BAD). The QRV reconstruction is done using three different β-parametrizations ($1 \times 10^{-7}, 1 \times 10^{-10}$ and $\beta(t)$), while the inverse integration for the BAD method is performed with an adiabatic geotherm while the direct problem is solved with a 2BL-geotherm. The sign + denotes that the solution at the end of 65 Myr is below 10%-level of uncertainties, while we use the sign - to denote the opposite. In the right lower corner of this table we represent the summation of + sign for each simulation of time-reversed mantle convection methods.

		Geodynamical observation [%]				Flux [%]		
Model	Method	Free-air Anom.	CMB Topo.	Surf. Topo.	Horiz. Div.	Surf.	CMB	Total (+)
SS-P	1×10^{-7}	102 (-)	14 (-)	38 (-)	48 (-)	12 (-)	4 (+)	1 of 6
	1×10^{-10}	10 (+)	4 (+)	15 (-)	9 (+)	19 (-)	14 (-)	3 of 6
	$\beta(t)$	7 (+)	3 (+)	7 (+)	7 (+)	2 (+)	2 (+)	6 of 6
	BAD	92 (-)	27 (-)	33 (-)	50 (-)			0 of 4
SS-R	1×10^{-7}	66 (-)	7 (+)	25 (-)		27 (-)	6 (+)	2 of 5
	1×10^{-10}	13 (-)	2 (+)	4 (+)		8 (+)	1 (+)	4 of 5
	$\beta(t)$	13 (-)	1 (+)	3 (+)		1 (+)	10 (+)	4 of 5
	BAD	54 (-)	30 (-)	33 (-)				0 of 3

Method	P+R
1×10^{-7}	3 of 11
1×10^{-10}	7 of 11
$\beta(t)$	10 of 11
BAD	0 of 7

Table 3.2: Present-Day Global Uncertainties for the Class of Cenozoic Era Predictions. The uncertainties quantify an ability of inverse mantle convection methods to deliver an initial loading state of the system at 65 Ma from which we may predict the present-day free-air gravity anomalies, the dynamic CMB and surface topography and the horizontal divergence of the tectonic plates. The 1st column represents the backward model used for solving of the inverse mantle flow problem. The 2nd column shows different types of boundary conditions (R for the rigid surface, and P for the mobile surface plates). The uncertainties of reconstructed geodynamical observables at the present-day are given from the 3rd to 6th column.

		Geodynamical observables [%]			
Model	BC	Free-air Anom.	CMB Topo.	Surf. Topo.	Horiz. Div.
QRV-2BL	P	37	9	33	29
	R	19	6	10	
QRV-2BL-120	P	37	6	31	33
	R	21	2	12	
QRV-A	P	11	6	8	7
	R	9	7	4	
BAD-2BL	P	92	31	83	73
	R	62	22	47	
BAD-2BL-120	P	88	38	83	70
	R	65	18	52	
BAD-A	P	21	15	24	6
	R	21	16	23	

CONCLUSION

We have developed a pseudo-spectral numerical model of compressible, gravitationally consistent, thermal convection in a spherical-shell planetary mantle that is capable of delivering accurate and robust solutions over very long geological scales. For Earth-like Rayleigh numbers, we find that a fully resolved solution of thermal convection dynamics in the upper mantle may require a horizontal expansion of the field variables up to spherical harmonic degree 512. In contrast, for a fully-resolved description of convection dynamics in the lower mantle, we find that a spherical harmonic truncation level at degree 128 is entirely sufficient. These differences in depth-dependent numerical resolution are consequences of the radial viscosity profile of the mantle that is constrained by surface geodynamic data, in which the average viscosity of the lower mantle is nearly two orders of magnitude greater than average upper-mantle viscosity.

Although, in future studies, we may be obliged to use $L \geq 512$ for modelling Earth-like convective flows (at least in the upper mantle), in this study we adopted a globally uniform spectral description characterized by a spherical harmonic truncation at degree 256 to reconcile the contrasting horizontal resolution requirements in the upper and lower mantle. To control any possible numerical instabilities in the upper mantle due to aliasing in the spectral domain we employed a Lanczos filtering of the spherical harmonic expansion of the non-linear temperature advection term. We found that the application of this spectral filtering throughout the mantle did not bias the essential global energy balance.

We obtained a valid approximation of steady-state geotherms for both surface boundary conditions (tectonic plates, rigid surface). In both cases we obtain surface heat flux values in the range of Earth-like values: 37 TW for a rigid surface and 44 TW for a surface with tectonic plates coupled to the mantle flow. Also, we find that although our convection simulations de-

liver relatively high CMB heat flux, namely 13 TW and 20 TW, for rigid and plate-like surface boundary conditions, respectively, these values are compatible with independent higher estimates (e.g., Lay et al. (2006)). We further note that the relatively high values of CMB heat flux predicted by our convection models are obtained assuming a CMB temperature of 3300 K. If we employ higher CMB temperatures, for example 4000 K (Boehler (1996)), then our predicted CMB heat flux becomes much larger than even the current highest independent estimates. Closely related to the question of CMB temperature, and the energy budget of the mantle, is the rate of secular cooling and, in particular, the radial distribution of internal heating. These outstanding questions provide motivation for a new set of simulations that will be tested in future studies employing the robust and efficient numerical convection methods presented in this work.

Although an initial thermal structure is strongly imprinted on the future mantle evolution, the extent to which a starting mantle heterogeneity determines the final temperature distribution depends on the surface boundary conditions. We have shown that a steady-state mantle-flow pattern obtained by a thermal convection simulation with a rigid surface is dependent on the starting mantle heterogeneity, and tends to harmonic degree 3, and 4. The dominant convection modes for the rigid-surface models are able to reinforce and maintain the stability of some of the present-day hotspot-related plumes in the mantle and this stability extends over remarkably long geological time spans. The plate-like surface boundary condition, in which the tectonic plate motions are coupled to those inside the mantle, is also able to produce some of the hotspots but these hotspot-related plumes are transient in character, persisting over the first few hundred million years, but then continue to change in pattern after about five hundred million years as the model evolves further to long-term steady-state. Also, a model with the plate-like surface boundary condition delivers a relatively similar final temperature distribution, tends to degree 1, regardless of the initial buoyancy field as the direct consequence of the present-day configuration of plate geometry. We should keep in mind that there is no currently accepted theory for accurately predicting the future evolution of surface plate geometries over very long geological time spans, in a manner that is dynamically self-consistent with the underlying mantle flow.

Obviously, the comparative analysis of the steady-state upwellings obtained by the rigid surface model and the transient hot thermal diapirs reinforced by the mobile surface plates

in the first few hundred million years, as well as their spatial connection to the present-day hotspots, can serve as an indicator of deep-mantle plumes resolved by seismic images and a depth-dependent rheology. Using this approach, we suggest that the tomography based (Simmons et al. (2009)) deep-mantle plumes are beneath the following present-day hotspots: Pitcairn, Easter, Galapagos, Crozet, Kerguelen, Caroline, and Cape Verde.

Although some convection studies have argued that large-amplitude chemical heterogeneity in the lower mantle (e.g.,Tan et al. (2011)) is needed to generate stable plume clusters, our results suggest that the geodynamically constrained viscosity maximum in the lower mantle (Forte & Mitrovica (2001); Mitrovica & Forte (2004)), in conjunction with the high CMB heat flux, is very effective in maintaining long-lived stable plumes. Indeed our findings ultimately lend further support to previous studies demonstrating a dominantly thermal interpretation of heterogeneity in the tomography models (e.g., Forte & Mitrovica (2001); Quéré & Forte (2006); Simmons et al. (2007); Simmons et al. (2009); Schuberth et al. (2009a,b); Davies & Davies (2009)).

The robustness of quasi-reversibility (QRV) reconstructions is constrained by the maximum degree of spherical harmonic expansion, and we prescribed L=32 as an optimal horizontal resolution for the QRV pseudo-spectral method over 65 Myr intervals. However, a higher horizontal resolution (for example, L=64) can be used for the QRV modelling of past mantle heterogeneity over shorter time-windows (~40 Myr).

Also, we have formulated the regularization parameter as a time-dependent function (β-function, eq. 3.9) that is able to solve the inverse problem of mantle convection for the steady-state solutions within 10% of uncertainty over an interval equivalent to the length of the Cenozoic era (i.e. 65 Myr).

We have discovered a high sensitivity of the QRV reconstruction robustness to the initial conditions of the system. Namely, uncertainties of reconstructed geodynamical observables are a few times higher for the models initialized by the present-day mantle heterogeneity (the CE-class) than for the simulations initialized by the steady-state solutions (the SS-class) using a two-boundary layer (2BL) geotherm for both classes. The CE-class models emphasize the 'incompatibility' of instantaneous mantle flow estimated by the 3-D tomographic image and thermal boundary layers (TBLs) introduced by a 2BL-geotherm. The 'Earth-like' geotherm rein-

forces the strong subduction zones in the first 30 Myr, and plumes that extend across the mantle to the opposite TBL after 65 Myr of mantle convection (Glišović et al. (2012)). The consequent mixing of this transported thermal heterogeneity rapidly builds amplitude of lateral variations in temperature inside the boundary layers. There is no doubt that the geotherm with TBLs plays a crucial role in thermal evolution of Earth's mantle constraining the reliability of a reconstructed temperature field at some point in the past.

Therefore, we probably ought to consider two different β_0-values in order to properly cover the Cenozoic era due to an enormous increase of mantle heterogeneity amplitude inside the TBLs (especially the upper one) between 30 Ma and 65 Ma. To achieve 71%, 63%, 67%, and 91% predictability of the horizontal divergence of the tectonic plates, free-air gravity anomalies, the dynamic surface and CMB topography, respectively, we have to apply $\beta_0 = 1 \times 10^{-13}$ from 0 to ~20 Ma, and $\beta_0 = 1 \times 10^{-12}$ on the rest of interval using the QRV method with both the surface tectonic plates (P) boundary condition and the 'Earth-like' geotherm (QRV-2BL model).

An additional implication of 'Earth-like' geotherm can be described by an artificial collapsing of oceanic spreading centres (for example, the East Pacific Rise) during the backward integration with the P-boundary condition. However, if we introduce an adiabatic (A) geotherm into the inverse mantle convection algorithm using the QRV method and the reconstructed geometry of tectonic plates over the Cenozoic era, then we are able to control artificial features around mid-oceanic ridges. Also, the QRV-A model compared to the QRV-2BL does not generate particular regions with relatively high-uncertainties in a prediction of mantle heterogeneity obtained from a reconstructed initial temperature field at 65 Ma. The lack of TBLs in an adiabatic geotherm allows the QRV model with both surface boundary conditions to fit a true solution of geodynamical observables around 90% over the Cenozoic era. The QRV-A uncertainty for the CE-class of inversions is about the same magnitude as one obtained by the QRV-2BL model with the initial conditions taken from the solutions in equilibrium (SS-class). This comparison leads to a debatable premise that the horizontally-averaged profile of the present-day tomographic image is similar to the adiabatic geotherm.

Collapsing of mid-oceanic ridges raises a consideration of the rigid (R) surface as an alternative surface boundary condition using the QRV-2BL model. The QRV-2BL simulation with the

R-boundary condition is also able to preserve emerging hot material onto the ocean floor over a considerable long time-window during the past 65 Myr of mantle evolution. With the exception that the QRV-2BL model with a rigid surface predicts relatively robust reconstruction of free-air gravity anomalies (81% accuracy), the CMB topography (94%), and the dynamic surface topography (90%). However, any rigid surface simulation is not able to provide information regarding the surface divergence.

For the CE-class of simulations we are not able to predict the heat flux over the Cenozoic era, and therefore we used a constant geotherm. However, the steady-state simulations (the SS-class) show the efficiency of the time-varying β-function to keep the level of predictability around 95% on the 65 Myr interval.

Using an 'Earth-like' geotherm for the forward solution starting from the initial conditions estimated by the BAD method (the BAD-2BL model) indicates that the BAD method failed to deliver a robust initial inverse solution. In other words, the BAD-2BL simulation is not able to preserve the maximum uncertainty estimated by the QRV method over a period of more than 20 Myr. Therefore the QRV method is superior in relation to the BAD method that is only able to provide accurate reconstruction using an adiabatic geotherm (the BAD-A model) in both directions of integration over the Cenozoic era. The robustness of QRV-A simulation is about two order of magnitude greater than that of the BAD-A model.

Summarizing all QRV results we define a range of robustness for the free-air gravity anomalies, the CMB tomography, the dynamic surface topography, and the horizontal divergence of the tectonic plates that are [63,89]%, [91,94]%, [67,92]%, and [71,93]%, respectively.

Our current numerical convection model has implemented a number of computational innovations that allow us to carry out accurate and stable simulations over very long geological time scales, in excess of a billion years. Although these simulations have implemented a number of important Earth-like parameter values (such as depth-dependent viscosity) there remain a number of outstanding challenges that we wish to resolve in a future series of forward convection runs. We are, in particular, interested in adding the following important geodynamical properties of the Earth's mantle:

1. the coupled core-mantle evolution (e.g., Buffet et al. (1996); Nakagawa & Tackley (2008a)),

2. radial and lateral heterogeneity in the distribution of radiogenic internal heating,

3. 3-D spatial and temporal variability of the effective viscosity of the mantle as well as temporal variations in thermal conductivity (k) based on Hofmeister (1999) interpretation of k, and

4. temporal and spatial variations in the geometry of surface tectonic plates determined in a dynamically self-consistent manner.

Another of our priorities is time-reversed convection modelling, and we are especially interested in the application of an heuristic, but efficient algorithm that is termed 'back and forward nudging' (Auroux et al. (2011)).

BIBLIOGRAPHY

Ammann, M. W., Brodholt, J. P., Wookey, J., & Dobson, D. P., 2010. First-principles constraints on diffusion in lower-mantle minerals and a weak D"-layer, *Nature*, **465**, 462-465.

Ascher, U. M., Ruuth, S. J., & Wetton, T. R., 1995. Implicit-explicit methods for time-dependent partial differential equations, *SIAM J. Numer Anal.*, **32**(3), 797-823.

Auroux, D., Blum, J., & Nodet, M., 2011. Diffusive Back and Forth Nudging algorithm for data assimilation, *Comptes Rendus Mathematique*, **349**(15-16), 849-854.

Baumgardner, J. R., 1985. Three dimensional treatment of convective flow in the Earth's mantle, *J. Stat. Phys.*, **39**, 501-511.

Behn, M. D., Conrad, C. P., & Silver, P. G., 2004. Detection of upper mantle flow associated with the African Superplume, *Earth and Planetary Science Letters*, **224**(3-4), 259-274.

Boehler, R., 1996. Melting temperature of the Earth's mantle and core: Earth's thermal structure, *Annual Review of Earth and Planetary Sciences*, **24**(1), 15-40.

Boehler, R. & Chopelas, A., 1991. A new approach to laser heating in high pressure mineral physics, *Geophys. Res. Lett.*, **18**(6), 1147-1150.

Bradley, D. C., 2011. Secular trends in the geologic record and the supercontinent cycle, *Earth-Science Reviews*, **108**(1-2), 16-33.

Buffet, B. A., Huppert, H. E., Lister, J. R., & Woods, A. W., 1996. On the thermal evolution of the Earth's core, *Journal of Geophysical Research*, **101**, 7989-8006.

Bunge, H., Hagelberg, C., & Travis, B., 2003. Mantle circulation models with variational data assimilation: inferring past mantle flow and structure from plate motion histories and seismic tomography, *Geophys. J. Int.*, **152**, 280-301.

Bunge, H.-P., 2005. Low plume excess temperature and high core heat flux inferred from non-adiabatic geotherms in internally heated mantle circulation models, *Physics of The Earth and Planetary Interiors*, **153**(1-3), 3-10, Studies of the Earth's Deep Interior - SEDI 2004.

Bunge, H. P. & Richards, M. A., 1996. The origin of large scale structure in mantle convection: effects of plate motions and viscosity stratification, *Geophys. Res. Lett.*, **23**, 2987-2990.

Bunge, H.-P., Richards, M. A., Lithgow-Bertelloni, C., Baumgardner, J. R., Grand, S. P., & Romanowicz, B. A., 1998. Time Scales and Heterogeneous Structure in Geodynamic Earth Models, *Science*, **280**(5360), 91-95.

Bunge, H.-P., Richards, M. A., & Baumgardner, J. R., 2002. Mantle-circulation models with sequential data assimilation: inferring present-day mantle structure from plate-motion histories, *Phil. Trans. R. Soc. Lond.*, **360**(1800), 2545-2567.

Cadio, C., Panet, I., Davaille, A., Diament, M., Métivier, L., & de Viron, O., 2011. Pacific geoid anomalies revisited in light of thermochemical oscillating domes in the lower mantle, *Earth and Planetary Science Letters*, **306**(1-2), 123-135.

Cande, S. & Stegman, D., 2011. Indian and African plate motions driven by the push force of the Reunion plume head, *Nature*, **475**, 47-52.

Chandrasekhar, S., 1961. *Hydrodynamic and hydromagnetic stability*, Oxford University Press, London and New York.

Chopelas, A. & Boehler, R., 1992. Thermal expansivity in the lower mantle, *Geophys. Res. Lett.*, **19**, 1983-1986.

Conrad, C. P. & Gurnis, M., 2003. Seismic tomography, surface uplift, and the breakup of Gondwanaland: Integrating mantle convection backwards in time, *Geochem. Geophys. Geosyst.*, **4**(3), 1031, doi:10.1029/2001GC000299.

Cordier, P., Amodeo, J., & Carrez, P., 2012. Modelling the rheology of MgO under Earth's mantle pressure, temperature and strain rates, *Nature*, **481**, 177-180.

Corrieu, V., Ricard, Y., , & Froidevaux, C., 1994. Converting mantle tomography into mass anomalies to predict the Earth's radial viscosity, *Phys. Earth Planet. Inter.*, **84**, 3-13.

Courtillot, V. & Besse, J., 1987. Magnetic field reversals, polar wander, and core-mantle coupling, *Science*, **237**, 1140-1147.

Courtillot, V. & Olson, P., 2007. Mantle plumes link magnetic superchrons to phanerozoic mass depletion events, *Earth and Planetary Science Letters*, **260**(3-4), 495-504.

Courtillot, V., Davaille, A., Besse, J., & Stock, J., 2003. Three distinct types of hotspots in the Earth's mantle, *Earth and Planetary Science Letters*, **205**(3-4), 295-308.

Davaille, A., Girard, F., & Bars, M. L., 2002. How to anchor hotspots in a convecting mantle?, *Earth and Planetary Science Letters*, **203**(2), 621-634.

Davies, D. R. & Davies, J. H., 2009. Thermally-driven mantle plumes reconcile multiple hotspot observations, *Earth and Planetary Science Letters*, **278**(1-2), 50-54.

Davies, J. H., 2005. Steady plumes produced by downwellings in Earth-like vigor spherical whole mantle convection models, *Geochem. Geophys. Geosyst.*, **6**, Q12001, doi:10.1029/2005GC001042.

Duncan, R. A. & Richards, M. A., 1991. Hotspots, mantle plumes, flood basalts, and true polar wander, *Rev. Geophys.*, **29**(1), 31-50.

Dziewonski, A. M. & Anderson, D. L., 1981. Preliminary reference Earth model, *Phys. Earth Planet. Inter.*, **25**, 297-356.

Forte, A., Moucha, R., Rowley, D., Quéré, S., Mitrovica, J., Simmons, N., & Grand, S., 2009. Recent tectonic plate decelerations driven by mantle convection, *Geophys. Res. Lett.*, **36**, L23301.

Forte, A. M., 2000. Seismic-geodynamic constraints on mantle flow: Implications for layered convection, mantle viscosity, and seismic anisotropy in the deep mantle, in *Earth's Deep Interior*, pp. 3-36, eds Karato, S., Forte, A. M., Liebermann, R. C., Masters, G., & Stixrude, L., American Geophysical Union, Washington, D.C.

Forte, A. M., 2007. Constraints on seismic models from other disciplines: Implications for mantle dynamics and composition, in *Treatise of Geophysics Vol.1*, pp. 805-854, eds Romanowicz, B. & Dziewonski, A. M., Elsevier, Amsterdam.

Forte, A. M. & Mitrovica, J. X., 1997. A resonance in the Earth's obliquity and precession over the past 20 Myr driven by mantle convection, *Nature*, **390**, 676--680.

Forte, A. M. & Mitrovica, J. X., 2001. Deep-mantle high-viscosity flow and thermochemical structure inferred from seismic and geodynamic data, *Nature*, **410**, 1049-1055.

Forte, A. M. & Peltier, W. R., 1987. Plate tectonics and aspherical Earth structure: The importance of poloidal-toroidal coupling, *J. Geophys. Res.*, **92**, 3645-3679.

Forte, A. M. & Peltier, W. R., 1991. Viscous flow models of geophysical observables, 1. Forward problems, *J. Geophys. Res.*, **96**(20), 131-159.

Forte, A. M. & Peltier, W. R., 1994. The kinematics and dynamics of poloidal-toroidal coupling in mantle flow: The importance of surface plates and lateral viscosity variations, *Adv. Geophys.*, **36**, 1-119.

Forte, A. M., Peltier, W. R., & Dziewonski, A. M., 1991. Inferences of mantle viscosity from tectonic plate velocities, *Geophys. Res. Lett.*, **18**, 1747-1750.

Forte, A. M., Dziewonski, A. M., & Woodward, R. L., 1993. Aspherical structure of the mantle, tectonic plate motions, nonhydrostatic geoid, and topography of the core-mantle boundary, in *Dynamics of the Earth's Deep Interior and Earth Rotation*, 72, pp. 135-166, eds Le Mouël, J.-L., Smylie, D., & Herring, T., American Geophysical Union, Washington, D.C.

Forte, A. M., Quéré, S., Moucha, R., Simmons, N. A., Grand, S. P., Mitrovica, J. X., & Rowley, D. B., 2010. Joint seismic-geodynamic-mineral physical modelling of African geodynamics: A reconciliation of deep-mantle convection with surface geophysical constraints, *Earth and Planetary Science Letters*, **295**(3-4), 329-341.

Gaboret, C., Forte, A. M., & Montagner, J.-P., 2003. The unique dynamics of the Pacific Hemisphere mantle and its signature on seismic anisotropy, *Earth and Planetary Science Letters*, **208**(3-4), 219-233.

Glatzmaier, G. A., 1984. Numerical simulations of stellar convective dynamos, I. The model and method, *J. Computational Physics*, **55**, 461-484.

Glatzmaier, G. A., 1988. Numerical simulations of mantle convection: time-dependent, three-dimensional, compressible, spherical shell, *Geophys. Astrophys. Fluid Dynamics*, **43**, 223-264.

Glišović, P., Forte, A. M., & Moucha, R., 2012. Time-dependent convection models of mantle thermal structure constrained by seismic tomography and geodynamics: implications for mantle plume dynamics and CMB heat flux, *Geophys. J. Int*, **190**, 785-815.

Hager, B. H. & Clayton, R. W., 1989. Constraints on the structure of mantle convection using seismic observations, flow models, and the geoid, in *Mantle Convection*, pp. 657-763, ed. Peltier, W., Gordon and Breach, New York.

Hager, B. H. & O'Connell, R. J., 1978. Subduction zone dip angles and flow driven by plate motion, *Tectonophysics*, **50**(2-3), 111-133.

Hager, B. H. & O'Connell, R. J., 1981. A simple global model of plate dynamics and mantle convection, *J. Geophys. Res.*, **86**, 4843-4867.

Herring, J. R., Orszag, S. A., Kraichnan, R. H., & Fox, D. G., 1974. Decay of two-dimensional homogeneous turbulence, *J. Fluid. Mech.*, **66**, 417-444.

Hofmeister, A. M., 1999. Mantle Values of Thermal Conductivity and the Geotherm from Phonon Lifetimes, *Science*, **283**, 1699-1706.

Huang, H., Fei, Y., Cai, L., Jing, F., Hu, X., Xie, H., Zhang, L., & Gong, Z., 2011. Evidence for an oxygen-depleted liquid outer core of the Earth, *Nature*, **479**, 513-517.

Ismail-Zadeh, A., Schubert, G., Tsepelev, I., & Korotkii, A., 2004. Inverse problem of thermal convection: numerical approach and application to mantle plume restoration, *Physics of the Earth and Planetary Interiors*, **145**(1-4), 99-114.

Ismail-Zadeh, A., Korotkii, A., Schubert, G., & Tsepelev, I., 2007. Quasi-reversibility method for data assimilation in models of mantle dynamics, *Geophys. J. Int.*, **170**, 1381-1398.

Jackson, I., 1998. Elasticity, composition and temperature of the Earth's lower mantle: A reappraisal, *Geophys. J. Int.*, **134**, 291-311.

Jarvis, G. T., 1991. Two-dimensional numerical models of mantle convection, *Adv. Geophys.*, **33**, 1-80.

Jarvis, G. T. & McKenzie, D. P., 1980. Convection in a compressible fluid with infinite Prandtl number, *J. Fluid Mech.*, **96**, 515-583.

Jaupart, C., Labrosse, S., & Mareschal, J.-C., 2007. Temperatures, Heat and Energy in the Mantle of the Earth, in *Treatise on Geophysics Vol. 7*, pp. 253-304, ed. Schuberth, G., Elsevier Ltd., Oxford.

Jurdy, D., 1981. True polar wander, *Tectonophysics*, **74**(1-2), 1-16, Quantitative methods of assessing plate motions.

Kellogg, L. H. & King, S. D., 1997. The effect of temperature dependent viscosity on the structure of new plumes in the mantle: Results of a finite element model in a spherical, axisymmetric shell, *Earth Planet. Sci. Lett.*, **148**, 13-26.

King, S. D., 1995a. Radial models of mantle viscosity: Results from a genetic algorithm, *Geophys. J. Int.*, **122**, 725-734.

King, S. D., 1995b. Models of mantle viscosity, in *Mineral Physics and Crystallography: A Handbook of Physical Constants*, pp. 227-236, ed. Ahrens, T., American Geophysical Union, Washington, D.C.

King, S. D. & Masters, G., 1992. An inversion for radial viscosity structure using seismic tomography, *Geophys. Res. Lett.*, **19**, 1551-1554.

King, S. D., Raefksy, A., & Hager, B. H., 1990. Vectorizing a finite element code for incompressible two-dimensional convection in the Earth's mantle, *Phys. Earth Planet. Inter.*, **59**, 195-207.

Korenaga, J., 2007. Eustasy, supercontinental insulation, and the temporal variability of terrestrial heat flux, *Earth and Planetary Science Letters*, **257**(1-2), 350-358.

Labrosse, S. & Jaupart, C., 2007. Thermal evolution of the Earth: Secular changes and fluctuations of plate characteristics, *Earth and Planetary Science Letters*, **260**(3-4), 465-481.

Labrosse, S., Hernlund, J. W., & Coltice, N., 2008. The Heat Flow out of the Core and its Temporal Fluctuations, *AGU Fall Meeting Abstracts*, p. A1736.

Landau, L. D. & Lifshitz, E. M., 1959. *Fluid Mechanics*, vol. 6, Pergamon, New York.

Larsen, T. B., Yuen, D. A., Moser, J., & Fornberg, B., 1997. A high-order finite-difference method applied to large Rayleigh number mantle convection, *Geophys. Astrophys. Fluid Dyn.*, **84**, 53-83.

Laskar, J., 1990. The chaotic motion of the solar system: A numerical estimate of the size of the chaotic zones, *Icarus*, **88**(2), 266-291.

Lattes, R. & Lions, J.-L., 1969. *The method of quasi-reversibility applications to partial differential equations*, American Elsevier Publishing Company, INC., New York.

Lay, T., Hernlund, J., Garnero, E. J., & Thorne, M. S., 2006. A Post-Perovskite Lens and D" Heat Flux Beneath the Central Pacific, *Science*, **314**(5803), 1272-1276.

Lithgow-Bertelloni, C. & Richards, M., 1998. The dynamics of Cenozoic and Mesozoic plate motions, *Rev. Geophys.*, **36**, 27-78.

Lowman, J. P., King, S. D., & Gable, C. W., 2004. Steady plumes in viscously stratified, vigorously convecting, three-dimensional numerical mantle convection models with mobile plates, *Geochem. Geophys. Geosyst.*, **5**(1), Q01L01, doi:10.1029/2003GC000583.

Lowman, J. P., Gait, A. D., Gable, C. W., & Kukreja, H., 2008. Plumes anchored by a high viscosity lower mantle in a 3D mantle convection model featuring dynamically evolving plates, *Geophys. Res. Lett.*, **35**, L19309, doi:10.1029/2008GL035342.

Machetel, P. & Yuen, D. A., 1986. The onset of time-dependent convection in spherical shells as a clue to chaotic convection in the Earth's mantle, *Geophys. Res. Lett.*, **13**, 1470-1473.

Mareschal, J.-C., Jaupart, C., Phaneuf, C., & Perry, C., 2012. Geoneutrinos and the energy budget of the Earth, *Journal of Geodynamics*, **54**(0), 43-54.

McKenzie, D. P., Roberts, J. M., & Weiss, N. O., 1974. Convection in the Earth's mantle: Towards a numerical simulation, *J. Fluid Mech.*, **62**, 465-538.

McNamara, A. K. & Zhong, S., 2005. Thermochemical structures beneath Africa and the Pacific Ocean, *Nature*, **437**, 1136-1139.

Mitrovica, J. X. & Forte, A. M., 1997. The radial profile of mantle viscosity: Results from the joint inversion of convection and post-glacial rebound observables, *J. Geophys. Res.*, **102**, 2751-2769.

Mitrovica, J. X. & Forte, A. M., 2004. A new inference of mantle viscosity based upon joint inversion of convection and glacial isostatic adjustment data, *Earth and Planetary Science Letters*, **225**(1-2), 177-189.

Morgan, W. J., 1971. Convection plumes in the lower mantle, *Nature*, **230**, 42-43.

Moucha, R. & Forte, A. M., 2011. Changes in African topography driven by mantle convection, *Nature Geoscience*, **4**, 707-712.

Moucha, R., Forte, A. M., Mitrovica, J. X., & Daradich, A., 2007. Lateral variations in mantle rheology: implications for convection related surface observables and inferred viscosity models, *Geophysical Journal International*, **169**(1), 113-135.

Moucha, R., Forte, A. M., Mitrovica, J. X., Rowley, D. B., Quéré, S., Simmons, N. A., & Grand, S. P., 2008. Dynamic topography and long-term sea-level variations: There is no such thing as a stable continental platform, *Earth and Planetary Science Letters*, **271**(1-4), 101-108.

Müller, R. D., Sdrolias, M., Gaina, C., Steinberger, B., & Heine, C., 2008. Long-Term Sea-Level Fluctuations Driven by Ocean Basin Dynamics, *Science*, **319**, 1357-1362.

Nakagawa, T. & Tackley, P. J., 2008a. Effects of a perovskite-post perovskite phase change near core-mantle boundary in compressible mantle convection, *Geophys. Res. Lett.*, **31**, L16611.

Nakagawa, T. & Tackley, P. J., 2008b. Lateral variations in CMB heat flux and deep mantle seismic velocity caused by a thermal-chemical-phase boundary layer in 3D spherical convection, *Earth and Planetary Science Letters*, **271**(1-4), 348-358.

Orszag, S. A., 1971. Numerical simulation of incompressible flows within simple boundaries: Accuracy, *J. Fluid Mech.*, **49**, 75-112.

Orszag, S. A., 1974. Fourier series on spheres, *Mon. Weath. Rev*, **102**, 56-75.

Panasyuk, S. V. & Hager, B. H., 2000. Inversion for mantle viscosity profiles constrained by dynamic topography and the geoid, and their estimated errors, *Geophys. J. Int.*, **143**, 821-836.

Panasyuk, S. V., Hager, B. H., & Forte, A. M., 1996. Understanding the effects of mantle compressibility on geoid kernels, *Geophys. J. Int.*, **124**, 121-133.

Parsons, B. & Daly, S., 1983. The relationship between surface topography, gravity anomalies, and temperature structure of convection, *J. Geophys. Res.*, **88**, 1129-1144.

Peltier, W. R., 1972. Penetrative convection in the planetary mantle, *Geophys. Astrophys. Fluid Dyn.*, **5**, 47-88.

Phinney, R. A. & Burridge, R., 1973. Representation of the elastic-gravitational excitation of a spherical Earth model by generalized spherical harmonics, *Geophys. J. R. Astr. Soc.*, **34**, 451-487.

Quéré, S. & Forte, A. M., 2006. Influence of past and present-day plate motions on spherical models of mantle convection: implications for mantle plumes and hotspots, *Geophysical Journal International*, **165**(3), 1041-1057.

Ricard, Y. & Vigny, C., 1989. Mantle dynamics with induced plate tectonics, *J. Geophys. Res.*, **94**, 17543-17559.

Ricard, Y. & Wuming, B., 1991. Inferring viscosity and the 3-D density structure of the mantle from geoid, topography and plate velocities, *Geophys. J. Int.*, **105**, 561-572.

Ricard, Y., Fleitout, L., & Froidevaux, C., 1984. Geoid heights and lithospheric stresses for a dynamic Earth, *Ann. Geophys.*, **2**, 267-286.

Ricard, Y., Sabadini, R., & Spada, G., 1992. Isostatic deformations and polar wander induced by redistribution of mass within the earth, *J. Geophys. Res.*, **97**(B10), 14223-14236.

Ricard, Y., Richards, M., Lithgow-Bertelloni, C., & Le Stunff, Y., 1993. A geodynamic model of mantle density heterogeneity, *J. Geophys. Res.*, **98**(21), 895-909.

Richards, M. & Engebretson, D., 1992. Large-scale mantle convection and the history of subduction, *Nature*, **355**, 437-440.

Richards, M., Ricard, Y., Lithgow-Bertelloni, C., Spada, G., & R., S., 1997. An explanation for Earth's long-term rotational stability, *Science*, **275**, 372-375.

Richards, M. A. & Hager, B. H., 1984. Geoid anomalies in a dynamic Earth, *J. Geophys. Res.*, **89**, 5987-6002.

Roberts, J. H. & Zhong, S., 2006. Degree-1 convection in the Martian mantle and the origin of the hemispheric dichotomy, *J. Geophys. Res.*, **111**, E06013, doi:10.1029/2005JE002668.

Samarskii, A., Vabishchevich, P., & Vasiliev, V., 2004. Numerical Methods for Solving Inverse Problems of Mathematical Physics, *URSS*, p. 478, (in Russian).

Schubert, G., Berkovici, D., & Glatzmaier, G. A., 1990. Mantle dynamics in Mars and Venus: Influence of an immobile lithosphere on three-dimensional mantle convection, *J. Geophys. Res*, **95**, 14105-29.

Schubert, G., Solomatov, V. S., Tackley, P. J., & Turcotte, D. L., 1997. Mantle convection and the thermal evolution of Venus, in *Venus II - Geology, Geophysics, Atmosphere, and Solar Wind Environment*, pp. 1245-1288, eds Bougher, S. W., Hunten, D. M., & Phillips, R. J., Universoty of Arizona Press, Tuscon, Arizona.

Schubert, G., Turcotte, D. L., & Olson, P., 2001. *Mantle Convection in the Earth and Planets*, Cambridge University Press, Cambridge.

Schuberth, B. S. A., Bunge, H.-P., & Ritsema, J., 2009a. Tomographic filtering of high-resolution mantle circulation models: Can seismic heterogeneity be explained by temperature alone?, *Geochem. Geophys. Geosyst.*, **10**, Q05W03, doi:10.1029/2009GC002401.

Schuberth, B. S. A., Bunge, H.-P., Steinle-Neumann, G., Moder, C., & Oeser, J., 2009b. Thermal versus elastic heterogeneity in high-resolution mantle circulation models with pyrolite composition: High plume excess temperatures in the lowermonst mantle, *Geochem. Geophys. Geosyst.*, **10**, Q01W01, doi:10.1029/2008GC002235.

Scotese, C. R., 2001. *Atlas of Earth History*, vol. 1, Paleogeography, PALEOMAP Project, Arlington, Texas, 52 pp.

Simmons, N. A., Forte, A. M., & Grand, S. P., 2007. Thermochemical structure and dynamics of the African superplume, *Geophys. Res. Lett.*, **34**, L02301, doi:10.1029/2006GL028009.

Simmons, N. A., Forte, A. M., & Grand, S. P., 2009. Joint seismic, geodynamic and mineral physical constraints on three-dimensional mantle heterogeneity: Implications for the relative importance of thermal versus compositional heterogeneity, *Geophysical Journal International*, **177**(3), 1284-1304.

Smirnov, A. V. & Tarduno, J. A., 2010. Co-location of eruption sites of the Siberian Traps and North Atlantic Igneous Province: Implications for the nature of hotspots and mantle plumes, *Earth and Planetary Science Letters*, **297**(3-4), 687-690.

Solheim, L. P., 1986. *Axially symmetric convection in spherical shells*, Master's thesis, University of Toronto, Toronto, Canada, M.Sc. thesis.

Solheim, L. P. & Peltier, W. R., 1990. Heat transfer and the onset of chaos in a spherical, axisymmetric, anelastic model of whole mantle convection, *Geophys. Astrophys. Fluid Dyn.*, **53**(4), 205-255.

Solomatov, S. & Reese, C., 2006. Formation of lower mantle heterogeneity due to grain size-dependent viscosity, *AGU, Fall Meeting Abstracts*, pp. MR21A-0010.

Spasojevic, S., Liu, L., & Gurnis, M., 2009. Adjoint models of mantle convection with seismic, plate motion, and stratigraphic constraints: North America since the Late Cretaceous, *Geochem. Geophys. Geosyst.*, **10**, Q05W02, doi:10.1029/2008GC002345.

Stacey, F. D., 1998. Thermoelasticity of a mineral composite and a reconsideration of lower mantle properties, *Phys. Earth Planet. Int.*, **106**, 219-236.

Steinberger, B. & Calderwood, A. R., 2006. Models of large-scale viscous flow in the Earth's mantle with constraints from mineral physics and surface observations, *Geophysical Journal International*, **167**(3), 1461-1481.

Steinberger, B. & O'Connell, J., 1998. Advection of plumes in mantle flow: implications for hotspot motion, mantle viscosity and plume distribution, *Geophysical Journal International*, **132**, 412-434.

Steinberger, B. & O'Connell, R. J., 1997. Changes of the Earth's rotation axis owing to advection of mantle density heterogeneities, *Nature*, **387**, 169-173.

Styles, E., Goes, S., van Keken, P. E., Ritsema, J., & Smith, H., 2011. Synthetic images of dynamically predicted plumes and comparison with a global tomographic model, *Earth and Planetary Science Letters*, **311**(3-4), 351-363.

Tackley, P. J., 1997. Effects of phase transitions on three-dimensional mantle convection, in *The Fluid Mechanics of Astrophysics and Geophysics Volume 5: The Doornbos Volume*, pp. 273-336, ed. Crossley, D., Gordon and Breach, New York.

Tackley, P. J., 2000. Mantle Convection and Plate Tectonics: Toward an Integrated Physical and Chemical Theory, *Science*, **288**(5473), 2002-2007.

Tan, E., Leng, W., Zhong, S., & Gurnis, M., 2011. On the location of plumes and lateral movement of thermochemical structures with high bulk modulus in the 3-D compressible mantle, *Geochem. Geophys. Geosyst.*, **12**, Q07005, doi:10.1029/2011GC003665.

Terasaki, H., Kamada, S., Sakai, T., Ohtani, E., Hirao, N., & Ohishi, Y., 2011. Liquidus and solidus temperatures of a Fe–O–S alloy up to the pressures of the outer core: Implication for the thermal structure of the Earth's core, *Earth and Planetary Science Letters*, **304**(3-4), 559-564.

Tosi, N., Čadek, O., & Martinec, Z., 2009. Subducted slabs and lateral viscosity variations: effects on the long-wavelength geoid, *Geophysical Journal International*, **179**(2), 813-826.

van Keken, P. E. & Ballentine, C. J., 1999. Dynamical models of mantle volatile evolution and the role of phase transitions and temperature-dependent rheology, *J. Geophys. Res.*, **104**, 7137-7168.

van Keken, P. E., Yuen, D. A., & van den Berg, A. P., 1994. Implications for mantle dynamics from the high melting temperature of perovskite, *Science*, **264**, 1437-1439.

Čadek, O. & Fleitout, L., 2003. Effect of lateral viscosity variations in the top 300 km on the geoid and dynamic topography, *Geophysical Journal International*, **152**(3), 566-580.

Čadek, O. & Fleitout, L., 2006. Effect of lateral viscosity variations in the core-mantle boundary region on predictions of the long-wavelength geoid, *Studia Geophysica et Geodaetica*, **50**, 217-232, 10.1007/s11200-006-0013-0.

Voice, P. T., Kowalewski, M., & Eriksson, K. A., 2011. Quantifying the timing and rate of crustal evolution: Global compilation of radiometrically dated detrital zircon grains, *J. Geol.*, **119**(2), 109-126.

Yoshida, M., 2008. Mantle convection with longest-wavelength thermal heterogeneity in a 3-D spherical model: Degree one or two?, *Geophys. Res. Lett.*, **35**, L23302, doi:10.1029/2008GL036059.

Yoshida, M., 2010. Preliminary three-dimensional model of mantle convection with deformable, mobile continental lithosphere, *Earth and Planetary Science Letters*, **295**(1-2), 205-218.

Yoshida, M. & Kageyama, A., 2006. Low-degree mantle convection with strongly temperature- and depth-dependent viscosity in a three-dimensional spherical shell, *J. Geophys. Res.*, **111**, B03412, doi:10.1029/2005JB003905.

Yoshida, M. & Santosh, M., 2011. Supercontinents, mantle dynamics and plate tectonics: A perspective based on conceptual vs. numerical models, *Earth-Science Reviews*, **105**(1-2), 1-24.

Zhang, N., Zhong, S., Leng, W., & Li, Z.-X., 2010. A model for the evolution of the Earth's mantle structure since the Early Paleozoic, *J. Geophys. Res.*, **115**, B06401, doi:10.1029/2009JB006896.

Zhang, S. & Christensen, U., 1993. Some effects of lateral viscosity variations on geoid and surface velocities induced by density anomalies in the mantle, *Geophysical Journal International*, **114**(3), 531-547.

Zhang, S. & Yuen, D. A., 1996. Various influences on plumes and dynamics in time-dependent, compressible mantle convection in 3-D spherical shell, *Phys. Earth Planet. Int.*, **94**, 241-267.

Zhao, D., 2004. Global tomographic images of mantle plumes and subducting slabs: insight into deep Earth dynamics, *Physics of the Earth and Planetary Interiors*, **146**(1-2), 3-34.

Zhao, D., 2007. Seismic images under 60 hotspots: Search for mantle plumes, *Gondwana Research*, **12**(4), 335-355.

Zhong, S., Zuber, M. T., Moresi, L., & Gurnis, M., 2000. Role of temperature-dependent viscosity and surface plates in spherical shell models of mantle convection, *J. Geophys. Res.*, **105**(B5), 11063-11082.

Zhong, S., Zhang, N., Li, Z.-X., & Roberts, J. H., 2007. Supercontinent cycles, true polar wander, and very long-wavelength mantle convection, *Earth and Planetary Science Letters*, **261**(3-4), 551-564.